Experiments and Numerical Analysis on Air Bearing Slumping of Segmented Thin-shell Mirrors for X-ray Telescopes

by

Heng Zuo

B.S., Tsinghua University (2014)

Submitted to the Department of Aeronautics and Astronautics
in partial fulfillment of the requirements for the degree of

Master of Science in Aeronautics and Astronautics

at the

MASSACHUSETTS INSTITUTE OF TECHNOLOGY

May 2017 [June 2017]

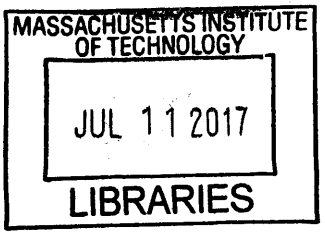

ARCHIVES

Author ..... Signature redacted .....
Department of Aeronautics and Astronautics
May 8, 2017

Certified by .. Signature redacted .....
Mark L. Schattenburg
Senior Research Scientist
Thesis Supervisor

Accepted by .... Signature redacted .....
Youssef M. Marzouk
Associate Professor of Aeronautics and Astronautics
Chairman, Graduate Program Committee

Experiments and Numerical Analysis on Air Bearing Slumping of Segmented Thin-shell Mirrors for X-ray Telescopes

by

Heng Zuo

Submitted to the Department of Aeronautics and Astronautics
on May 8, 2017, in partial fulfillment of the
requirements for the degree of
Master of Science in Aeronautics and Astronautics

Abstract

Slumping (or thermal shaping) of thin glass sheets onto high precision mandrels was used by NASA Goddard Space Flight Center to fabricate the NuSTAR telescope with success. But this process requires long thermal cycles and produces mid-range spatial frequency errors due to the anti-stick mandrel coatings. Over the last few years, MIT Space Nanotechnology Lab has developed a non-contact slumping process differentiating from the preceding contact slumping, which utilizes a pair of porous air bearing mandrels through which compressed nitrogen is forced, with a thin piece of glass sheet floating between two thin layers of nitrogen during the thermal cycle. However, the underlying mechanism behind air bearing slumping still remains unveiled.

This thesis describes a series of design and tests on horizontal slumping tool with improved active control algorithm and fiber sensing techniques, which results in glass with reduced mid-range spatial frequency errors that could be accomplished in much shorter thermal cycles. We examined the influence of the slumping time, the supply pressure and the air film thickness and gravity to the outcome shape of the glass. To complement the experiments and to understand the mechanism, we built a finite element model with fluid-structure interaction to analyze the viscoelastic behavior of glass during air bearing slumping. We proved that for the 2D axisymmetric model, experimental and numerical approaches have comparable results. We also discovered the crucial impacts of bearing permeability to the glass shape. The 3D cylindrical model is also in development, and a novel vertical slumping tool is to eliminate the undesirable influence of gravity under test. Through both experiments and simulations, we believe that non-contact slumping using air bearing could remove mid-range spatial frequency errors, which is critical to producing high-resolution large-aperture thin mirrors for X-ray telescopes.

Thesis Supervisor: Mark L. Schattenburg
Title: Senior Research Scientist

Acknowledgments

Foremost, I would like to express my profound gratitude to my research adviser Dr. Mark Schattenburg for the continuous support and extensive instructions of my study and research. His guidance and immense knowledge inspired me to find my path, and his patience and enthusiasm helped me grow.

I am also deeply indebted to my two academic advisers: Prof. Raul Radovitzky and Prof. Paulo Lozano, for their enormous encouragements, insights, and perceptive comments. Many other professors at MIT Department of Aeronautics and Astronautics have also provided me with generous help, which I greatly appreciate as well.

I would also like to thank everyone in our lab. Ralf Heilmann was always there to give me valuable advice and support. Our brilliant mirror team: Brandon Chalifoux, Youwei Yao and Micheal DeTienne never hesitates to help me with their passionate involvements and meaningful discussions. My other colleagues Alex Bruccoleri, Jay Fucetola, Jungki Song and Martin Klingensmith all kindly offered me constructive suggestions.

I feel very lucky to join the amazing community of MIT, and I have met lots of wonderful persons during my past three years. I still owe much to the many people who helped me come here, especially the professors and friends in my undergraduate Tsinghua University. In view of limited space, I couldn't thank each of them explicitly in this thesis. But I feel so honored to be surrounded by all of you. Thank you.

My final gratitude go to my parents and other family members for their unfailing support and unwavering belief in me. I couldn't have achieved what I have now without you, and I'll continue to work towards becoming a better PhD candidate as well as an honorable person.

Contents

List of Figures

List of Tables

Chapter 1

Introduction

1.1 Motivation and goals

The main motivation for X-ray observatory development is to probe answers to a number of key questions in astronomy, such as to "discover how the universe works, explore how it began and evolved, and search for life on planets around other stars" as NASA's strategic objective 2014 says [17]. By projecting humankind's vantage point into space with observatories in Earth orbit and deep space, we seek to understand these profound topics about the universe with more details described in both the Decadal Survey of Astronomy and Astrophysics by National Research Council [3] and the NASA Astrophysics Roadmap [14].

Future X-ray astronomy observations call for X-ray telescopes with both fine angular resolution and large aperture areas. Different missions have various requirements depending on the energy band of the X-ray sources of interest, yet all of them will benefit from the development of lightweight high resolution thin-shell mirrors. Typically, the ideal angular resolution requires $0.5-5\,arcsecond$ HPD[1] in the sub $1\,keV$ band with collecting area $10-100$ times larger than current telescopes. Due to the special design of nested grazing-incidence optics, the mass constraints of the telescope and economic considerations, these goals are hard to achieve and the overall production of high-quality mirrors remains a challenging field. [18] In the first place, this requires

[1]HPD (half power diameter) is the diameter within which half of the focused X-rays are enclosed.

thin lightweight mirrors with very good surface figure accuracy, which are difficult to fabricate in the traditional commercialized method.

NASA Goddard Space Flight Center (GSFC) developed a method called "slumping" where thin glass sheets are placed onto high precision mandrels to form into desired conic figures by thermal shaping. This method has successfully fabricated mirrors for the famous NASA NuSTAR telescope. However, the best mirrors generated by this process are limited to resolution of about $7\,arcsecond$, primarily in the form of mid-range scale spatial frequency errors. The cause of these mid-range errors are believed to be dusts or particles in the anti-stick coatings used to prevent adhesion of mandrels and mirrors. Another downside of this approach is its long running time for each piece of mirror because long thermal cycles are necessary to the success of the shaping process.

Over the last few years, MIT Space Nanotechnology Lab (SNL) has developed a new slumping process which utilizes a pair of porous air bearing mandrels through which compressed nitrogen is forced, with the round flat glass sheet floating on a thin layer ($< 50\,\mu m$) of nitrogen during the thermal cycle. This results in glass with reduced mid-range spatial frequency errors and can be accomplished in much shorter thermal cycles. [2] Furthermore, SNL is currently developing a fine figure correction scheme "ion implantation" for thin optics, with high energy ions implanted into a substrate to cause structural changes creating near-surface stress and substrate bending. The hope is through the combination of these two methods, we will be able to fabricate mirrors of half arc seconds resolution.

The purpose of this thesis is to continue the development of air bearing slumping to study the possibility of it generating thin-shell mirrors with final resolution. A detailed mathematical model of the slumping process will be developed to understand the underlying mechanism and to predict the final glass shape based on process parameters. Experiments will also be conducted to create samples for future study, and to verify model findings under closed-loop control of pressure supply and apparatus stage tilt angle.

1.2 Thesis structure

1.2.1 Scope of the Thesis

This thesis is organized as follows:

Chapter 1 outlines the motivation and scope of the proposed air bearing slumping approach.

Chapter 2 continues with background information on X-ray astronomy and the theory of X-ray observatories, and articulate our general goal of achieving high-resolution, large-aperture X-ray telescopes.

Chapter 3 reviews recent mirror fabrication approaches used for generating X-ray telescope optics. By identifying the downsides of the past contact slumping method, non-contact slumping with air bearings proposed by SNL is introduced.

Chapter 4 describes my work of improving the slumping control system and glass surface wavefront reconstruction practice. A series of repeatability experiments have been accomplished with the improved tool to investigate the influence of thermal cycles, supply pressure, air film thickness and other contributing factors.

Chapter 5 builds mathematical models for both the air flow and the glass, and the concept of fluid-structure interaction comes into view. Finite element analysis with elastic and viscoelastic glass models have been performed, and both 2D axisymmetric model and 3D cylindrical model have been simulated, with various influencing parameters considered and studied.

Chapter 6 establishes credibility of our methods by comparing both simulation and experiments results, and conducting error analysis with quality measurements.

Chapter 7 points out possible directions for future work staring with my most recent vertical slumping experiments, while also making a statement about our achievements and concluding some of the important aspects about air bearing slumping.

1.2.2 Thesis Focus

The focus of this thesis is divided into three parts:

1. To improve the stability, controllability and robustness of the slumping tool; furthermore, to conduct a series of mirror fabrication experiments with the tool to study the repeatability and long term convergence of the resulting shape of the mirror under different experimental conditions.
2. To build a numerical model for the slumping process, especially to simulate the deformation of the mirror at the dwelling temperature; by identifying the contributing factors and understanding their influences, we could thus design a better parameter set and thermal cycles for future experiments with predictable results.
3. To combine both experiments and simulation results to confirm they are comparable with each other, and try to give a physical explanation by analyzing the output from both approaches.

The goal to generate good figure with thin mirrors is clear, yet the road is full of twist and turns. The efforts of my work could also be visualized in the following chart. In the following chapters, I'll go through the reasoning of our thought process, and explain each term in detail.

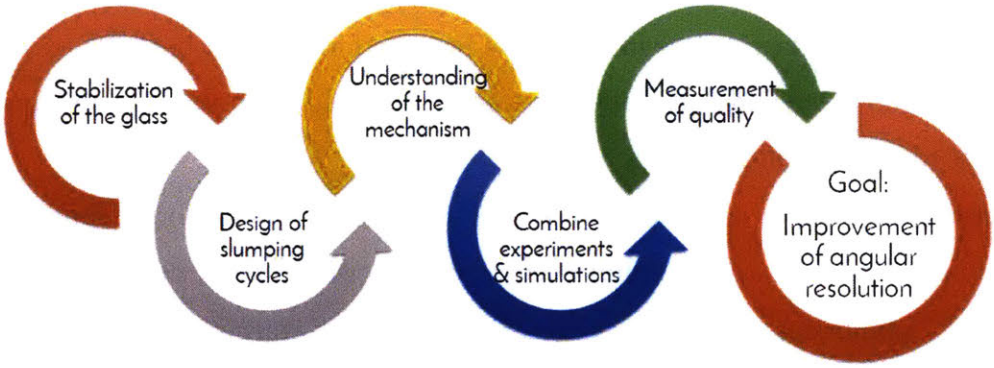

Figure 1-1: Efforts and accomplishments of my work.

Chapter 2

Background on X-ray observatories

2.1 X-radiation

X-radiation is a form of electromagnetic radiation. Most X-rays have a wavelength ranging from $0.01-10\,nm$, corresponding to frequencies in the range 30 petahertz to 30 exahertz ($3 \times 10^{16}-3 \times 10^{19}\,Hz$) and energies in the range $0.1-100\,keV$. X-rays with high photon energies (above $5-10\,keV$, below $0.2-0.1\,nm$ wavelength) are called hard X-rays, while those with lower energy are called soft X-rays.

The refractive index of X-rays is denoted as

$$n = 1 - \delta + i\beta, \tag{2.1}$$

where the real and imaginary components δ and β describe the dispersive and absorptive aspects of the wave-matter interaction. In general, δ is a very small number, so from the equation we see that x-ray refractive index tends to be slightly smaller than 1. This in turn gives rise to total external reflection at sufficiently small angles, with the critical angle defined as $\sqrt{2\delta}$, which is typically between $0.2°-2°$.

2.1.1 X-ray astronomy

X-ray astronomy is an observational branch of astronomy which involves X-ray observation and detection from astronomical objects. X-rays emitted from astronomical

objects that contain extremely hot gasses at temperatures in a range of a million Kelvin to hundreds of millions of Kelvin. It is the space science related to a type of space telescope that can see farther than standard light-absorption telescopes. Astrophysicists are interested in the X-ray band to study non-thermal processes, since the sky is not dominated by thermal emission from stars and diffuse astrophysical plasma, unlike lower-energy bands. These detectable non-thermal phenomena in hard X-ray includes the diffuse X-ray background, the up-scattering of lower-energy photons by relativistic electrons, and various nuclear and relativistic processes in stellar remnants, and pulsar and neutron star environments. [5] Figure 2-1 shows a comparison of different images that could be observed in various wavelengths from the Crab Nebula, a remnant of an exploded star.

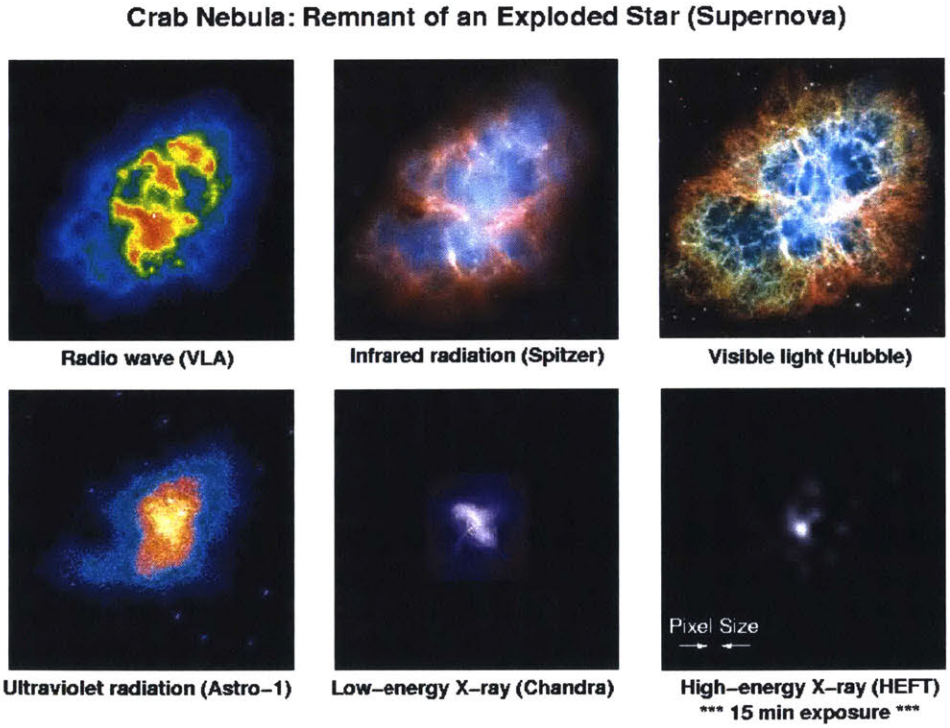

Figure 2-1: The Crab Nebula: a remnant of an exploded star, observed by different telescopes. [Credit: NASA HEFT (CM H. Chen)]

2.2 X-ray observatories

An X-ray telescope is a telescope that is designed to observe remote objects in the X-ray spectrum. Since the Earth's atmosphere is almost opaque to X-rays, X-ray telescopes must be mounted on high altitude rockets, balloons or artificial satellites. Figure 2-2 is about atmospheric opacity as a function of wavelength. In this graph, the level of the brown curve represents how opaque the atmosphere is at the given wavelength. The major windows are at visible wavelengths (marked by the rainbow) and at radio wavelengths from about $1\,mm - 10\,m$.

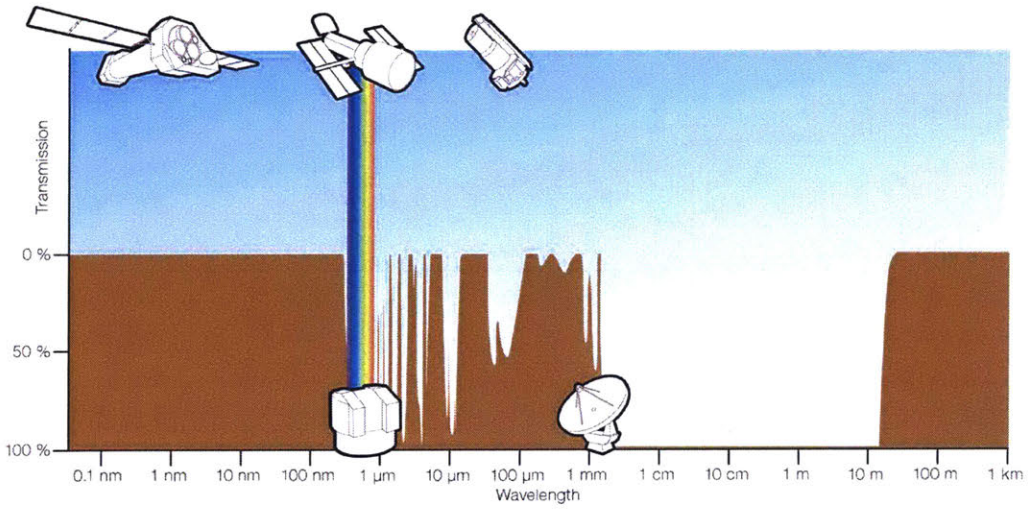

Figure 2-2: Atmospheric opacity graph. [Credit: ESA/Hubble (F. Granato)] [8]

2.2.1 Grazing incidence reflection of X-rays

Unlike visible light which could be easily redirected using lenses and mirrors, X-rays tend to initially penetrate and get absorbed in most materials without changing direction, because of their much higher frequency and photon energy. People have found very different techniques to redirect X-rays, most of which could only change the directions by only minute angles. The most common principle is to use reflection at grazing incidence angles, either by implementing total external reflection at very small angles or multilayer coatings, to reflect a beam of X-rays from a surface and to

measure the intensity of X-rays reflected in the specular direction.

Several designs have been used in X-ray telescopes based on grazing incidence reflection, including a set of widely used designs by Hans Wolter [28]. Wolter showed that a reflection off a parabolic mirror followed by a reflection off a hyperbolic mirror can lead to the focusing of X-rays, with an applicable wide field of view without suffering from extreme coma seen by using just one parabolic mirror. This is denoted as the Wolter Type I design, shown in Figure 2-3. Due to the tiny grazing incidence angles between the incoming X-rays with the tilted surface of the mirrors, the collecting area is rather small. Thus, nesting arrangements of thin mirror segments inside each other are used to increase the total collecting areas.

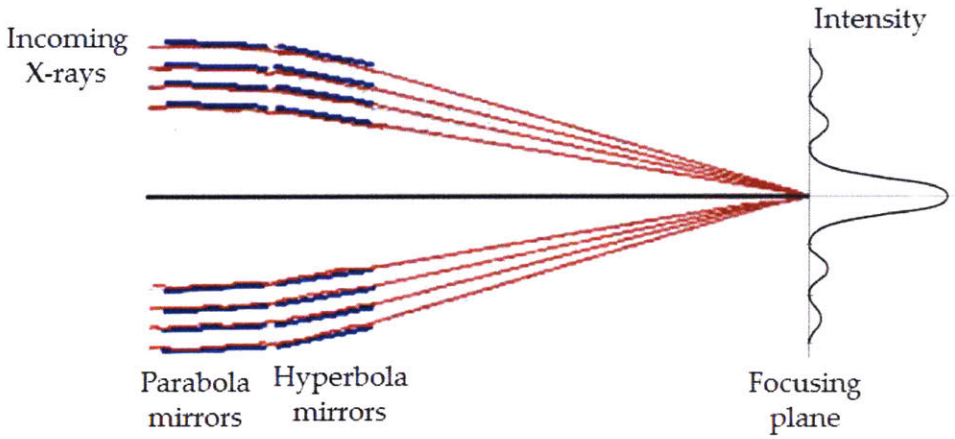

Figure 2-3: Wolter Type I telescope design.

2.2.2 History of X-ray telescopes

A rocket-borne experiment to obtain X-ray images from the sun was the first X-ray telescope to employ Wolter Type I design. [11]

Chandra X-ray Observatory (CXO) is one recent satellite X-ray observatory equipped with nesting Wolter Type I optics. Successfully launched by NASA in 1999, Chandra has operated for 18 years in a high elliptical orbit, returning thousands of high-resolution images and spectra of various astronomical objects in the energy bandwidth between $0.5-8\,keV$. Figure 2-4 shows the labeled diagram of the CXO.

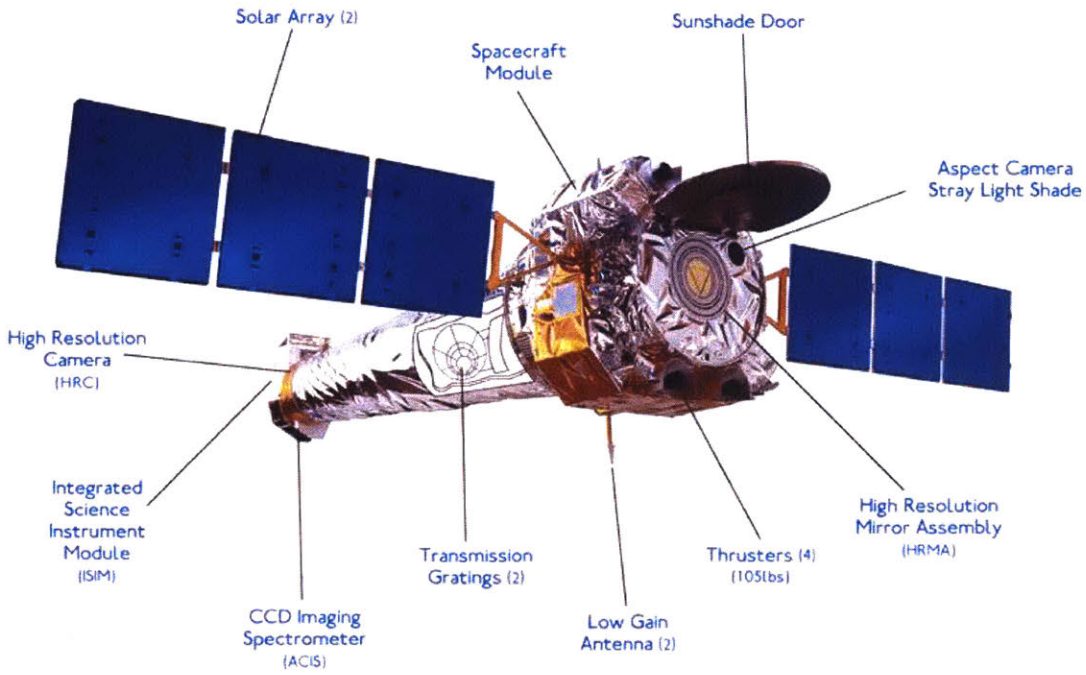

Figure 2-4: Labeled diagram of Chandra X-ray Observatory for soft X-ray sources. [Credit: NASA/CXC/NGST]

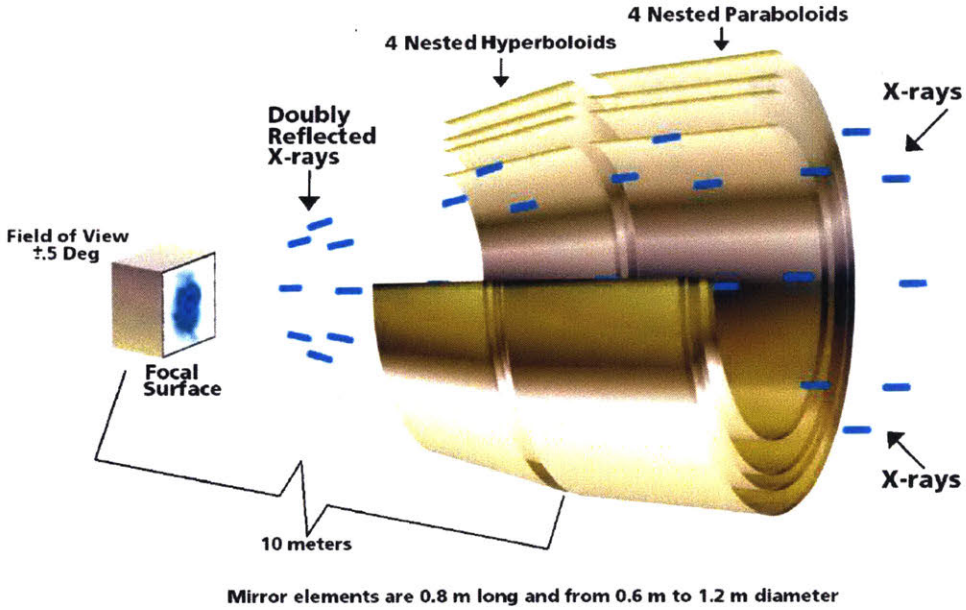

Figure 2-5: Cut-away schematic of Chandra. [Credit: NASA/CXC/ D. Berry]

Figure 2-5 is a schematic drawing of the Chandra X-ray Observatory's optic system. The major reflecting parts are made with four nested, co-axial, confocal, grazing-incidence parabolic and hyperbolic mirror pairs. The material for optics is ZERODUR from Schott, a lithium-aluminosilicate glass-ceramic, because of its low coefficient of thermal expansion and demonstrated capability of permitting very smooth polished surfaces. The manufacturing process involves grinding, polishing, and final smoothing. The thickness of the mirrors range from $16\,mm$ for the inner elements to $24\,mm$ for the outer ones. The total collecting area renders $0.04\,m^2$, with a fine angular resolution of $0.5\,arcsecond$ HPD. [25]

NuSTAR (Nuclear Spectroscopic Telescope Array) is another space-based X-ray telescope that uses Wolter Type I telescope to focus high energy X-rays from astrophysical sources in the range of $3-79\,keV$. Launched in year 2012, it conducts a deep survey for black holes a billion times more massive than the Sun and investigates how particles are accelerated to very high energy in active galaxies. Figure 2-6 is an artist conceptual drawing of the NuSTAR orbiting. It has two identical optics modules to increase sensitivity.

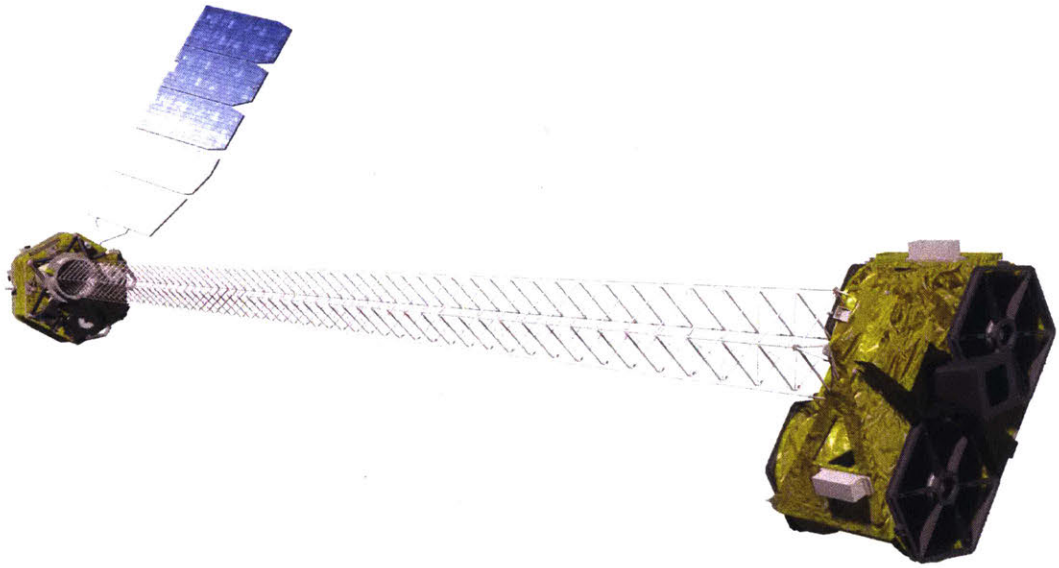

Figure 2-6: NuSTAR concept on orbit. [Credit: NASA/JPL-Caltech]

Almost all high-resolution X-ray telescopes utilize this similar geometry, but they

differ quite a lot in details, including mirror prescriptions, dimensions, and number of shells. Depending on those design details, the manufacturing and assembling procedure could be very different. [19]

2.3 Goals for future X-ray observatories

2.3.1 Tradeoffs between resolution vs. collecting area

The utilization of X-ray mirrors for X-ray astronomy simultaneously requires:

- the ability to determine the location at the arrival of an X-ray photon in two dimensions, i.e. high angular resolution;
- a reasonable detection efficiency, which requires large effective collecting area.

However, during the manufacturing process it's very hard to realize both requirements at the same time. Current X-ray telescope technologies are still quite limited in sensitivity and resolution, which limits our ability to study astrophysical phenomena in fine detail.

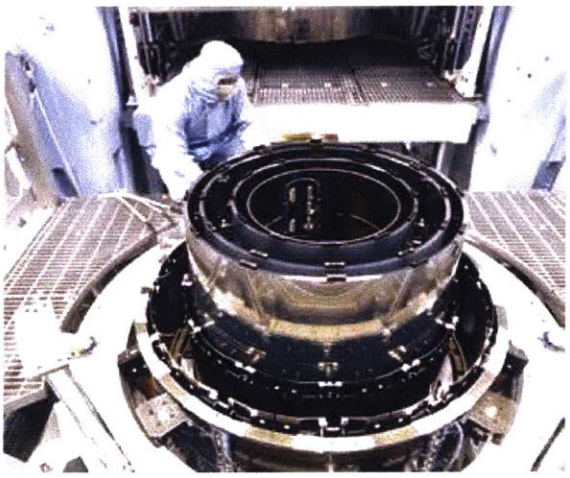

(a) Chandra, launched in 2009, has thick shells ($25\,mm$) with high resolution ($\sim 0.5\,arcsecond$ HPD) and small collecting area ($\sim 0.01\,m^2$). [25]

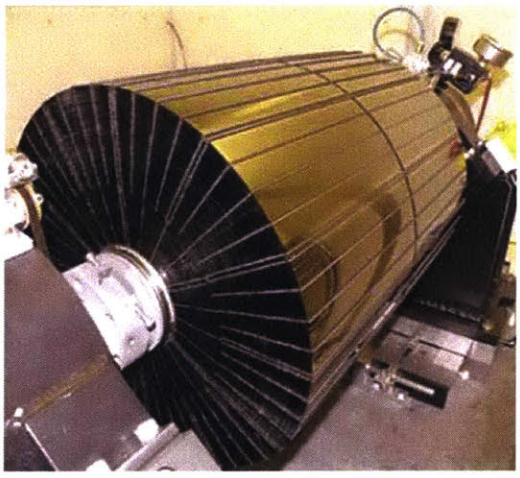

(b) NuSTAR, launched in 2012, has thin shells ($0.21\,mm$) with low resolution ($\sim 60\,arcsecond$ HPD) and large collecting area especially in hard X-ray region ($\sim 0.08\,m^2$). [13]

Figure 2-7: Trade-off between resolution and collecting area

When designing X-ray telescopes, we always encounter a competition between high angular resolution and large collecting area. For instance, Figure 2-7 compares Chandra and NuSTAR in terms both resolution and collecting area.

2.3.2 Goal: high-resolution, large-aperture X-ray observatory

Over the past 16 years, NASA's Chandra X-ray Observatory has provided an unparalleled means for exploring the high energy universe with its half-arcsecond angular resolution. Chandra studies deepen people's understanding of galaxy clusters, active galactic nuclei, normal galaxies, supernova remnants, planets, and solar system objects, as well as advance our understanding of dark matter, dark energy, and cosmology. The key to Chandra's success is its $0.5\,arcsecond$ resolution, but it's also clear that many Chandra observations are photon-limited. [24]

A successor to Chandra with comparable angular resolution and greatly increased photon throughput is the Lynx Mission (previously named X-ray Surveyor Mission), a large strategic mission concept identified in the 2013 Enduring Quests, Daring Visions NASA Astrophysics Roadmap [14]. It will host an X-ray telescope with an effective area of more than $1\,m^2$ at X-ray energy band $1\,keV$, and a $15\,arcminutes$ field-of-view with $1\,arcsecond$ or better half-power diameter resolution. Figure 2-8 shows a concept drawing of this mission.

It's not trivial to address our fundamental goal of producing high-resolution, large-aperture x-ray observatories. W. Zhang [32] outlined 5 steps in making X-ray telescopes:

- Substrate fabrication;
- Coating;
- Alignment;
- Bonding;
- Module design, analysis, engineering and testing.

The making of a mirror assembly starts with the making of many mirror substrates, which is also what this thesis is mainly about. Unlike the thick bulk material used for Chandra, we prefer thin segmented mirrors to reduce blockage and nested

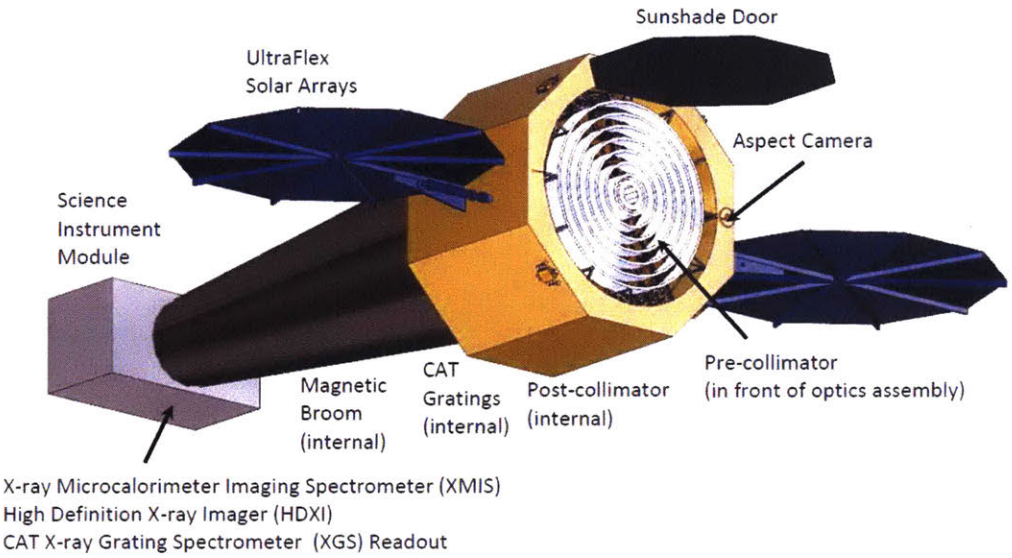

Figure 2-8: Artist's conception of the Lynx (former X-ray Surveyor) baseline mission concept. [10]

mirrors to increase collecting area. After an integrated consideration of the mass, thermal and mechanical properties that could satisfy the telescope design, nowadays people mainly use two materials for the mirror substrates: borosilicate glass and single crystal silicon. In this thesis, I'll only discuss technologies for manufacturing thin glass mirrors.

Chapter 3

Introduction to slumping (thermal shaping of glass)

3.1 X-Ray mirror technology

Traditional grinding and polishing techniques for shaping thick optics, such as lenses we have seen in most labs and the thick shells in Chandra, won't work for ultra thin optics that we'd like to work on in X-ray telescopes, because thin optics suffer excessive deformation and stresses under grinding. This leads us to seeking novel methods for manufacturing thin mirror substrates. Up to now, people have devised primarily four fabrication technologies which have successively promoted the progress towards high-resolution X-ray telescopes. The aforementioned methods are: electrolyse nickel-cobalt replication [22], silicon pore optics [6], slumping glass [29, 30, 27], and polishing single-crystal silicon [31]. Before NASA GSFC invented the new polishing single-crystal silicon technique, slumping glass is currently the most accurate optical replication process for segmented thin optics and has been effectively used to fabricate mirrors of NuSTAR.

3.1.1 Contact slumping

The slumping process used for NuSTAR at NASA Goddard Space and Flight Center is as follows:

- A sheet of glass is placed on top of a cylindrical mandrel[1] in an oven.
- Then the oven is heated and the temperature gradually increases to about $600°C$, when glass sheet softens and gravity forces the glass to conform to the mandrel to replicate its shape.
- After that, the oven is cooled down, and the glass solidifies while maintaining the conformed shape.

This process is further on referred to as contact-slumping, and is illustrated in the Figure 3-1. It allows for generation of glass mirrors with excellent fidelity at long spatial wavelengths ($> 1\,cm$), with a best resolution of $\sim 7\,arcsecond$ HPD as described by W. Zhang [29]. However, it also suffers from a few major drawbacks:

1. First, since the glass firmly contacts the mandrel during the slumping process, any dust particulates captured in between the two surfaces will imprint on the surface of the glass and create dimples on the range of $0.05-1\,mm^{-1}$, which is referred to as mid-range spatial frequency errors. This will impose a harsh problem to the final resolution of the mirrors, and errors in this range are very hard to remove after being generated.
2. To potentially avoid dust problems, people have tried to get both surfaces of the mandrel and glass ultra cleaned before slumping. However, in this way they will stick to each other after cooling down. To avoid fusing of the mandrel and glass, a release layer is introduced between them as anti-sticking coatings. NASA NSFC used boron nitride to coat the fused quartz mandrel for NuSTAR. The coatings allow the glass to be removed from the mandrel, but they also tend to clump rather than staying uniformly distributed on the bearing surface,

[1]To be more accurate, the mandrel is cylindrical along the azimuth direction, but hyperbolic or parabolic in the radial direction. This follows the design of Wolter Type I telescopes.

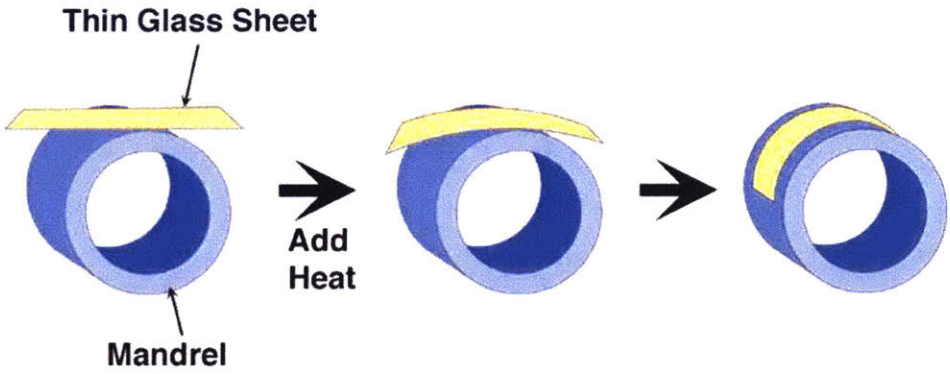

(a) Contact slumping process

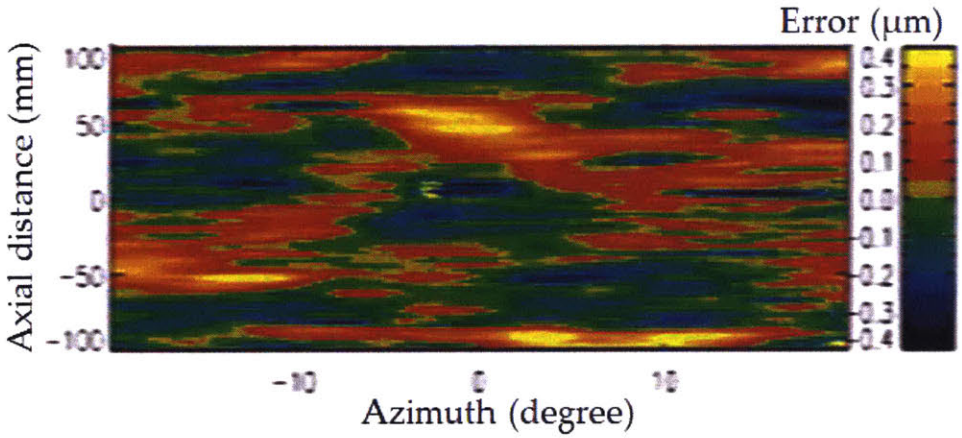

(b) Surface height error of a slumped substrate of NuSTAR mirrors

Figure 3-1: NuSTAR (Nuclear Spectroscopy Telescope Array) mirror fabrication at NASA GSFC [29]

which causes the glass to exhibit dimples, also creating substantial mid-range spatial frequency errors in the surface profile.

3. Another downside is caused by the thermal asymmetry between two surfaces of the glass: on one side the glass is contacting air, while on the other side the glass is touching the solid mandrel. During the solidification of the glass, if the cooling speed is too fast, the different thermal properties of the mandrel and air on the two sides of the glass would result in stress asymmetry between the two surfaces of the mirror, causing the mirror to curl up and lose its fidelity. Thus to minimize temperature gradients from one side of the glass to the other as the glass solidifies, the cooling time has to be long enough. The total thermal

cycle at NASA NSFC takes more than 50 hours.

Given so many dissatisfactions of contact-slumping, different groups around the world have devised a variety of solutions on top of the status quo. Contact slumping with pressure assistance is proposed by European Space Agency as an alternative for the ATHENA Mission in addition to the baseline solution based on Silicon Pore Opitcs. They apply pressure to the glass during hot slumping to ease the mould shape replication and to enhance the ripple relaxation. [23] Another effort by Harvard-Smithsonian Center for Astrophysics is called adjustable grazing incidence X-ray optics, which applies piezo-electric actuators to slumped thin glass foils to reach sub-arcsecond resolution under the context of the Lynx Mission. [21]

Considering the good long-range spatial frequency errors correcting potential as well as the unresolved mid-range frequency errors that contact slumping endures, our group at MIT SNL has devised the idea of non-contact slumping using air bearings, which could produce thin-shell mirrors devoid of mid-range spatial frequency errors, and with lower cost mandrels and quicker processing time that would significantly reduce manufacturing costs.

3.1.2 Non-contact slumping using air-bearing slumping

In non-contact slumping, a set of porous mandrels allow air to pass through and create two thin layers ($15-50\,\mu m$) of air flow. The mirror sits between two thin air films, supported by the viscous creeping flow of air. Then the system is heated to temperature slightly higher than the glass strain point, allowing for enough viscosity for the glass to replicate the perfect mandrel figure without directly contacting with the mandrel surface. Figure 3-2 depicts the air bearing slumping process.

The advantages of non-contact slumping are:

- Air flow could sweep away dust particles, and air films thickness is larger than the typical dust particle size in clean room environment (less than $10\,\mu m$), so mirrors won't be touching any of these particulates.
- It avoids using non-stick coatings, so mirrors generated from this method are

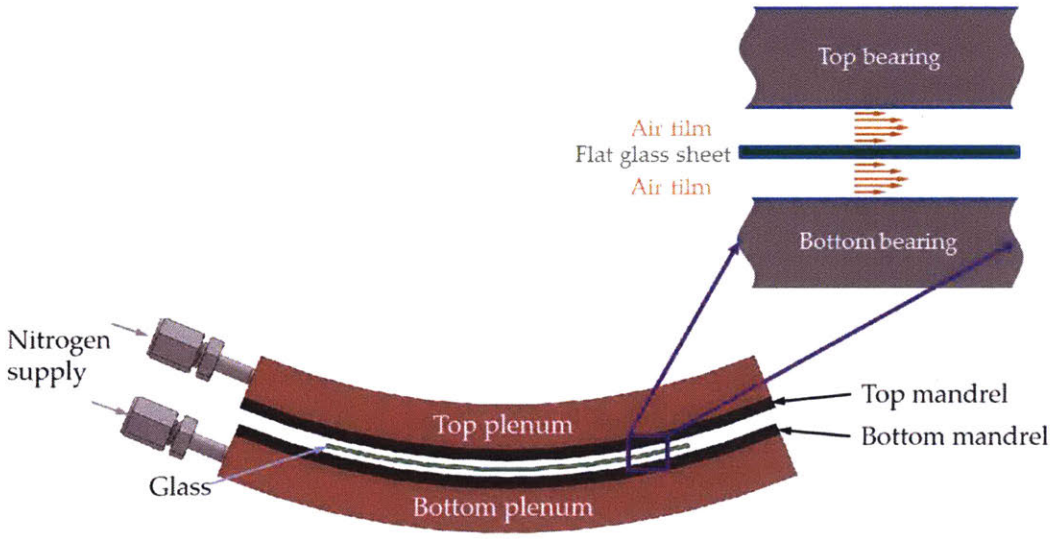

Figure 3-2: Illustration of air bearing slumping process (not drawn to scale). Hot glass sheet is suspended by two cushions of air film created by opposing porous air bearings.

free from mid-spatial frequency errors.

- The medium on both sides of the glass is the same — air, with the same thermal mass, so they would exhibit the same heating and cooling rates, resulting in a very high degree of thermal symmetry, thus enabling much more rapid slumping cycles.

Figure 3-3 compares non-contact slumping vs. contact slumping. Dust or anti-stick coatings on mandrels generate bumps in the glass in contact slumping, while non-contact slumping avoids direct contact with mandrels thus avoids creating mid-range frequency dimples in the glass.

The goal with non-contact slumping at SNL is to produce mirrors with low mid-range frequency errors, even at the cost of creating certain amount of long-range spatial frequency errors. The idea is mir-range errors are the hard to remove, yet long-range errors could be eliminated with some figure correction methods. Our lab is developing one such correction technique "ion implantation" which scans ion beams with energy of mega electron volts over mirror surfaces to impart position-dependent stress thus removing long-range spatial frequency errors.

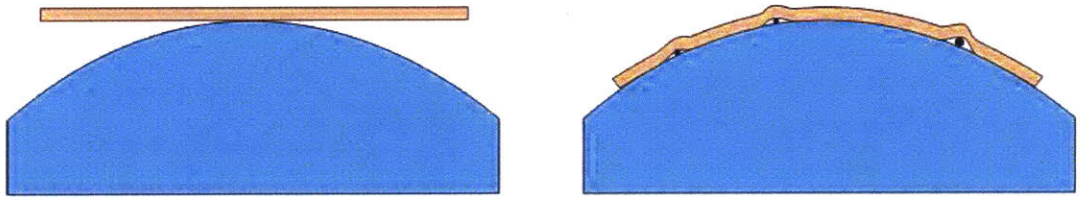

(a) Contact slumping

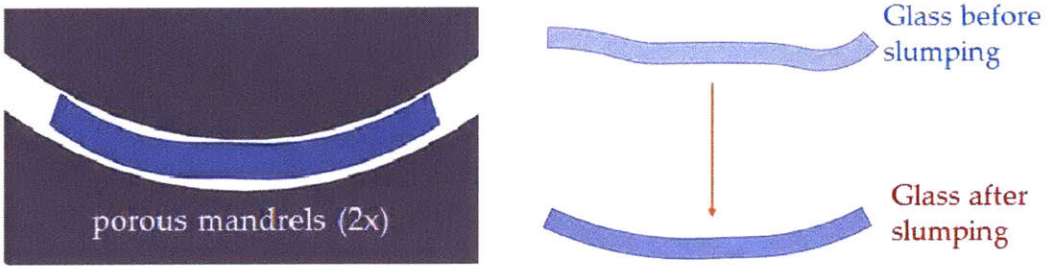

(b) Non-contact slumping

Figure 3-3: Comparison between contact-slumping and non-contact slumping. Top: Dust / anti-stick coatings on mandrels generate bumps in the glass in contact slumping. Bottom: Non-contact slumping avoids direct contact with mandrels thus avoids creating mid-range frequency dimples in the glass.

3.2 Non-contact slumping set-up at SNL

3.2.1 Slumping tools

Initial experiments in thermal shaping of glass at our lab began in the mid-2000s, with focus on single-sided metal and ceramic mandrels with machined holes and grooves for air delivery [1]. After that, double-sided mandrels of porous ceramics were developed. The work in the past has been focused on slumping flat round glass wafers with flat porous bearings. The reason why we work on flat bearings first is mainly out of manufacturing concerns: it's rather hard to manufacture a set of cylindrical bearings[2], in spite of the choice of materials; but it's relatively easy to manufacture a pair of flat bearings.

Figure 3-4 shows the slumping tool set-up in our lab for flat glass sheets.

We use high hardness silicon carbide (SiC) as the material for both porous bearing mandrels and plenum chamber, which are made separately and bonded together by

[2]Same as the above note

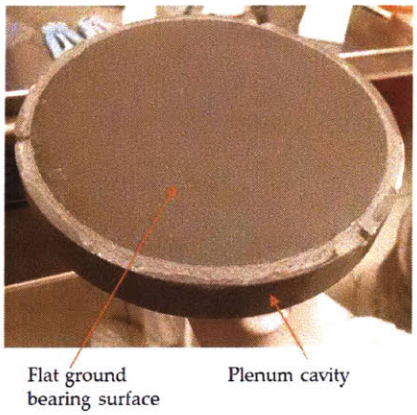

(a) Silicon carbide mandrel with integrated plenum and pressurized nitrogen port

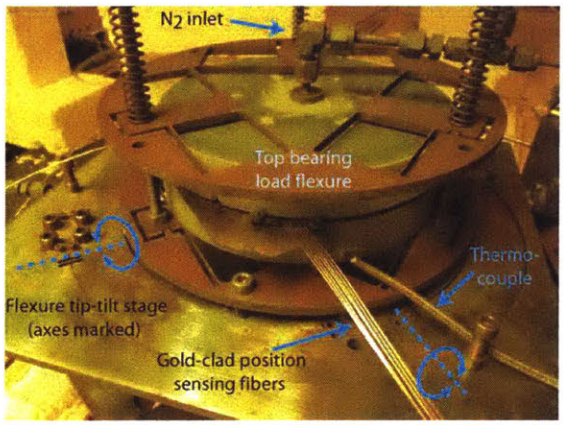

(b) A pair of opposing mandrels in a stainless steel and Inconel sensor/actuator structure

Figure 3-4: Current slumping tool set-up in our lab for flat glass sheets.

high-temperature SiC adhesive to ensure the same thermal expansion coefficients. Mandrel surfaces are spaced apart by three Kovar[3] shims of thickness $600-650\,\mu m$ to create a gap of $25-50\,\mu m$ on each side of the glass that is much larger than typical dust particles. This ensures that ripples and dimples caused by particles are no longer present. This whole structure is placed in an oven. All the mechanical components we use here are made of stainless steel, titanium or Inconel that could sustain high temperature.

The functionality of different parts of the slumping tool are:

- The sandwiched bearing-glass assembly is placed on top of a flexure tip-tilt stage that could move the bearing in two horizontal directions;
- Two sets of gold-clad fibers are placed on top of the stage to measure the horizontal glass position;
- Three pneumatic bellows attached to the tip-tilt stage are actuated by by air to control glass position;
- Pure nitrogen is continuously supplied into the inlet through stainless steel tubing, effectively generating a pressure distribution in both bearing cavities;

[3]Kovar is a nickel–cobalt ferrous alloy which has the same thermal expansion characteristics as borosilicate glass that enables a tight mechanical joint between two contacting materials over a range of temperatures.

- Three thermal couples are used to measure the temperature around the structure at different locations.

The pressure load on the two porous air-bearings could vary according to our need, currently in the range of $0.015-0.1\,psi$ or $103-690\,Pa$. The thickness of the air films could also be tuned to match our requirements.

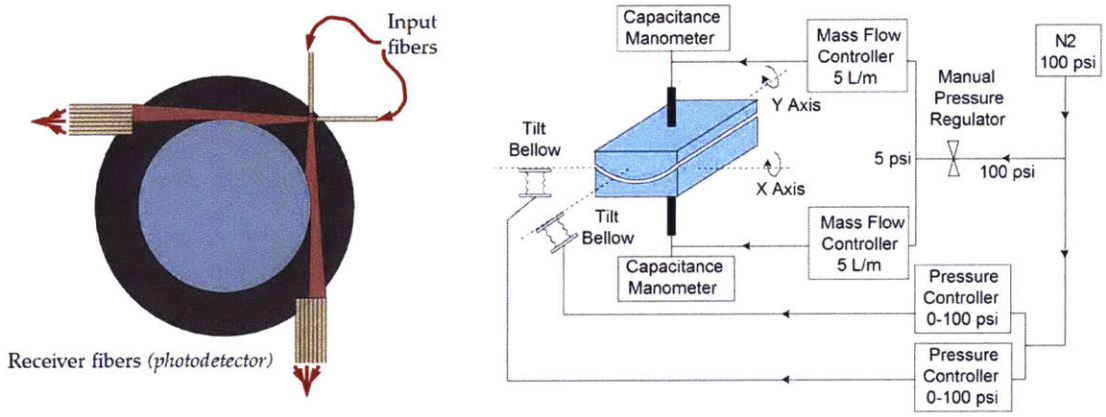

(a) Two set of gold-clad optical fibers sense the location of the wafer inside the bearing.

(b) Schematic of nitrogen control system.

Figure 3-5: Depiction of slumping tool control system

Figure 3-5 shows the slumping tool control system. (a) For glass location sensing, we use two sets of optical fibers to send and receive light in two perpendicular directions. For each direction, the light blockage is a function of the mirror position, and this relationship is approximately linear. This technique allows us to deduce the position of the glass by measuring the intensity from the receiving fibers, and it has a huge advantage because of its simplicity. (b) After obtaining information about the glass position, we could control the glass position by inflating Inconel bellows to tilt the bellows attached to the stage. Bearing plenum pressures are controlled using capacitance manometers and mass flow controllers.

3.2.2 Annealing of glass

The process of slumping is very much related to the stress relaxation of the glass objects. From a raw substrate to a formed mirror, we not only want the glass to

replicate the desired shape, but also need to relieve the internal stress inside the glass, so it won't deform further under no external forces while fulfilling its roles. This brings up the topic of annealing of glass.

Annealing is a process of slowly cooling hot glass objects to relieve residual internal stresses introduced during manufacture. As the temperature increases, glass will soften and transit from a hard and relatively brittle state into a viscous or rubbery state. During this process, its liquid viscosity tends to decrease and its fluidity tends to increase.

Unlike crystalline materials have a single transition temperature that characterizes the phase change, the glass-transition temperature is characterized by a range of temperatures over which this glass-to-liquid transition gradually occurs. At such stage, the glass is still hard enough to take on significant external deformation without fracture, but it is also soft enough to relax internal strains through internal microscopic flow. To describe the glass transition phenomenon, several conventions are defined by either a constant cooling rate (for instance $20\,K/min$), or a viscosity threshold (for instance $10^{12}\,Pa \cdot s$).

Williams-Landel-Ferry model

The Williams-Landel-Ferry model [26] is used to describe the temperature dependence of liquid viscosity of materials that have a glass transition temperature.

The model is:

$$\mu(T) = \mu_0 \exp\left(\frac{-C_1(T - T_r)}{C_2 + T - T_r}\right) \tag{3.1}$$

where T is temperature, T_r is a reference temperature related to the glass transition temperature T_g, and C_1, C_2 and μ_0 are empirical parameters with only two of them being independent. These parameters are determined by fitting of discrete values through experiments for different materials.

Figure 3-6 shows the logarithm of viscosity versus temperature for fused silica, high silica, borosilicate and soda-lime glasses. On the vertical axis, several specific points important to the fabrication and processing of glass are labeled. [4]

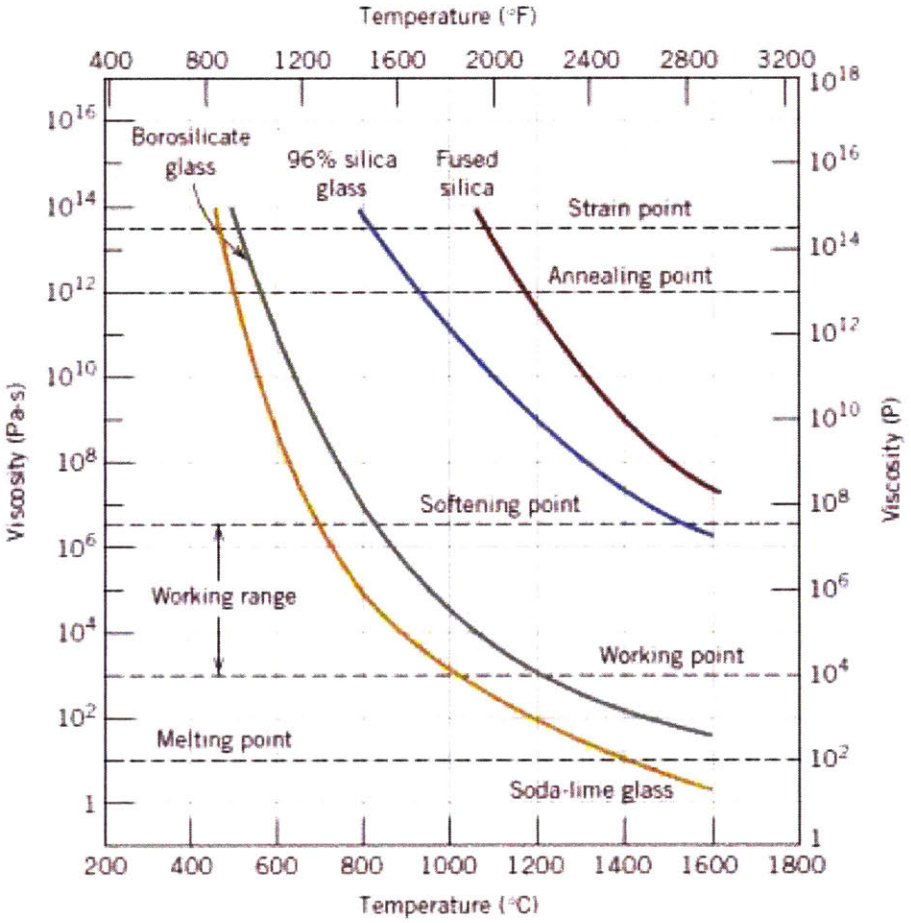

Figure 3-6: Logarithm of viscosity versus temperature for fused silica and three silica glasses. [4]

Viscosity of Schott D 263 glass

The substrate material we use for slumping is Schott D263, a colorless borosilicate glass that SCHOTT manufactures with the help of a special down-draw method. Some of the technical details for this material are shown in Table 3.1.

3.2.3 Thermal cycles

Before we start working on the slumping tool, we need to decide what thermal cycles we would like to impose. Typically there are three stages in a cycle: ramping stage, dwelling state, and cooling stage. Ramping stage is the heating period, during which

Table 3.1: Key temperature points for Schott D 263 glass. [12]

Name	Temperature	Corresponding viscosity	Explanations
Strain point	$529°C$	$10^{13.5}\,Pa \cdot s$	Transition starts here. Below this point fracture occurs before plastic deformation. Internal stresses could be relieved within a few hours at this point.
Annealing Point	$557°C$	$10^{12}\,Pa \cdot s$	Atomic diffusion is sufficiently rapid to remove any internal stresses within a few minutes at this point.
Softening Point	$736°C$	$10^{6.6}\,Pa \cdot s$	Maximum temperature at which glass could be handled without causing significant dimensional alterations.

we gradually heat the glass inside the oven from room temperature to a temperature higher than the softening point of the glass. Then comes the dwelling stage, at which the temperature inside the oven is maintained constant, such that the glass could deform while releasing the internal stresses. After that we cool the system down to room temperature again and finish one thermal cycle.

Following this scheme, there are in principle three parameters we need to decide on: ramp time, dwell time and dwell temperature. Considering the long-term durability of our slumping tool, as well as the minimum requirements for glass transition, we both don't want to operate our system at a very high temperature that may potentially damage our tools, but also need to heat the glass to at least the strain point. So we finally choose to work around $550°C$, just above the strain point for D263 glass. This is considerably lower than other groups doing contact slumping, which typically have glass slumped around $600°C$, almost reaching the softening point. Due to this reason, we need to dwell at our peak temperature longer compared to other groups. In our experiments, we have tried to tune the dwell time from $0.1-100\,h$.

However, even having a slightly longer dwelling stage, we could still bring down

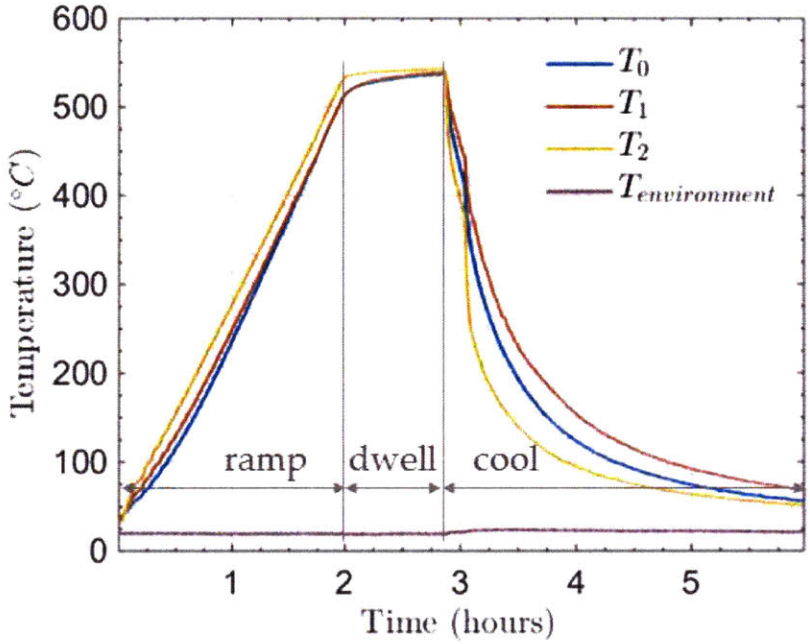

Figure 3-7: Thermally symmetric tool design allows short, relatively cool slumping cycles.

the total slumping time (three stages included), because we could implement much shorter ramping and cooling stages. As described earlier, this is the advantage of non-contact slumping, to have air surrounding the glass to create a thermally symmetric system. So the thermal expansion rates on both surfaces of the glass are the same, and this allows us to implement much more rapid heating and cooling.

Figure 3-7 shows the actual records of the thermal couples obtained from one of our experiment. Compared to the $50\,h$ contact slumping time, we could reduce this to 10 times shorter.

Chapter 4

Recent slumping tests and experiments

4.1 Improvement of the control system

Does the glass tend to stay inside the bearing during slumping? The answer is no, especially for the flat bearing system we use now. Study of fluid mechanics tells us that the central position inside the bearing is an unstable equilibrium point, such that any deviation from this position will only encourage further deviations. So in reality air flow will try to push the glass out of the bearing almost at no time. To solve this, we need a very good glass position control system.

During the past year, I installed more accurate and reliable fiber sensors, and implemented a better position controller as shown in Figure 4-1.

The process of implementing the proportional–integral–derivative controller (PID controller) to control glass position includes:

1. Conduct system identification (SID) tests to measure frequency responses for X and Y direction separately;

2. Fit the measured frequency responses to a second order system:

$$G(s) = K_p \frac{\tau_{lag} s + 1}{s} \frac{\alpha_{lead} \tau_{lead} s + 1}{\tau_{lead} s + 1}; \tag{4.1}$$

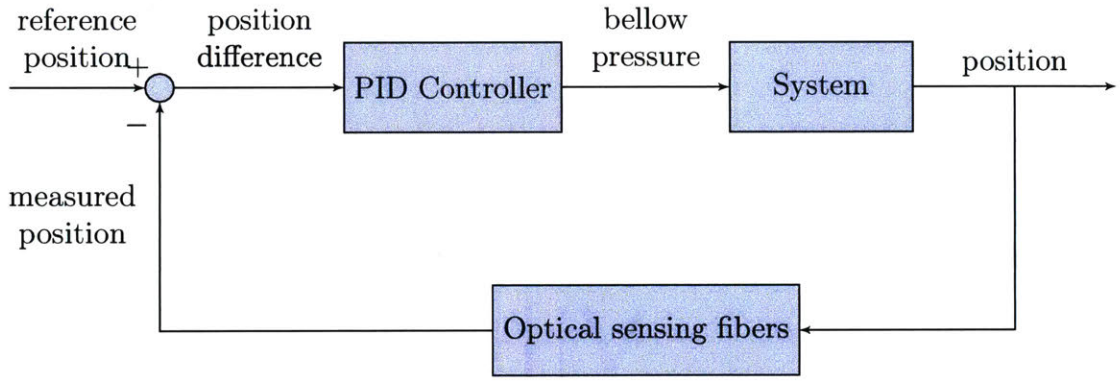

Figure 4-1: Control diagram

3. Consider temperature influence and conduct the above SID tests at different temperatures;
4. Introduce a reference sinusoidal signal in each direction to constantly shift the glass in circular movement during slumping;
5. Integrate into a control algorithm with LabVIEW.

These have resulted in a number of benefits, including much higher system reliability, fewer glass crash events, quicker slumping set-up, and more consistent run-to-run results.

4.1.1 Implementation of more reliable optical sensing fibers

During our experiments, it's crucial to have stable optical sensing fibers so that measurements from different runs could be comparable. To establish the stability of optical fibers, I baked two sets of fibers - nickle-coated and gold-coated optical fibers - in the oven for the same amount of time and measured their intensity. Then I repeated such tests for three times and compare the degradation of the fiber intensity.

Figure 4-2 shows the results of these tests. During these tests, three nickel-coated fibers and three gold-coated fibers were tested, while another nickel-coated fiber was chosen to be the control group that wasn't heated in the oven. In Figure 4-2 all nickel-coated fibers are denoted with stars while all gold-coated fibers are denoted

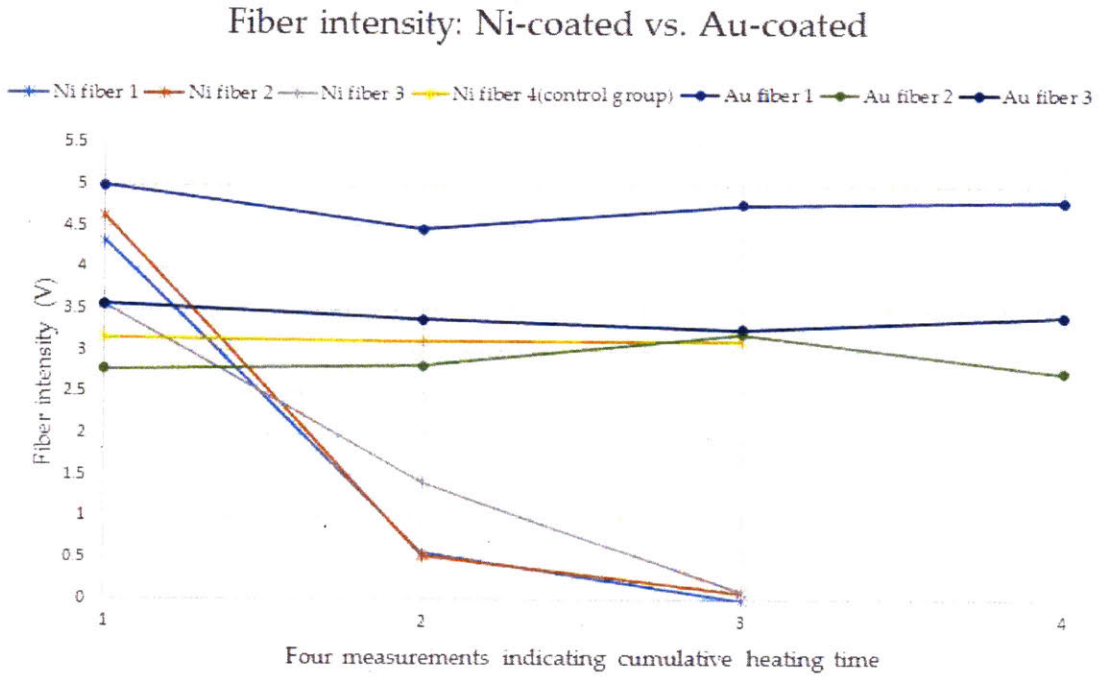

Figure 4-2: Test fiber intensity vs. cumulative heating time for Ni-coated fibers (denoted by stars) and Au-coated fibers (denoted by circles). Note: difference in intensities among same type of optical fibers come from different fiber cross-section cutting quality. Since we cut all the fibers with Ruby cutters by hand, despite our effort to maintain similar cutting surface, it's still hard to have them exactly the same.

with circles. The six fibers underwent a total of four measurements during the whole experiment. The first measurement occurred before heating. The second measurement occurred after the first heating cycle in the oven, during which more than 60% of intensity loss were observed in nickel-coated fibers, while gold-coated fibers showed almost no change in intensity. The third measurement occurred after the second heating cycle in the oven, after which the intensity of all three nickel-coated fibers dropped to nearly zero, while gold-coated fibers and control group nickel-coated fiber all maintained the original intensity. So I heated only three gold-coated fibers during the third heating cycle, and their intensity were very stable.

This shows gold-coated fibers have superior stability even at very high temperature. So I switched from nickel-coated fibers and equipped our slumping tool with

gold-coated optical fibers.

4.1.2 System identification tests

To have a system transfer function, we conducted a series of SID tests from the input sinusoidal reference position to the output actual glass position.

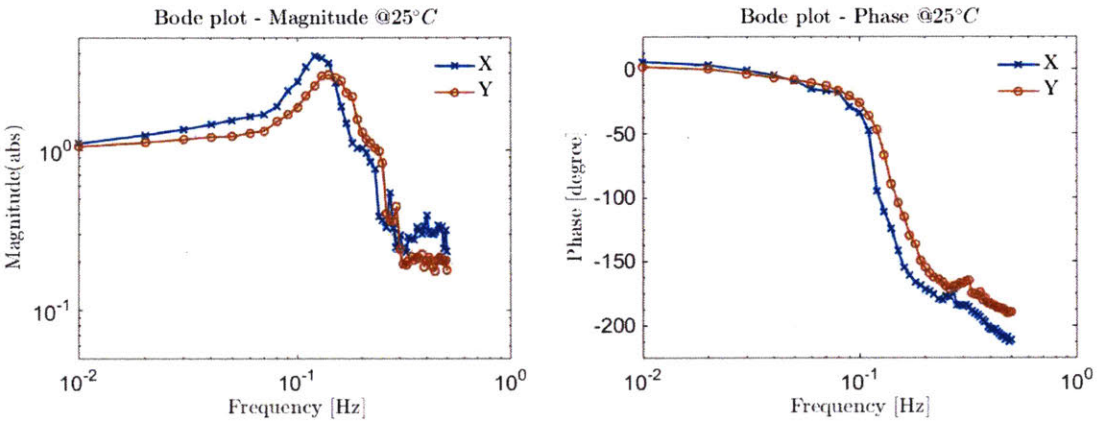

(a) Magnitude (b) Phase

Figure 4-3: Measured system transfer function at $25°C$

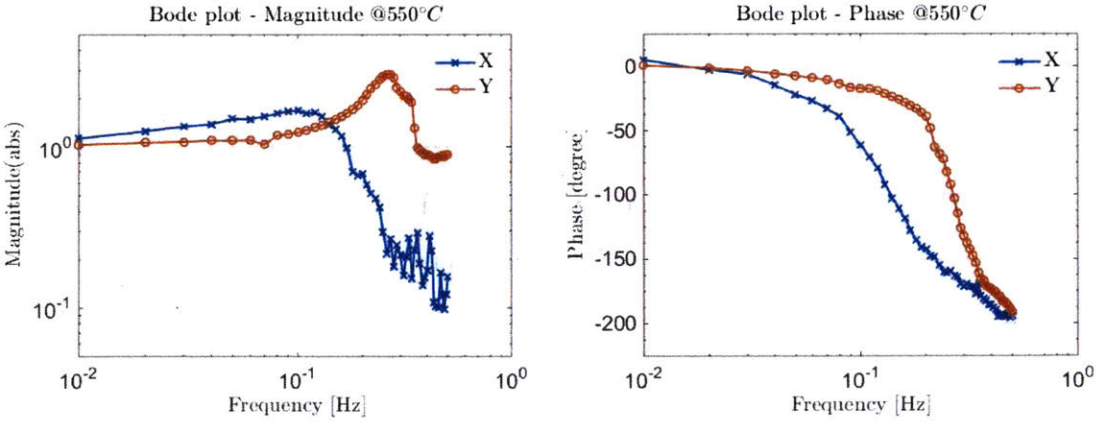

(a) Magnitude (b) Phase

Figure 4-4: Measured system transfer function at $550°C$

Tests have been carried out under three temperatures $25°C$, $400°C$, $550°C$ and a wide range of frequencies $0.01-1Hz$. Figure 4-3 and Figure 4-4 show the measured system transfer function at $25°C$ and $550°C$.

From these plots, we discovered the following facts:

- Despite the temperature and direction, large noise always appears at frequency above $0.1\,Hz$, and the system loses control at $1\,Hz$;
- There is obvious directional difference in the frequency response, which we believe is primarily caused by the asymmetries of the tip-tilt stage;
- X magnitude decreases in general as temperature increases, yet its resonant frequency doesn't show much change;
- Y magnitude doesn't decrease much as temperature increases, yet its resonant frequency becomes significantly larger.

Furthermore, the measured transfer function could be fitted to a second-order system

$$\frac{A_0\omega_n^2}{s^2 + 2\zeta\omega_n s + \omega_n^2}. \tag{4.2}$$

Figure 4-5 and Figure 4-6 show the Bode plot of the fitted system transfer function. From the data we could see there is noticeable change in the natural frequency ω_n and damping ratio ζ as temperature increases.

4.1.3 Substrate dithering with reference signals

Before we had the new controller, we've encountered enormous difficulties in stabilizing the glass position between the bearing. We tried to control the glass in the same spot inside the bearing, however sometimes the glass shifted out of the bearings but we couldn't tell, because in such cases the intensity of the position sensing optical fibers were unchanged. Therefore, compared to having the substrate held steady at one spot, we prefer to have it follow a regular reference movement, such that any deviation from this regular movement would imply an undesirable change in the substrate motion.

To do this, we intentionally introduced a reference sinusoidal signal in each direction such that the glass could constantly dither inside the bearing during slumping. The frequency of the reference is $0.01\,Hz$ in both X and Y directions, while Y has

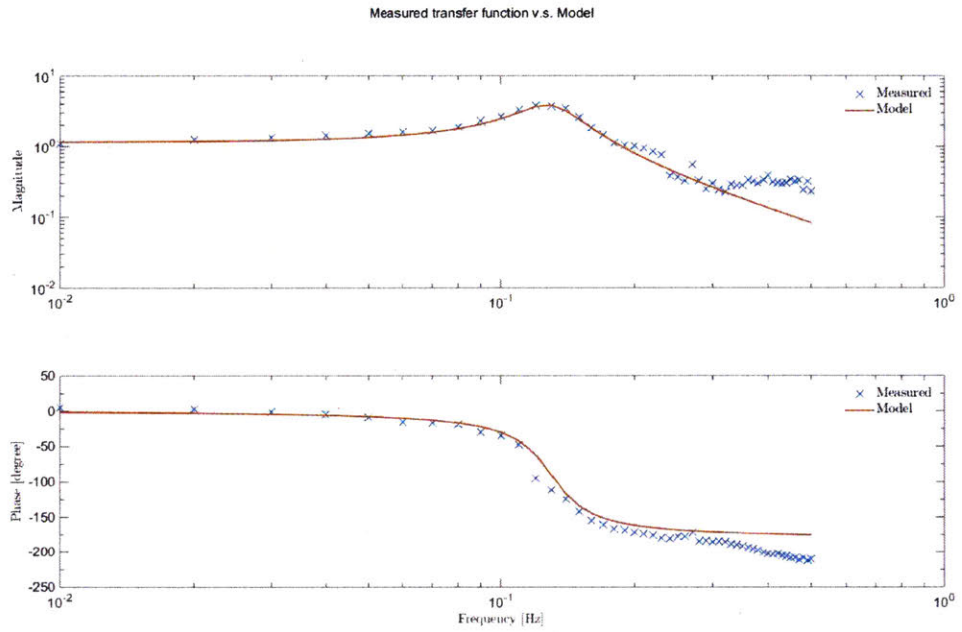

(a) X: $A_0 = 1.15, \omega_n = 0.13 \times 2\pi, \zeta = 0.15$

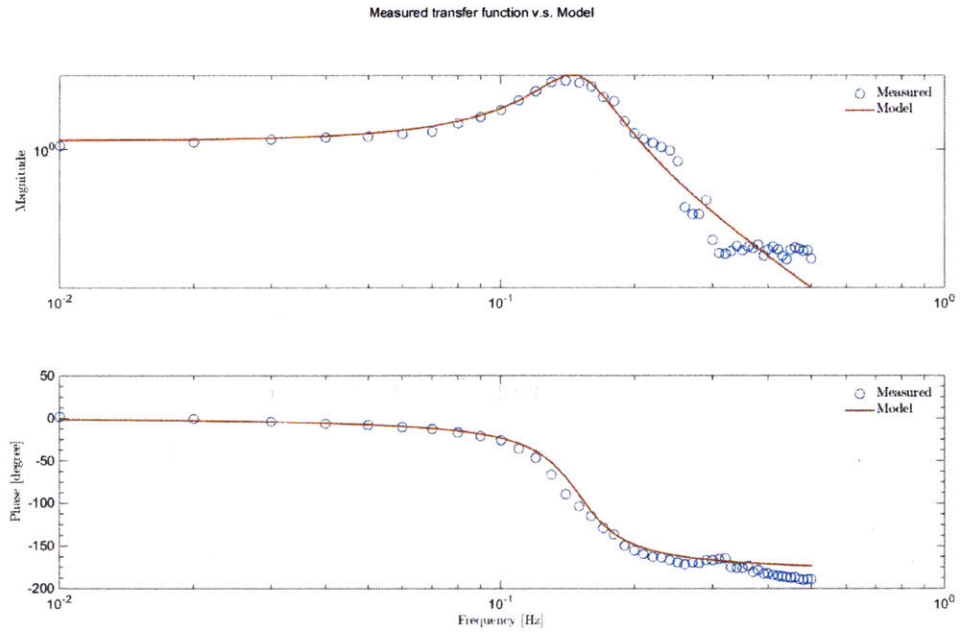

(b) Y: $A_0 = 1.15, \omega_n = 0.15 \times 2\pi, \zeta = 0.18$

Figure 4-5: Fitted system transfer function at $25°C$

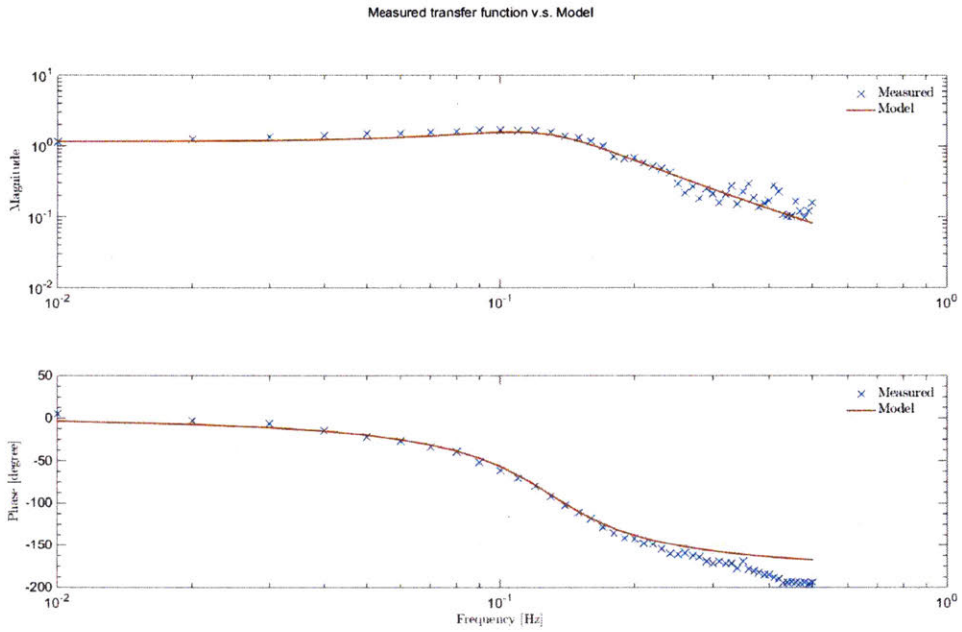

(a) X: $A_0 = 1.15, \omega_n = 0.13 \times 2\pi, \zeta = 0.4$

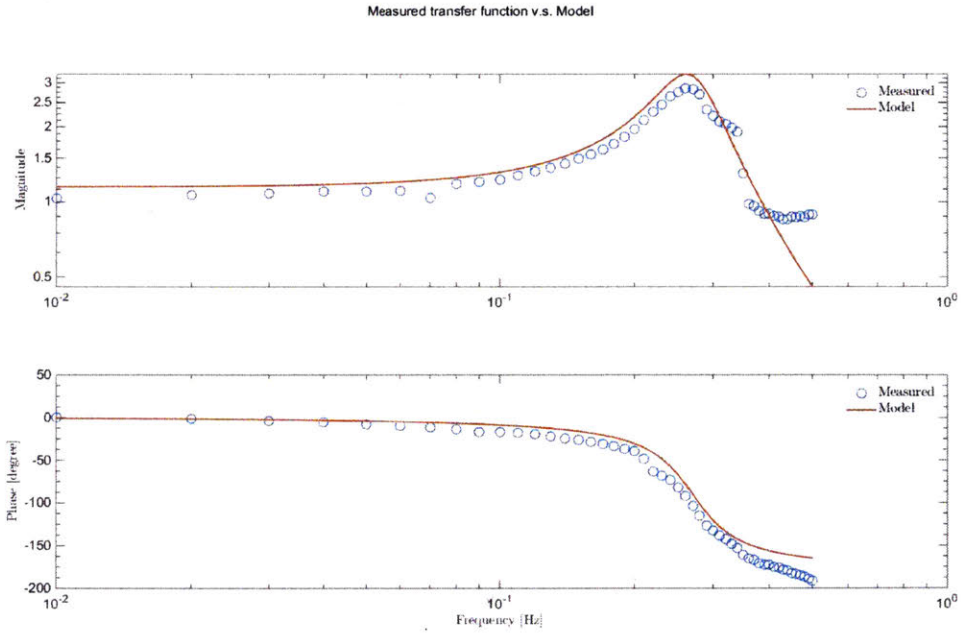

(b) Y: $A_0 = 1.15, \omega_n = 0.27 \times 2\pi, \zeta = 0.18$

Figure 4-6: Fitted system transfer function at $550°C$

a phase lag of $\pi/2$ compared to X, so the glass could follow a circular movement. Figure 4-7 shows a real-time measurement of such dithering.

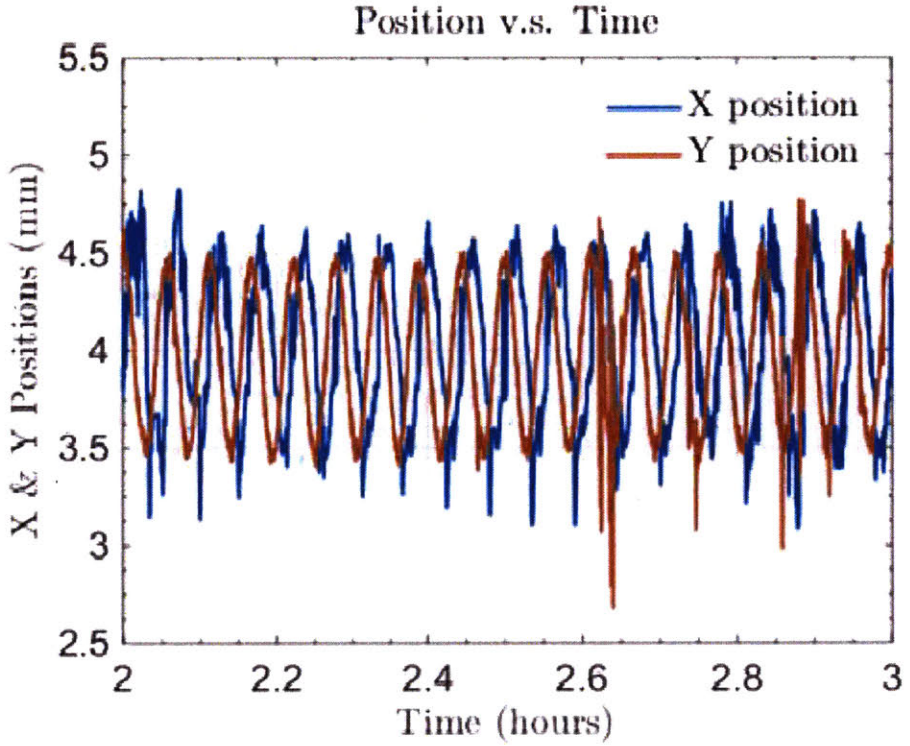

Figure 4-7: Measured glass position following a sinusoidal reference in both X and Y with frequency $0.01\,Hz$ amplitude $1.5\,mm$.

4.1.4 Integrate into a controller in LabVIEW

Finishing the above steps, we implemented a full control loop in LabVIEW with a nice user interface as shown in Figure 4-7. From this controller, we could monitor the position and the reference position of the glass, as well as temperatures read from the thermocouples. The gain of this controller could be automatically adjusted as temperature reaches to a certain temperature ($400°C$). We could also monitor the bearing pressure and flow-rate of the nitrogen.

With the improved controller, the stabilization time of the system could be brought down from $10\,mins$ to within $30\,s$.

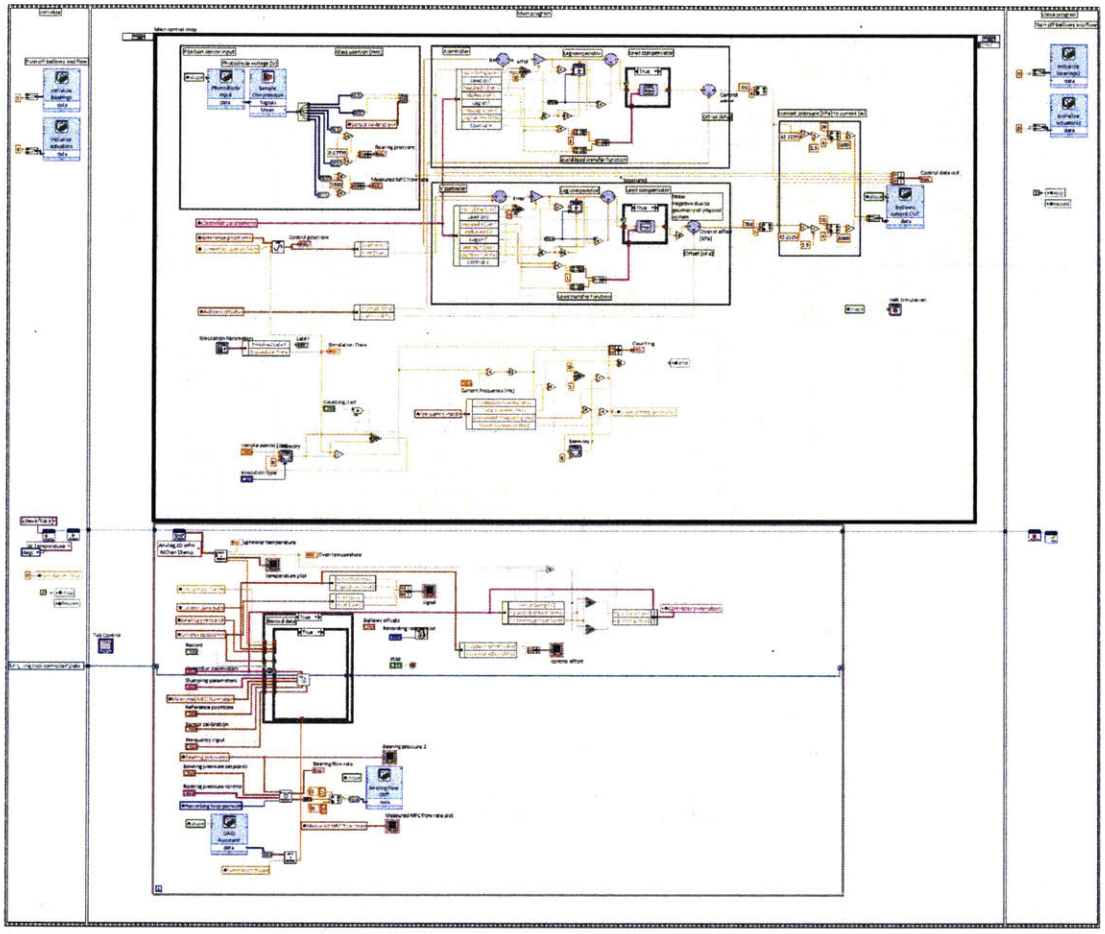

(a) Data-flow

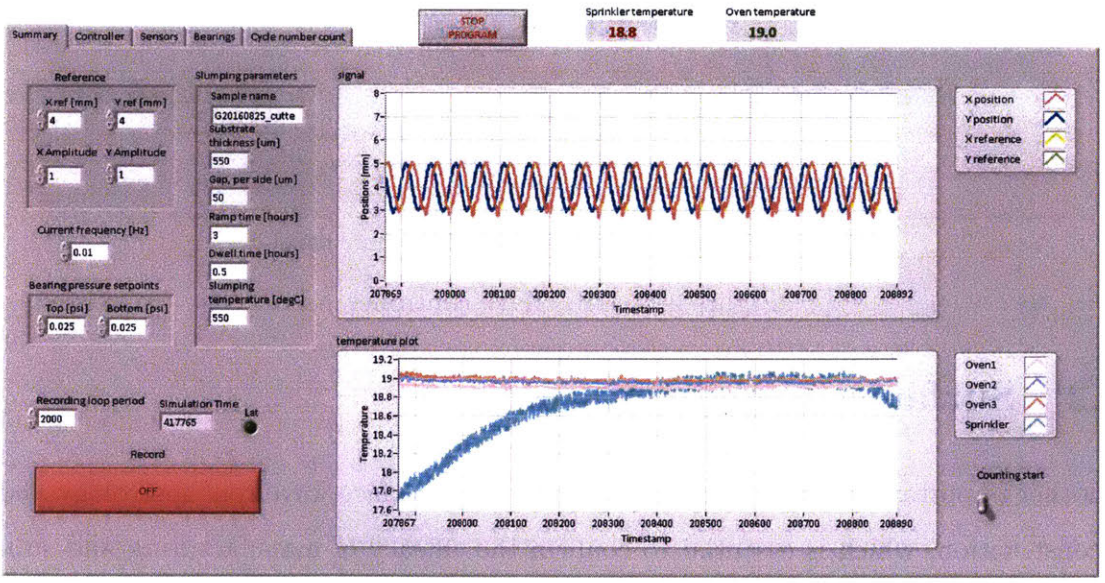

(b) User interface position and temperature monitor panel

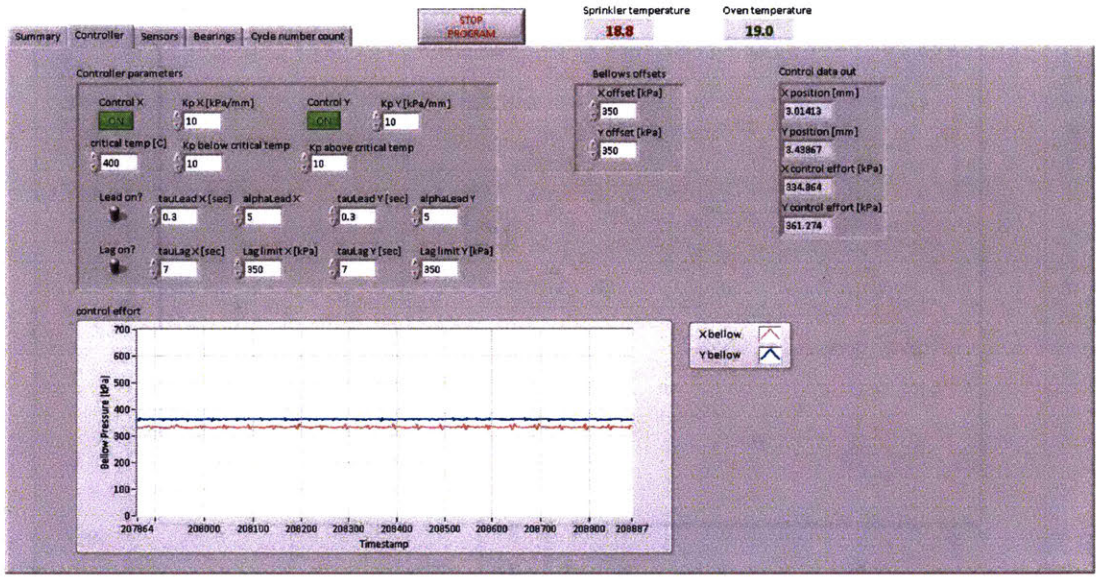

(c) User interface controller panel

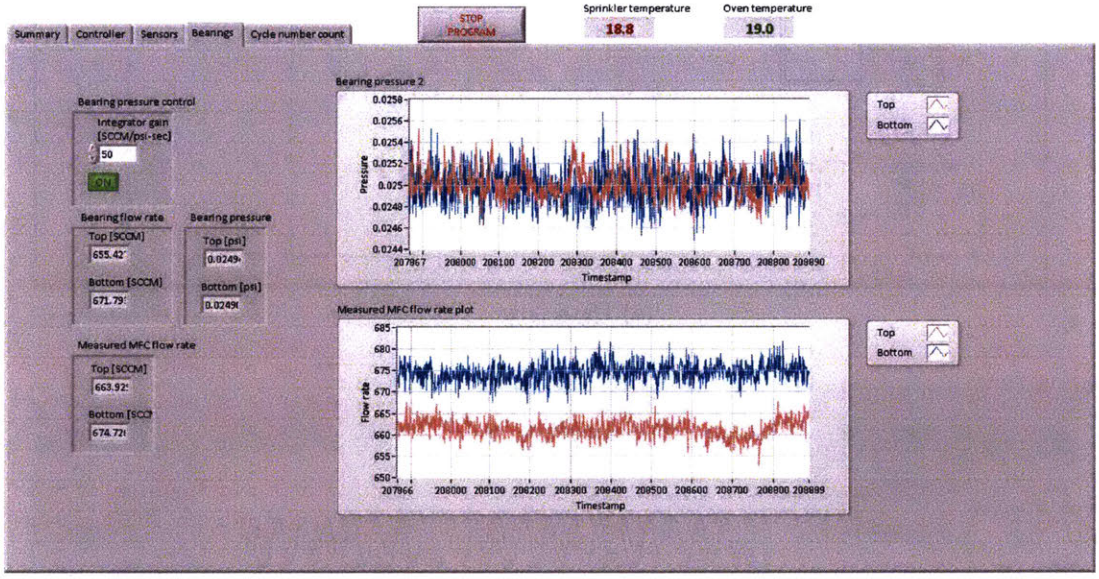

(d) User interface bearing pressure and flow rate panel

Figure 4-7: LabVIEW controller

4.2 Surface reconstruction

Another important aspect of the experiments is the surface wavefront metrology and reconstruction, which is essential to confirm the efficacy of manufacturing and substrate flattening processes. There are multiple solutions that could meet our demands for metrology of thin glass optics. In our lab, we have set up a deep-ultraviolet (deep-

UV) Shack-Hartmann surface metrology tool.

4.2.1 Shack-Hartmann wavefront sensing metrology

The Shack-Hartmann technology was developed by Platt and Shack as an improvement to the Hartmann metrology technology [20]. Instead of relying on light interference, Shack-Hartmann sensors measure position of focused spots from the far field to infer corresponding local near-field wavefront gradients.

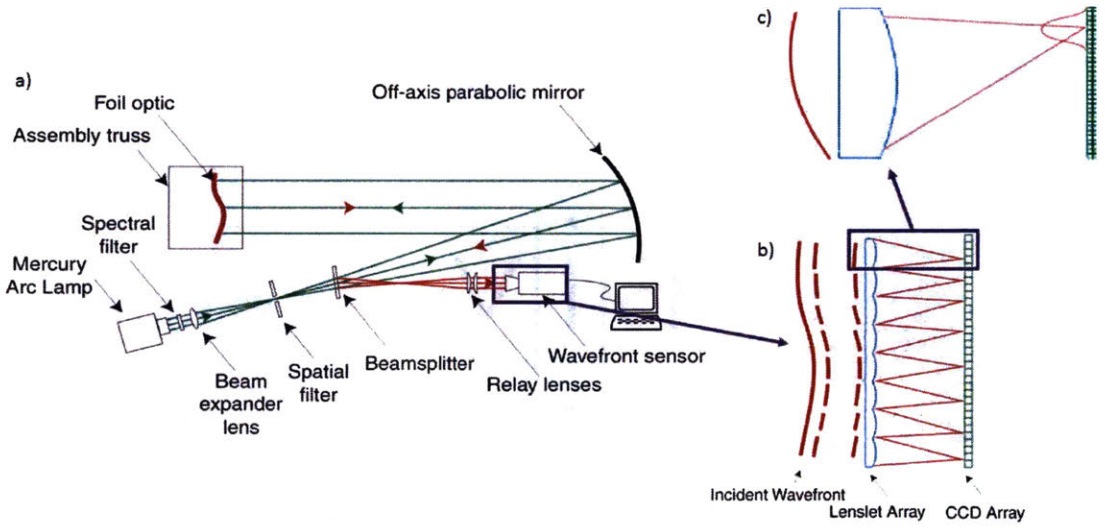

Figure 4-8: Shack-Hartmann wavefront sensing metrology tool concept. (a) The optical design for the deep-UV Shack-Hartmann metrology tool. (b) Lens array dissects the incoming wavefront. (c) Each lenslet focuses its portion of wavefront to a focal spot.

Figure 4-8 shows the Shack-Hartmann tool concept. [9] The system works is as follows:

(a) Collimated illumination passing through a spectral filter is focused by a beam expander lens, and then spatially filtered and propagated as an expanding spherical wave. An off-axis paraboloid then collimates this spherical wave, which limits the largest size of the object under measurement. The collimated light reflecting from the test optic, the paraboloid again, the beamsplitter, is then re-collimated by the relay lenses.

b) Lights reflected from the foil optics surface carrying information about the surface wavefront enters the wavefront sensor, where an array of lenslets is placed at the system image plane. Each lenslet in this array dissects one portion of the incoming wavefront onto the charge coupled device (CCD) detector array.

c) The average wavefront tilt across each lenslet aperture causes a shift of the corresponding focal spot. Comparing the distorted spot pattern from an aberrated wavefront to the regular spot pattern, we are able to generate a map of the wavefront slopes, from which the original optics surface wavefront could be reconstructed.

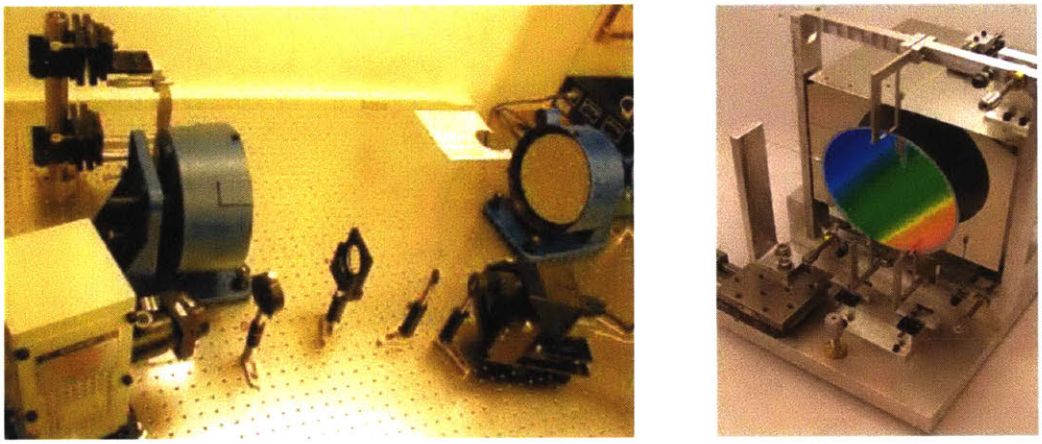

Figure 4-9: Shack-Hartmann metrology system hardware in a class 1000 cleanroom environment at the MIT SNL. Left: The optical instruments and light path. Right: Assembly truss mounting a sample.

Figure 4-8 shows the Shack-Hartmann tool concept. In our lab, we use deep-UV wavelengths as the light source since glass is virtually opaque to wavelengths below $260\,nm$, thus we will be able to reflect the wavefront from only one surface of the optics. This system has $350\,\mu rad\,(\approx 72\,arcsec)$ angular dynamic range and $0.5\,\mu rad\,(\approx 0.1\,arcsec)$ angular sensitivity. The surface map could cover over a $100\,mm$ diameter and is accurate to $17\,nm$ RMS and repeatable to $5\,nm$ RMS.

Figure 4-10 shows the raw data collected on the CCD array in the wavefront sensor.

After obtaining the wavefront data, we are able to reconstruct the surface profile using at least two different approaches: polynomial fitting and direct integration.

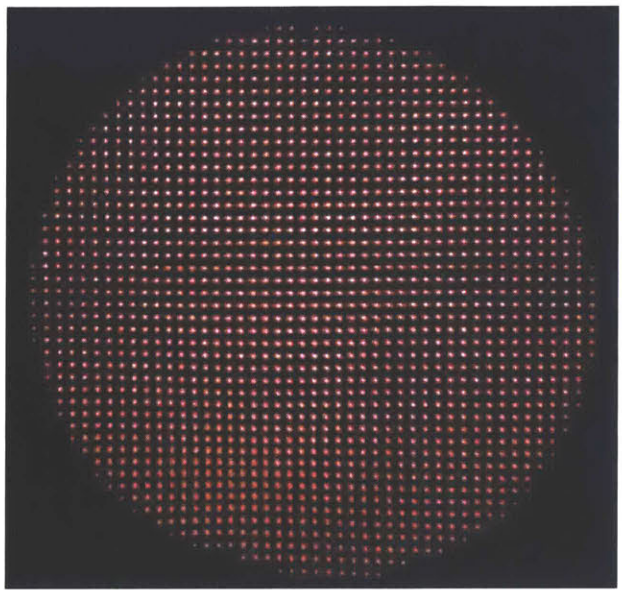

Figure 4-10: Raw data collected on the CCD array in the wavefront sensor of the Shack-Hartmann tool.

4.2.2 Surface reconstruction with polynomials

One way of describing wavefront aberrations are Zernike circle polynomials. Introduced by the Dutch scientist Fritz Zernike (Nobel prize laureate in physics for inventing phase-contrast microscope) in 1934, they can describe mathematically the 3-D wavefront deviation from a unit circle. Each polynomial describes one specific form of surface deviation, while many terms combined could describe many more complex surface topologies, which could be fit to specific forms of wavefront deviations.

These polynomials are orthogonal to each other on the unit circle in a continuous fashion. They are defined by two variables - φ the azimuthal angle, and ρ the radial distance ($0 \leq \rho \leq 1$), and they have even and odd polynomials:

$$Z_n^m(\rho, \varphi) = R_n^m(\rho)\, \cos(m\, \varphi) \tag{4.3}$$

$$Z_n^{-m}(\rho, \varphi) = R_n^m(\rho)\, \sin(m\, \varphi), \tag{4.4}$$

where m and n are non-negative integers with $n \geq m$, and $|Z_n^m(\rho, \varphi)| \leq 1$.

The radial polynomials R_n^m are defined as

$$R_n^m(\rho) = \sum_{k=0}^{\frac{n-m}{2}} \frac{(-1)^k\,(n-k)!}{k!\left(\frac{n+m}{2}-k\right)!\left(\frac{n-m}{2}-k\right)!}\,\rho^{n-2\,k} \tag{4.5}$$

for $n - m$ even, and 0 for $n - m$ odd.

Figure 4-11 shows the Zernike polynomials up to the 6^{th} order. The higher rows contribute to lower order aberrations, while the lower rows represent higher order aberrations.

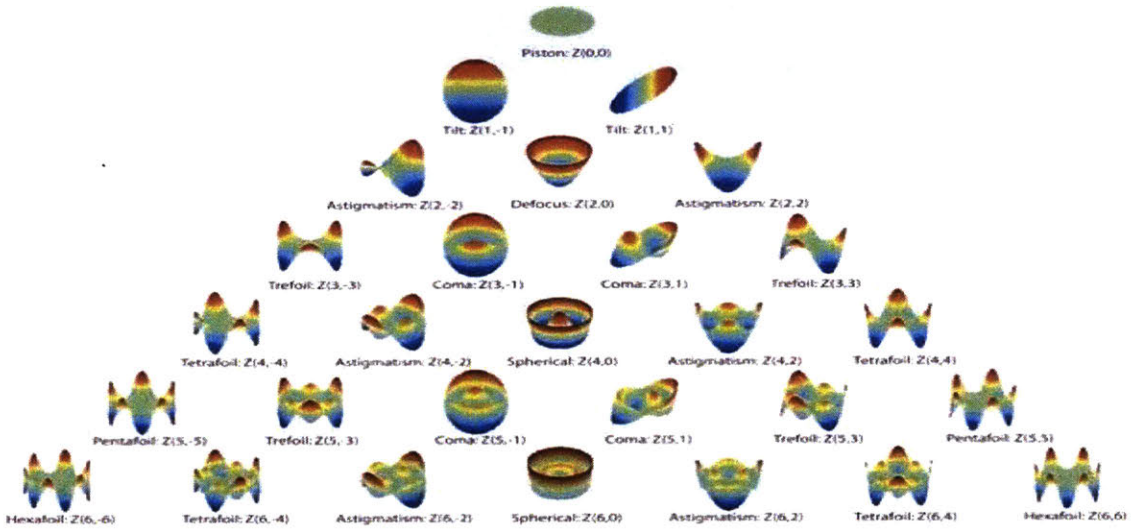

Figure 4-11: Zernike polynomials up to the 6^{th} order.[7]

In principle, by including sufficient number of terms, any wavefront deformation can be described to a desired degree of accuracy. However, if high n are involved, the unequal distribution of nodal lines over the circle will introduce ringing effects near the perimeter where $\rho \approx 1$. This is very undesirable in usage of measured data, since we won't know if the ringing effects are caused by the experiments or brought in by polynomial fitting. Another disadvantage for the Zernike polynomials is they are good for circular wafers but not so ideal for rectangular disks. The adaptivity of polynomials fitting method is also relatively low.

4.2.3 Surface reconstruction through direct integration

To overcome the drawbacks of polynomial fitting, another method of direct integration was introduced in our analysis. The idea is to apply a line integral with the gradient information between neighbouring grid points from Shack-Hartmann measurements to obtain wavefront differences at these grid points. The theoretical basis of line integration is set by Green's theorem.

In mathematics, Green's theorem gives the relationship between a line integral around a simple closed curve $\partial\Omega$ and a double integral over a plane region Ω bounded by the curve $\partial\Omega$. The curve should be positively oriented, piecewise smooth, and simple closed in plane. The theorem states that if P and Q are functions of (x, y) defined on an open region containing Ω and they have continuous partial derivatives, then:

$$\oint_{\partial\Omega} P\,dx + Q\,dy \;=\; \iint_{\Omega} \left(\frac{\partial Q}{\partial x} - \frac{\partial P}{\partial y}\right) dx\,dy \tag{4.6}$$

Specifically, in our case

$$P = \frac{\partial \phi}{\partial x},\; Q = \frac{\partial \phi}{\partial y},$$

where ϕ is the wavefront. Then the above equation becomes:

$$\oint_{\partial\Omega} \left(\frac{\partial \phi}{\partial x}\,dx + \frac{\partial \phi}{\partial y}\,dy\right) \;=\; \iint_{\Omega} \left(\frac{\partial}{\partial x}\frac{\partial \phi}{\partial y} - \frac{\partial}{\partial y}\frac{\partial \phi}{\partial x}\right) dx\,dy \tag{4.7}$$

If the wavefront is smooth enough and continuous differentiable to the second order, i.e. $\phi \in C^{(2)}$, then

$$\frac{\partial}{\partial x}\frac{\partial \phi}{\partial y} = \frac{\partial}{\partial y}\frac{\partial \phi}{\partial x}$$

, thus

$$\oint_{\partial\Omega} \left(\frac{\partial \phi}{\partial x}\,dx + \frac{\partial \phi}{\partial y}\,dy\right) \;=\; 0 \tag{4.8}$$

Thus we could choose any two path L_1, L_2 between two points A and B, such that $\partial\Omega = L_1 - L_2$, then they should have the same line integral:

$$\int_{L_1} \left(\frac{\partial \phi}{\partial x}\,dx + \frac{\partial \phi}{\partial y}\,dy\right) \;=\; \int_{L_2} \left(\frac{\partial \phi}{\partial x}\,dx + \frac{\partial \phi}{\partial y}\,dy\right) \tag{4.9}$$

This is shown in Figure 4-12. Using this conclusion, we could choose any path to

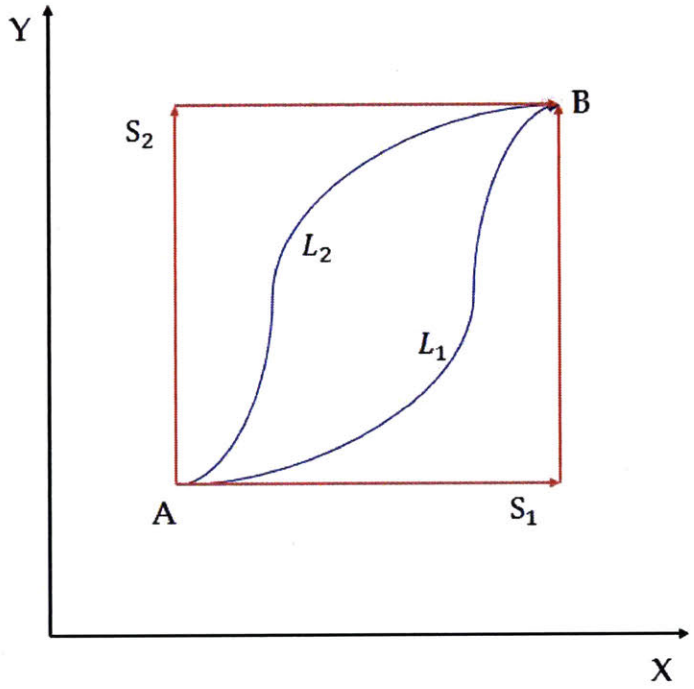

Figure 4-12: Line integration from point A to B.

integrate the wavefront between two points and they should generate the same value. From the Shack-Hartmann we could get the X and Y gradient components of the grid points, so we choose to integrate along path S_1 and path S_2 separately and take the average value of them as the reconstructed wavefront.

The advantage of direct line integration is its wide applicability — it could be used on any geometry and doesn't require a pre-defined set of polynomials to fit to. It could also capture some surface aberrant without introducing ringing effects on the rims. However, the disadvantage is its reconstruction accuracy. In the integration we are essentially assuming a linear gradient between the grid points, while the physical wavefront is certainly not linear.

4.2.4 Integrate both methods to a MATLAB based user interface

We built a Wafer Analysis GUI with MATLAB capable of processing the raw data from Shack-Hartmann with either polynomial fitting or direct integration method. The optics surface height and surface slope are calculated and plotted in both 2-D and 3-D views. Figure 4-12 shows this interface analyzing our slumped sample G20160603.

4.3 Slumping tests with improved slumping tools

Now that we have a stable system, we could go ahead to perform a series of experiments with our tools. The goals of these experiments are:

1. To explore the influence of different parameters, including pressure, slumping temperature, and slumping time, and try to come up with a combination of parameters that could produce the best slumping results which meet our requirements;

2. To establish repeatability of the slumping tools, i.e., to confirm that different substrates having undergone the same slumping procedure could have the same surface profile and slopes.

From the discussion about annealing glass in the previous chapter, we see that slumping temperature and slumping time are closely related. Since our system may become fragile as the temperature becomes higher, we chose to investigate the effects of slumping time first.

4.3.1 Short slumping time

With the improved system, we successfully performed over 60 short slumping tests with rapid sample changeover in just six weeks. We used Schott D263 glass substrates of $100\,mm$ diameter and $550\,\mu m$ thickness.

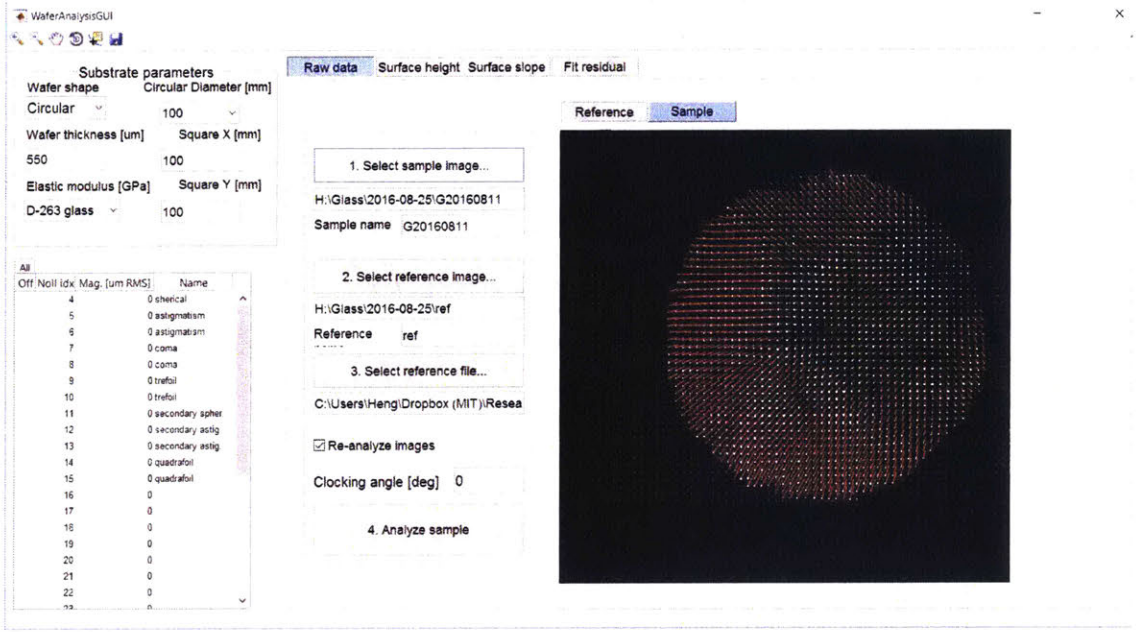

(a) Raw data

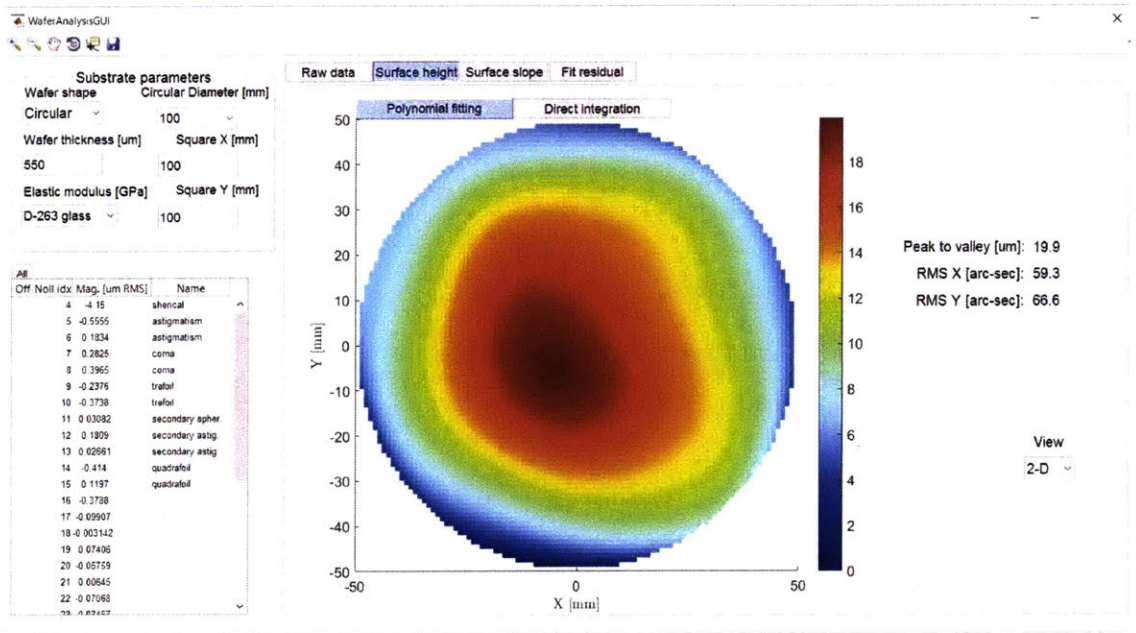

(b) Surface height through Zernike polynomial fitting

Figure 4-13 shows that the original wafer has large surface waviness with peak-to-valley[1] typically $60-90\,\mu m$ and average slope error of $\geq 200\,arcsec$.

[1]Peak-to-valley or P-V describes the surface flatness of the optics. It measures the difference between the "highest" and "lowest" parts on the surface of the optic, where "top" and "bottom" are defined as the local difference between the actual optic and the ideal one. It is a maximum measurement, and does not indicate how many peaks and valley there are on the whole surface.

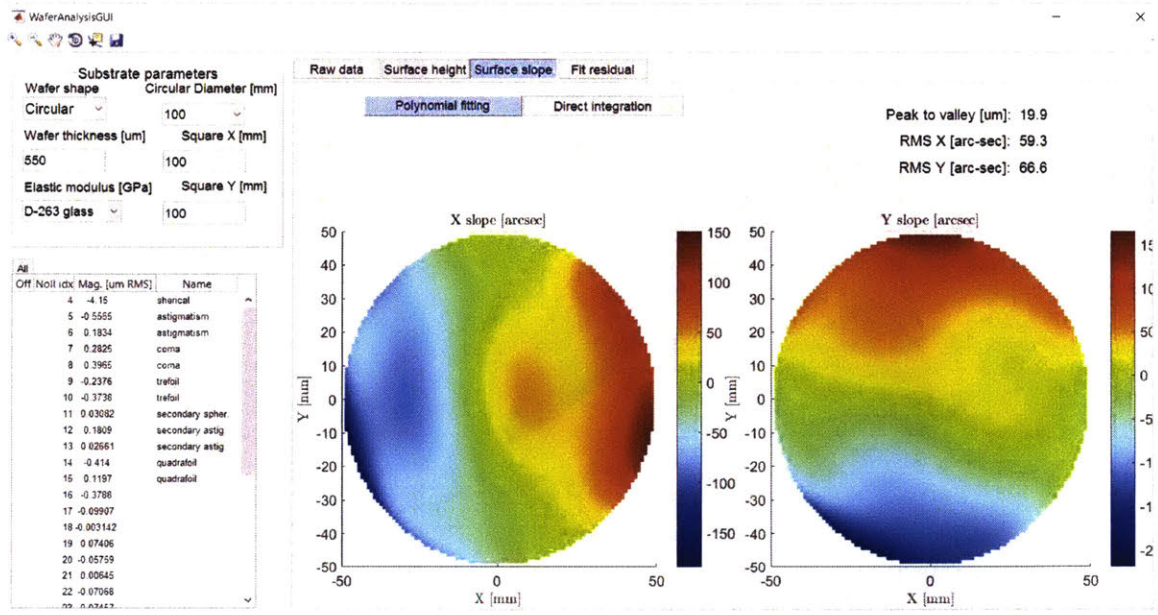

(c) Surface slope through Zernike polynomial fitting

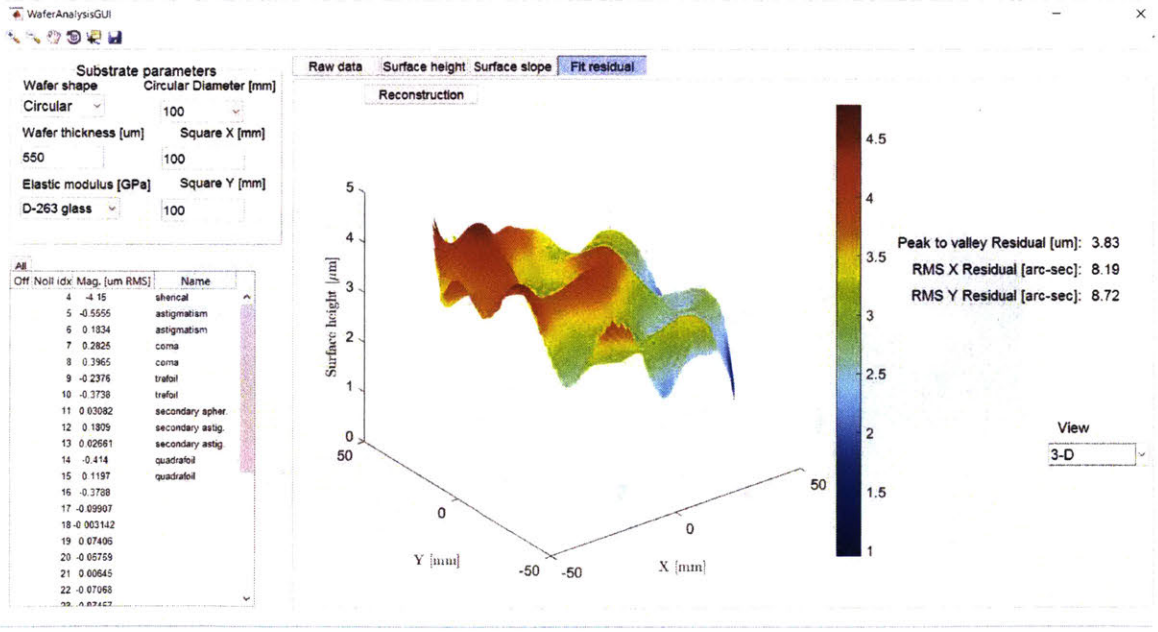

(d) Fitting errors between two methods

Figure 4-12: MATLAB based wafer analysis interface analyzing sample G20160811

To start with, we performed a series of short slumping experiments with short dwell time ($\leq 1\,h$) and observed the change of the peak-to-valley of the slumped

Here we use it only as an indicator but not an absolute criterion of the quality of surface flatness.

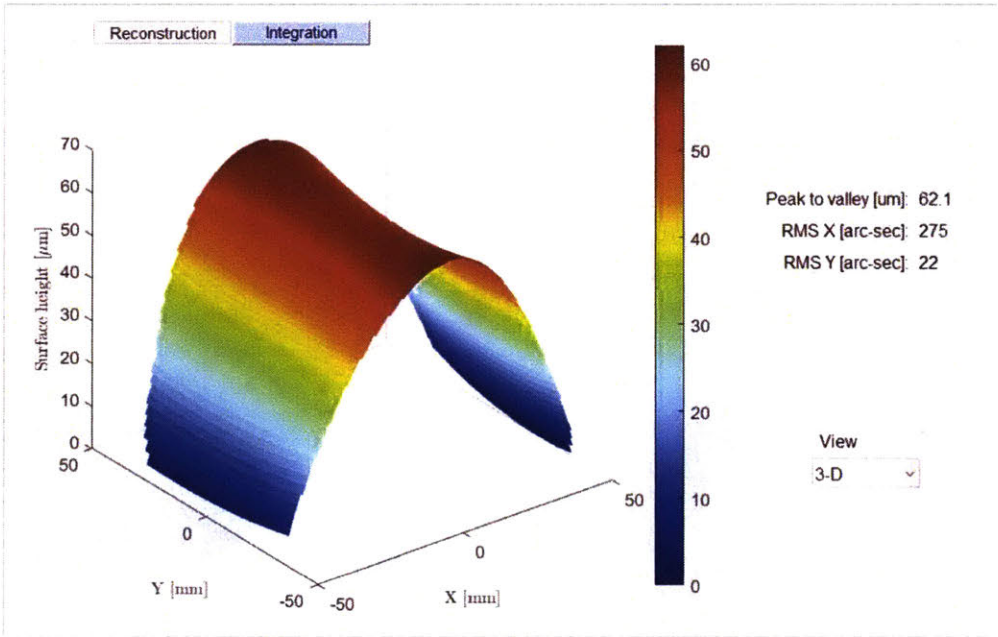

(a) Surface height

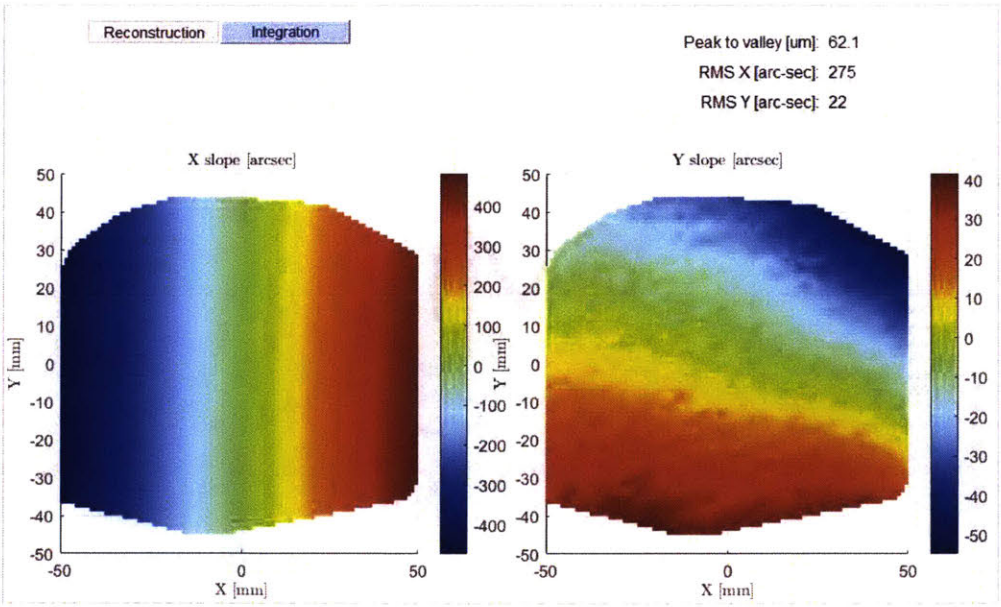

(b) Surface slope

Figure 4-13: Reconstructed surface wavefront of a pre-slumped substrate. A huge bow shape on the long spatial frequency range presents along one direction of the pre-slumped substrate.

glass. The results are shown in Figure 4-14.

In Figure 4-14 the left graph shows the reconstructed surface peak-to-valley of

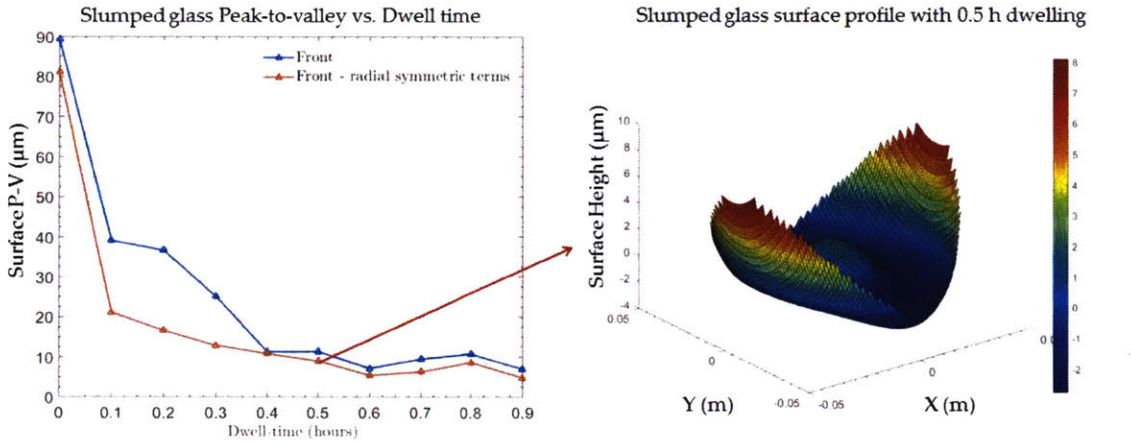

Figure 4-14: Short dwell experiments. Left: reconstructed surface P-V of slumped samples after a series of dwell time $0.1 \sim 0.9\,h$. Right: reconstructed surface profile after $0.5\,h$ dwell time.

slumped samples after a series of dwell times $0.1-0.9\,h$. Here I used Zernike polynomial fitting for all substrates, and both lines represent the front surface of the substrates [2]. The blue line shows all the terms from the Zernike polynomials, while the red line substrates the radially symmetric terms in the Zernike polynomials. Each point in this figure represents a new piece of glass. We could observe a constant P-V decrease with increasing slumping time, especially in the first $0.5\,h$; and the rate of this decrease slows down after $0.5\,h$.

The right graph shows the reconstructed surface profile after $0.5\,h$ of dwelling. Though the P-V has been largely decreased there is still strong astigmatism that has not been fully removed from the pre-slumped substrate, which indicates insufficient dwell time.

Having noticed the constant decrease of P-V with increasing slumping time, we were interested if this trend would keep decreasing as we slump longer. So we ask ourselves, is there an "equilibrium point" or "steady state" that we could reach? To answer this question, we had to slump longer.

[2]We define the "front" as the side of the glass facing top to avoid unnecessary confusions in the measurement.

4.3.2 Long slumping time

Then we carried out some long dwell time slumping experiments to find out if the assumed steady shape could be reached.

Figure 4-15 shows two slumping results after $16\,h$ of dwelling. The two surface profile have similar P-V of $\sim 15\,\mu m$ and similar "sombrero" shape, a Mexican hat, with a dome in the center and slight curls at the rims.

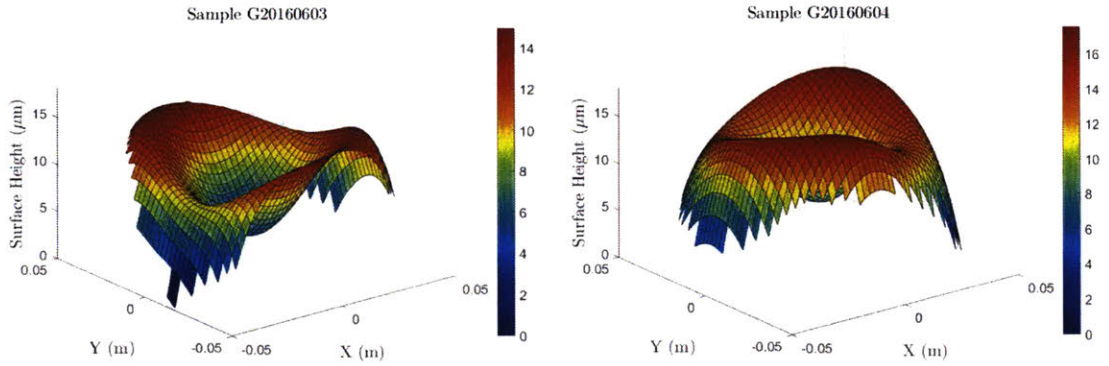

(a) (b)

Figure 4-15: Two experiments of long dwell time $16\,h$. Similar surface profile with P-V of $15\,\mu m$.

It's interesting that though we've increased the dwell time, the P-V of the slumped glass became larger again, and the surface profile looks quite different from that of the short slumping experiments.

Then we slumped a few substrates with even longer dwelling stage. Figure 4-16 shows two slumping results after $100\,h$ of dwelling. The two surface profile have similar P-V of $\sim 20\,\mu m$ and similar "water fountain" shape, with a dome in the center and obvious curls at the rims.

This raises a huge question: Why can't we reach a repeatable steady shape after long slumping time? Is there an equilibrium point at all? We couldn't find any explanation for what have been observed, if a final steady state exists as proposed. Obviously, we don't understand the mechanism of the slumping well enough just from our experiences with experiments. So I decided to step back and conduct some

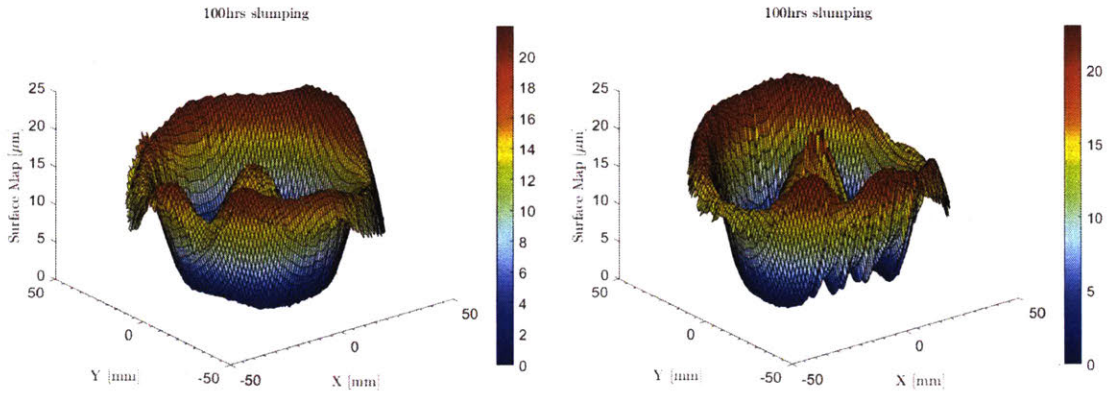

(a) (b)

Figure 4-16: Two experiments of long dwell time $100\,h$: Similar surface profile with P-V of $20\,\mu m$.

modeling and simulation to understand the cause of the large P-V and the mechanism of the interaction between the glass and air flow.

4.4 Discussion of the results

Before moving on to the discussion about simulations, I would like to state that we have also done a lot of tests tuning other parameters.

4.4.1 Influence of temperature

As said before, the temperature and slumping time are closely related. Despite our reluctance of going to higher temperature, we did perform a few experiments at $575°C$ and $600°C$. The main results were approximately as predicted, that the time scale of dwelling stage in general became a few times faster.

4.4.2 Influence of nitrogen pressure

All previous results were for pressure equal to $0.025\,psi$ ($\approx 172\,Pa$). Here I present some results for higher nitrogen pressure $0.08\,psi$ ($\approx 552\,Pa$). Figure 4-17 shows 5

different substrates were slumped at $1\,h$, $2\,h$, $4\,h$, $8\,h$, $16\,h$ and both front and back surface wavefront were measured. The trend was very similar to those of $0.025\,psi$.

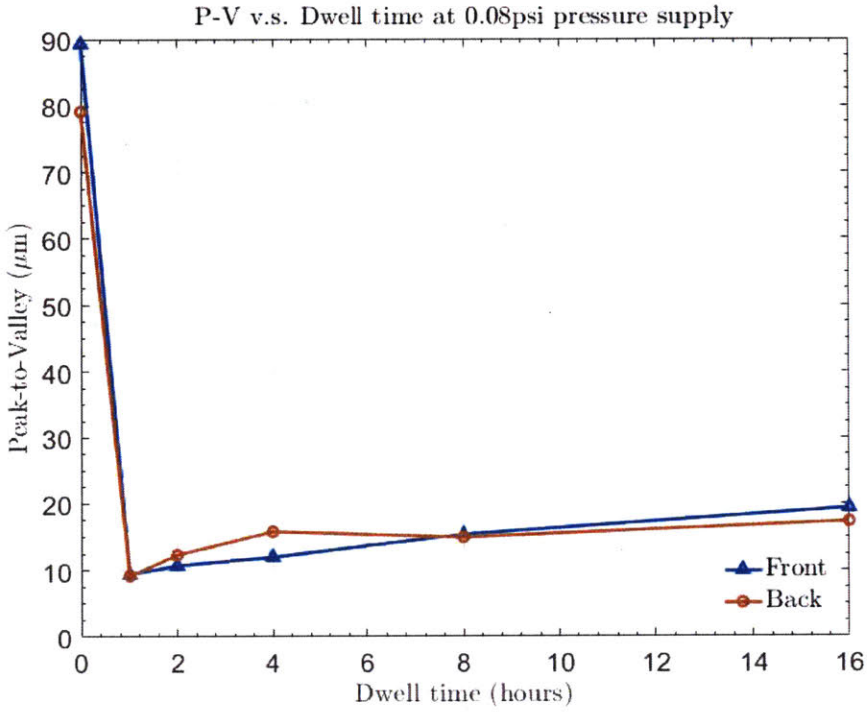

Figure 4-17: Surface P-V of 5 samples slumped at $1\,h$, $2\,h$, $4\,h$, $8\,h$, $16\,h$ with $P = 0.08\,psi$.

Though we had believed that higher pressure would reduce the surface waviness, however, the experimental results didn't show much support for this, at least not to an extent worth our notice of.

4.4.3 Influence of bearing-glass air film thickness

All previous experiments were conducted with an average air film thickness of $50\,\mu m$ on both sides of the glass. We also had the belief that the surface flatness would be improved with smaller air film thickness.

Figure 4-18 shows a comparison of slumped wafer surface P-V at 5 dwell times $0.5\,h$, $0.6\,h$, $0.7\,h$, $0.8\,h$, $0.9\,h$ between $35\,\mu m$ and $50\,\mu m$ average air film thickness. Though there were only a few samples, but we did notice that a smaller average

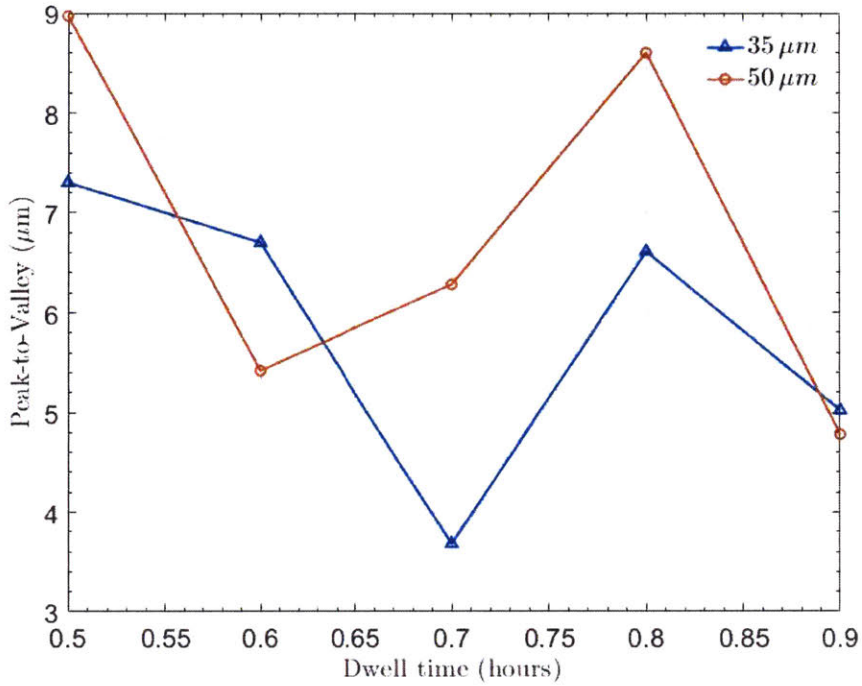

Figure 4-18: Surface P-V vs. dwell time for 35 μm and 50 μm average air film thickness

air film thickness seems to generate smaller glass surface P-V, which corresponds to smaller surface variation and better surface flatness.

4.4.4 Influence of gravity

Another very important factor is the gravity, which I believe is the main reason for the major dome shape we obtained from the experiments. After the glass reaches the dwell temperature and softens, the gravity force would tend to drag the glass towards the bottom bearing, and caused the central lob in the glass. If there were no gravity, this center lob might be smaller and lower in size.

I studied the effects of gravity later in the simulations.

Chapter 5

Numerical modeling and finite element analysis

The motivations for conducting numerical analysis are:

1. To better explain the experimental results, specifically why there seems to be no equilibrium or steady state for air-bearing slumping;

2. To further understand the underlying mechanism of the slumping process, especially how the glass moves and deforms, as well as how the air flows during air-bearing slumping.

5.1 Modeling air pressure distribution

5.1.1 Air pressure distribution of a square glass and a square bearing

One simple analysis has been done by one past graduate student [1] to estimate pressure distribution of air flow between a square glass and square bearing, assuming both the shape and position of the glass doesn't change during this process. The model is shown in Figure 5-1.

The assumptions and governing equations are listed as follows:

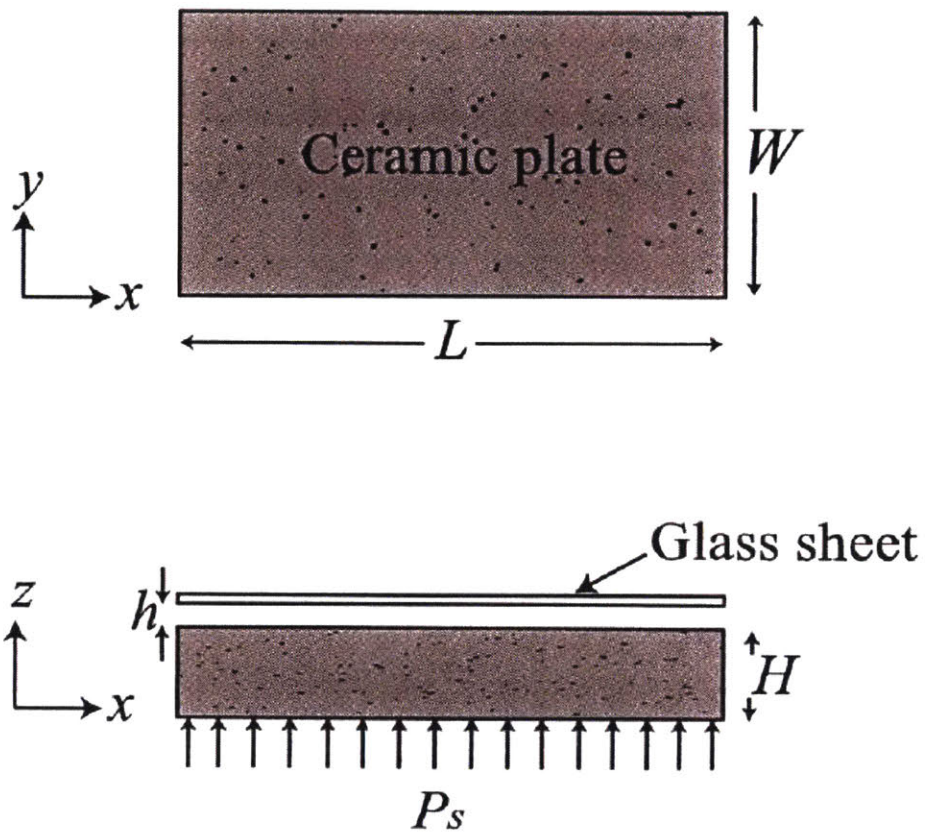

Figure 5-1: Geometry of the model for the air flow analysis with a porous ceramic plate and position-fixed glass.

1. The flow in the porous bearing is at creeping velocities, thus follows Darcy's law with k being permeability of the bearing:

$$\mathbf{U}' = -\frac{k}{\mu}\nabla p' \tag{5.1}$$

Continuity equation:

$$\frac{\partial U'_x}{\partial x} + \frac{\partial U'_y}{\partial y} + \frac{\partial U'_z}{\partial z} = 0 \tag{5.2}$$

where $\mathbf{U}'$, μ and p' are the velocity, viscosity and pressure of the air flow in the porous material.

2. Air flow in the gap between glass and bearing follows Navier-Stokes equation:

$$\rho\left(\frac{\partial \mathbf{U}}{\partial t} + \mathbf{U}\cdot\nabla\mathbf{U}\right) = -\nabla p + \mu\nabla^2\mathbf{U} + \mathbf{f} \tag{5.3}$$

which could be further reduced to:

$$\frac{\partial^2 \mathbf{U}}{\partial z^2} = \frac{1}{\mu}\nabla p \tag{5.4}$$

where $\mathbf{U}$, μ and p are the velocity, viscosity and pressure of the air flow in the gap between the glass and bearing.

The boundary conditions for this equation are:

$$z = h:\ \mathbf{U} = 0; \tag{5.5}$$

$$z = 0:\ \mathbf{U} = \mathbf{U}',\ p = p'. \tag{5.6}$$

From part 2 we get:

$$\mathbf{U} = \frac{1}{2\mu}z(z-h)\nabla p - \frac{h-z}{h}\frac{k}{\mu}\nabla p' \tag{5.7}$$

or equivalently:

$$u = \frac{z-h}{\mu}\left(\frac{z}{2} + \frac{k}{h}\right)\frac{\partial p}{\partial x} \tag{5.8}$$

$$v = \frac{z-h}{\mu}\left(\frac{z}{2} + \frac{k}{h}\right)\frac{\partial p}{\partial y} \tag{5.9}$$

$$w = \frac{z-h}{\mu}\frac{k}{h}\frac{\partial p'}{\partial x}\bigg|_{z=H} \tag{5.10}$$

where u, v, w are the velocity components of $\mathbf{U}$.

Integrate the continuity equation with the solution in equation 5.8 we get

$$\frac{\partial^2 p}{\partial x^2} + \frac{\partial^2 p}{\partial y^2} = \frac{12k_z}{h(h^2+6k_z)}\frac{\partial p'}{\partial z}\bigg|_{z=H} \tag{5.11}$$

Since $k \sim 10^{-16}\, m^2$, $h^2 \sim 10^{-12}\, m^2$, so $k \ll h^2$, then the above equation becomes:

$$\frac{\partial^2 p}{\partial x^2} + \frac{\partial^2 p}{\partial y^2} = \frac{12 k_z}{h^3} \frac{\partial p'}{\partial z}\bigg|_{z=H} \tag{5.12}$$

According to the above solution, a finite difference scheme was used to calculate the pressure distribution of the pressure in a square bearing. Figure 5-2 shows three calculated pressure profiles for a $100\, mm \times 100\, mm \times 12.7\, mm$ porous bearing with different air gap thickness [1]. This figure shows that the smaller the gap, the more uniform and higher is the pressure distribution.

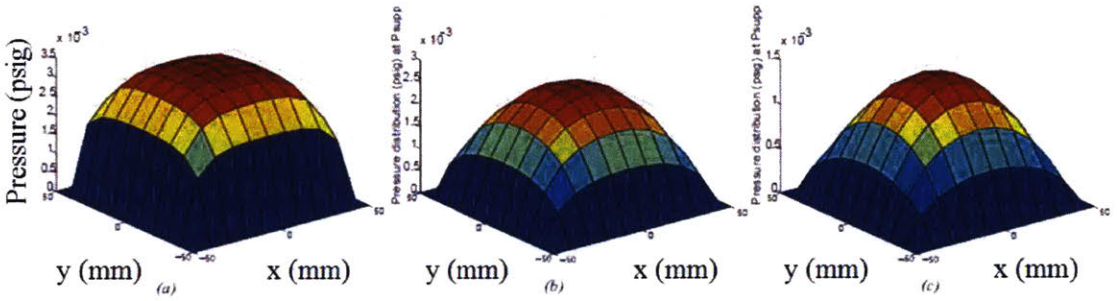

Figure 5-2: Air gap thickness from left to right: $5\,\mu m$, $10\,\mu m$, $15\,\mu m$. [1]

5.1.2 Air pressure distribution of a circular glass and a circular bearing

Next we consider modeling the circular case. Most of the derivations in the above section are the same, but now in the polar coordinates. This work was presented by P. Murti in 1974 [16] and the solution of the pressure distribution $p(r)$ in the air film is:

$$p(r)^2 = p_s^2 + \left(p_a^2 - p_s^2\right) \frac{I_0(\lambda r)}{\lambda R}, \qquad \lambda = \sqrt{\frac{12k}{Hh^3 + 6kH^2}}. \tag{5.13}$$

where

p_s - absolute supply pressure to the air bearing,

p_a - ambient pressure,

R - radius of the bearing and glass,

k - permeability of the porous air bearing,

h - thickness of the air gap,

H - thickness of the porous air bearing,

I_0 - the modified Bessel function of the first kind of order zero $I_n(z) = \frac{1}{2\pi i} \oint e^{\frac{z}{2}(t+\frac{1}{t}))} t^{-n-1} dt$.

The above solution could also be written as:

$$p(r)^2 - p_a^2 = \left(p_s^2 - p_a^2\right)\left(1 - \frac{I_0(\lambda r)}{\lambda R}\right) \tag{5.14}$$

Since both $p(r)$ and p_s are much smaller than p_a, thus

$$p(r)^2 - p_a^2 = (p(r) - p_a)(p(r) + p_a) \approx (p(r) - p_a)p_a, \tag{5.15}$$

$$p_s^2 - p_a^2 = (p_s - p_a)(p_s + p_a) \approx (p_s - p_a)p_a \tag{5.16}$$

The solution could be further rewritten as

$$p(r) = p_s\left(1 - \frac{I_0(\lambda r)}{\lambda R}\right), \tag{5.17}$$

This analysis provides us with a starting point for analyzing the air flow between the glass and bearing, however, it's oversimplified and doesn't consider any motion or deformation of the glass, which is the most crucial thing we care about during slumping. Obviously, we need to take into consideration the glass in the finite element analysis.

5.2 Fluid-structure interaction analysis

The way to consider both air flow and glass deformation together is through implementing fluid–structure interaction (FSI). FSI could solve the problem when fluid flow causes deformation of the structure, while this deformation, in turn, changes the boundary conditions of the fluid flow.

5.2.1 FSI to simulate glass deformation

In fluid-structure interaction analyses, fluid forces are applied onto the solid and the solid deformation changes the fluid domain. The computational domain is therefore divided into a fluid domain and a solid domain, where a fluid model and a solid model are defined respectively, and the interaction occurs along the interface of the two domains. Having the two models coupled, we can perform simulations and predictions of the actual physical phenomena.

To solve the coupling between the fluid and the structural models, the conditions of displacement compatibility and traction equilibrium along the structure-fluid interfaces must be satisfied:

Kinematic condition, or Displacement compatibility: $$\mathbf{d}_f = \mathbf{d}_s \quad (5.18)$$

Dynamic condition, or Traction equilibrium: $$\mathbf{n} \cdot \tau_\mathbf{f} = \mathbf{n} \cdot \tau_\mathbf{s} \quad (5.19)$$

where $\mathbf{d}_f$ and $\mathbf{d}_s$ are the fluid and solid displacements respectively, τ_f and τ_s are the fluid and solid stresses respectively, and $\mathbf{n}$ is the local normal direction of the fluid-solid interface.

Fluid–structure interaction problems are in general too complex to solve analytically, so they have to be analyzed by means of numerical simulation including both computational fluid mechanics and computational solid mechanics. Two main approaches for the simulation of fluid–structure interaction problems are:

- Monolithic approach (or direct FSI coupling): the equations governing the fluid and the structure are combined and treated in one system (with one stiffness matrix), linearized and solved simultaneously, with a single solver;
- Partitioned approach (or iterative FSI coupling): the equations governing the fluid and the structure are solved separately, with two distinct solvers, in succession, always using the latest information provided by the other part of the coupled system.

In our simulations, I used the first approach which requires less memory and therefore could be applied to deal with larger scale problems. The FSI simulation

could be incorporated with a finite element scheme in commercially available software. The software that I use is ADINA, founded and developed by Dr. K.J. Bathe, a professor at MIT School of Engineering.

5.2.2 Combined simulation for both glass motion and deformation

Another challenge we have in the simulation is to combine the glass motion and deformation together. This essentially requires a transient analyses, where typically a time integration scheme can be used. However, to solve this dynamics problem as a whole is too complicated. So I would have to consider the causes of glass motion and deformation separately.

As stated before, the glass deformation is rooted in its interaction with the air flow, and could be modeled with fluid-structure interaction. This is assuming no absolute displacement change of the glass. The cause for glass motion is essentially the force imbalance. All the forces exerted on the glass are: net pressure from the surrounding air and the gravity of the glass. If the net force exerted on the glass is non-zero, then the glass would have a total displacement towards the direction of the net force. This is assuming there is no deformation in the glass, such that the glass is moving as a rigid body pushed by the ambient air flow.

With the above notions, we could start thinking if it's possible to separate the simulation of glass shape (deformation through FSI) and glass position (motion through fluid mechanics of air). In this problem, the fluid field and the fluid-structure-interaction have different time scales: the disturbance in the fluid field could be responded immediately, yet the viscoelastic deformation in the glass would take a much longer time.

Thus I came up with a scheme to update glass position and shape separately and iteratively as shown in the following recipe:

iterative scheme

1. Assuming the glass is a rigid body, perform computational fluid mechanics in the air films to find the balance position of the glass:

   - Conduct CFD simulation, calculate total force on the glass

   $$F_{total} = \int_{\Omega} (p_{top} - p_{bottom}) dA \; + \; \rho g h A; \tag{5.20}$$

   where p_{top}, p_{bottom} are the pressure from the top and bottom glass-air interface, ρ, h, A are the density, thickness and surface area of the glass, and g is the gravitational constant.

   - If $F_{total} > 0$, there is a net force pointing downwards, then artificially move the glass position towards the bottom, and vice versa;
   - Repeat above two steps until the net force on the glass is close to zero within a threshold, then update the position of the glass.

2. Maintain the same glass position from step 1 and deform the glass using fluid-structure interaction:

   - Conduct FSI simulation for a certain length of time (controlled by the relaxation time of the viscoelasticity of glass, which I'm about to explain in future sections);
   - Find the deformation of the glass and update the shape of the glass.

3. Iteratively perform the above two steps, with enough iterations to approximate the actual physical time.

The advantage of this scheme is that it not only considers the macro force balance of the glass (step 1), but also leaves enough time for stress relaxation within the glass (in step 2). In the following sections, I'll show how this scheme works in detail.

5.3 2D axisymmetric elastic glass model

The purpose is to analyze the pressure distribution of air films and dynamic glass deformation together, as outlined in the above section. Nevertheless, this is still too complicated to model. Apart from the pressure and velocity distribution of the air films, and the motion and deformation of the glass, the mechanical and thermal properties for modeling glass have not been fully studied systematically. Thus no work could be done unless some assumptions are made.

To start with, I'll first carry out simulations for the 2D axisymmetric model. In this type of flow, the solution variables are the same on each radial cross-section plane in a cylindrical coordinate system. Solutions can therefore be defined in a domain on one radial plane.

5.3.1 Model set-up in ADINA

In this section, I make the following assumptions:

- The model for both bearings are axisymmetric about the axis, so only one radius of the physical objects need to be modeled, thus this 2D axisymmetric model enables a much smaller problem scale and much faster simulation;
- The center of the glass is pinned at the axis, such that the horizontal position of the glass is fixed while only vertical movement along the axis is allowed;
- No thermal process or temperature change is considered, which means we are only modeling the dwelling stage at constant temperature $500°C$.

The model set-up in ADINA is shown in Figure 5-3.

Given the above assumptions, we still need a model for the glass. In the coming sections, I'll discuss two different models for the glass. But before that, I need to show some credibility of this analysis in general, so I set the glass to be a rigid body and compare to the analytic solution first.

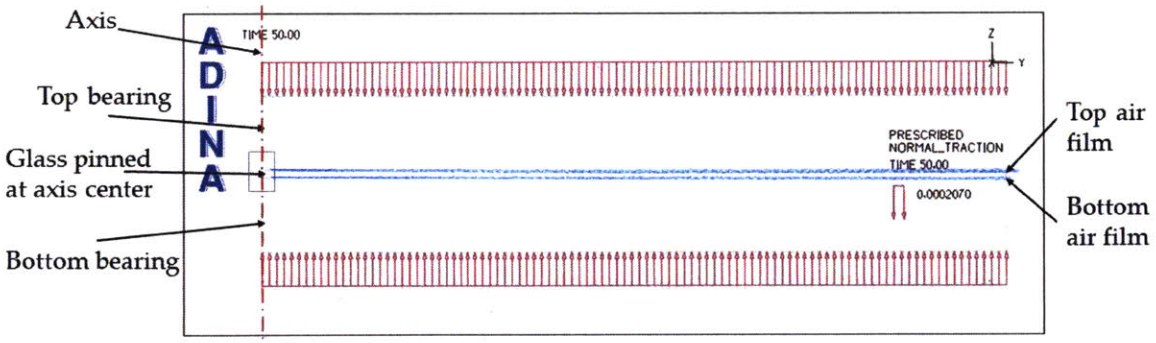

Figure 5-3: 2D axisymmetric model

5.3.2 Rigid glass model compared with the analytic solution

I first performed a simple finite element analysis assuming a rigid glass model, and compare the air pressure distribution from the simulation to the analytic solution in section 5.1.2. This is basically a computational fluid dynamics simulation.

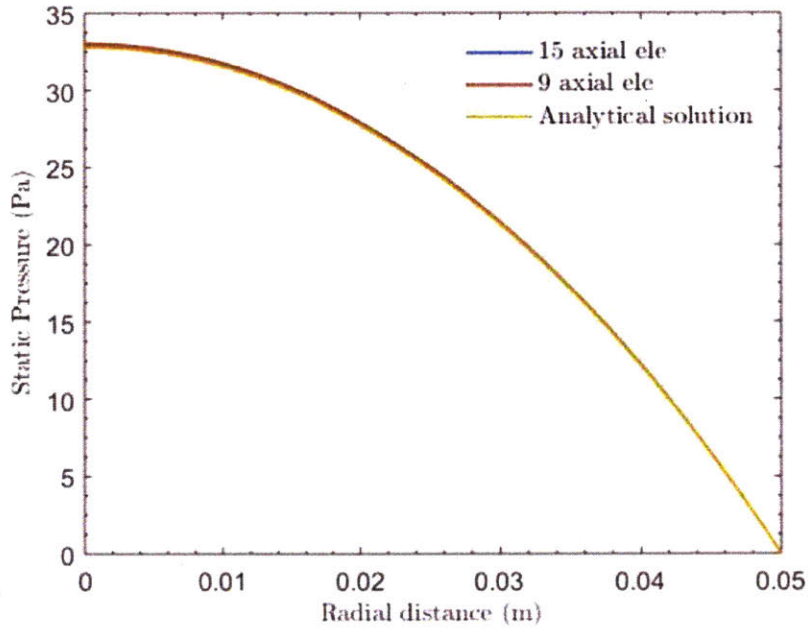

Figure 5-4: Pressure distribution in the air film: Comparison between the finite element analysis of rigid glass model and the analytic solution.

Figure 5-4 shows that even with very few elements along the radial direction,

the pressure distribution from the simulation result resembles that of the analytic solution.

5.3.3 Elastic glass model

Now I need to introduce a deformable model for the glass to perform the scheme outlined in 5.2.2. The simplest model for a deformable solid is a pure elastic model, where the material is only defined by Young's modulus, Poison ratio and density.

The material properties I used for this model were:

Glass: $E = 72.9\,GPa$, $\nu = 0.208$, $\rho = 2.51 \times 10^3\,kg/m^3$;

Air: $\mu = 3.623 \times 10^{-5}\,kg/(m \cdot s)$, $\rho = 0.4027\,kg/m^3$;

Bearing: $\kappa = 4 \times 10^{-13}\,m^2$.

The geometric properties I used for this model were:

Glass: radius $50\,mm$, thickness $550\,\mu m$;

Air film: total thickness (adding air films on both side of the glass) $100\,\mu m$;

Bearing: radius $72\,mm$, thickness (of each bearing) $6\,mm$.

Figure 5-5 shows how the shape and position of the glass is updated in each iteration. An arbitrary shape of the glass is input to the system, while the initial vertical position of the glass is at the center of the gap with $50\,\mu m$ of air film on both sides of the glass. Each line represent the glass after one iteration, and each iteration corresponds to certain physical time. In total 2000 iterations were performed and the glass after each iteration was plotted on the same figure shown here.

The two arrows label the initial input glass and the output glass after 2000 iterations (corresponding to about $5\,h$ of physical time). We could see that both the shape and central position of the glass change dramatically. The final P-V is $13\,\mu m$, quite on the same magnitude with the experiments.

5.3.4 Influence of simulation time

One question that needs to be answered from the experiments is if there is a final "equilibrium state" for the glass. So it's important for us to study the time evolution

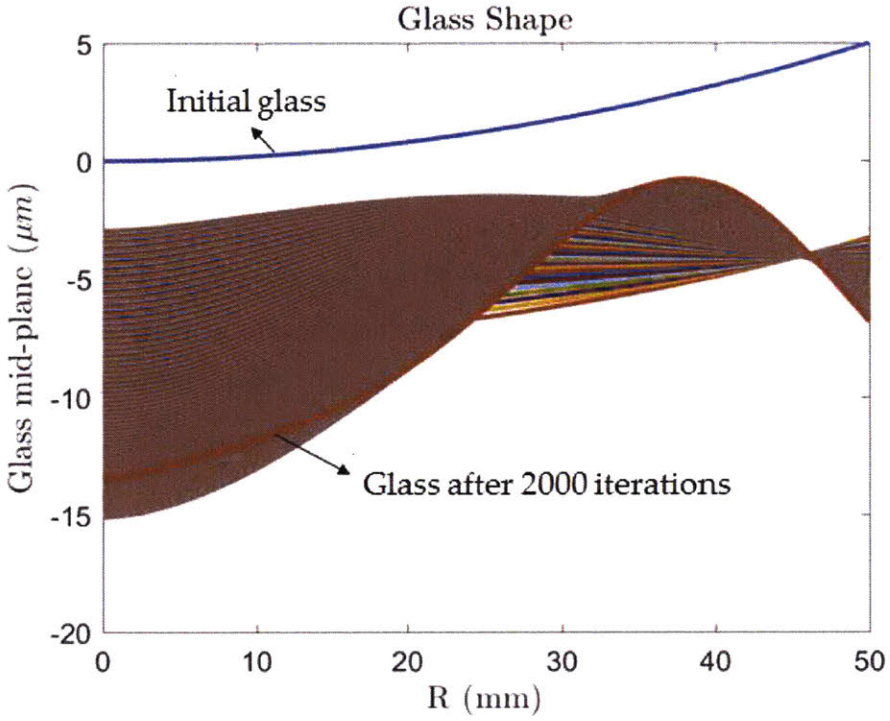

Figure 5-5: Iterative scheme updates the shape and position of the elastic glass through iterations. Blue line shows the initial input glass. Orange line shows the output glass after 2000 iterations.

of the glass from iteration to iteration.

Figure 5-6 shows the same simulation of Figure 5-5 extended to 5800 iterations. (a) With 3000 more iterations, the glass deformed even further. In fact, another smaller wave formed closer to the central axis. Though we haven't observed this in experiments, the results itself is quite interesting. This suggests that if I keep running the simulation, the glass will keep deforming; i.e. there is no convergence of the glass shape, or no "steady state". It also suggests that no matter what the initial shape of the glass is, after the same number of iterations the output glass shape should be very similar, i.e. we should control the slumping time to get repeatable results.

(b) and (c) show RMS[1] deformation and von Mises stress[2] of the glass between

[1]RMS, abbreviation for root mean square, is the square root of the arithmetic mean of the squares of the values.

[2]Von Mises stress, also known as the equivalent tensile stress, is directly related to the deviatoric strain energy and describes yielding of materials.

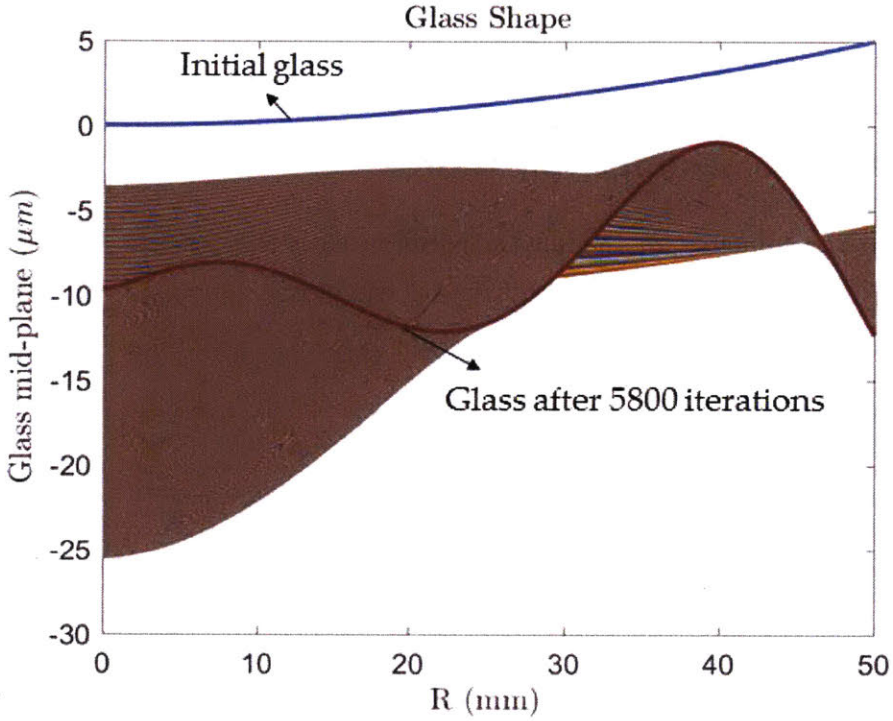

(a) Evolution of the glass through iterations. Blue line: input initial glass. Red line: output glass after 5800 iterations.

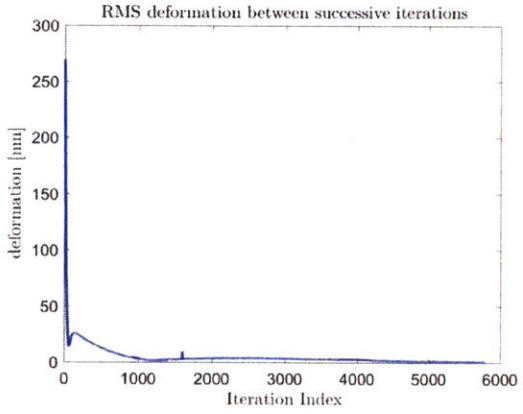

(b) RMS deformation of the glass between successive iterations.

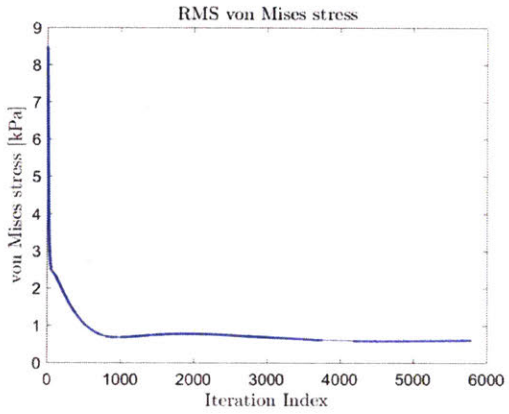

(c) RMS von Mises stress inside the glass between successive iteration.

Figure 5-6: Simulation results after 5800 iterations.

successive iterations. Both two values reduce significantly since the iteration stars, and gradually reach to a stable value. Though the glass keeps deforming, the RMS deformation and von Mises stress tends to maintain relatively constant. Note that in figure (b), despite the von Mises stress has dropped dramatically since the slumping

starts, it is nevertheless never zero. This means that in our simulation the glass is never completely stress-free, which is a contradiction to our assumption.

5.3.5 Influence of supply pressure

I also studied the influence of the supply pressure with this model. In Figure 5-7, four different supply pressures $p_s = 0.0015\,psi$, $0.0025\,psi$, $0.004\,psi$, $0.0055\,psi$ are used. All four cases have the same input initial glass, but after 2000 iterations the results are quite different.

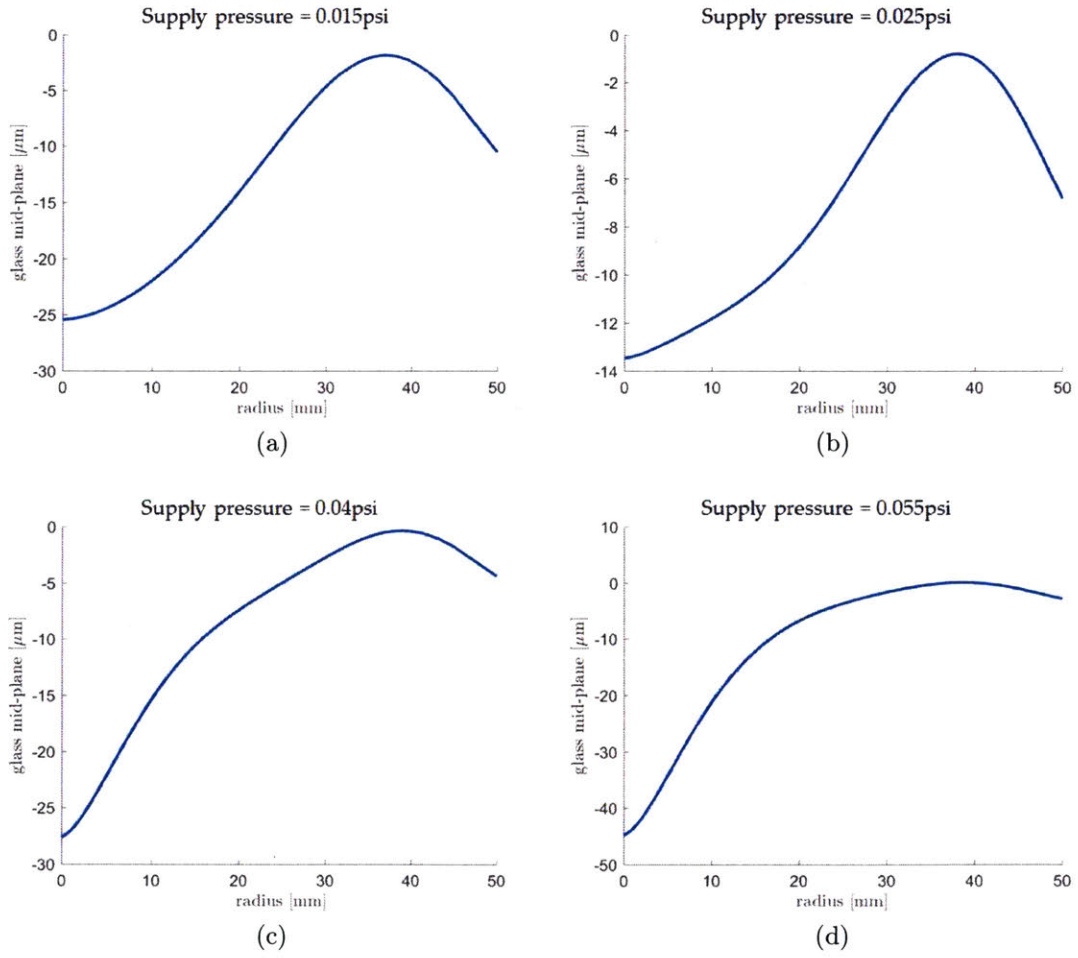

Figure 5-7: Output glass under different supply pressure with the same input initial glass after 2000 iterations.

The deformation becomes much greater as the pressure goes higher, which to

some extent contradicts our previous belief that higher pressure will generate flatter glass. Another thing to notice is that when the supply pressure reaches $0.055 psi$, the deformation of the glass has become so large ($40\,\mu m$) that it might take half the allowable space between two air-bearings (the total space is $100\,\mu m$).

By assuming the glass as an elastic material, we are essentially hoping that after each iteration defined by 5.2.2, the internal stress of the glass is relieved, such that the output of the last iteration which is also the input of the next iteration is in a stress-free state. This belief, however, is anything but true. So the model need to be improved by introducing viscosity into the glass.

5.4 2D axisymmetric viscoelastic glass model

5.4.1 Modeling glass viscoelasticity

Before we move on, we need a model for viscoelastic materials. Unlike elastic materials which can deform back to the original state very quickly once the stress is removed, viscous materials show resistance to shear flow and strain linearly with time under external stress. Glass above its strain point could be viewed as a viscoelastic material, that could exhibit both viscous and elastic characteristics when undergoing deformation. The strain is time-dependent, as a result of the diffusion of atoms or molecules inside an amorphous material.

Standard linear solid model and stress-strain relaxation

For viscoelastic materials, the elastic components can be modeled as springs, given by

$$\sigma = E\varepsilon, \tag{5.21}$$

where σ is the stress, E is the elastic modulus of the material, and ε is the strain that occurs under the given stress. The viscous components can be modeled as dashpots

for which the stress–strain rate relationship is given by

$$\sigma = \eta\dot{\varepsilon}, \tag{5.22}$$

where σ is the stress, η is the viscosity of the material, and $\dot{\varepsilon}$ is the time derivative of strain.

One model that combines both effects together is the standard linear solid model, shown in Figure 5-8. A viscous material is modeled as a spring and a dashpot in series

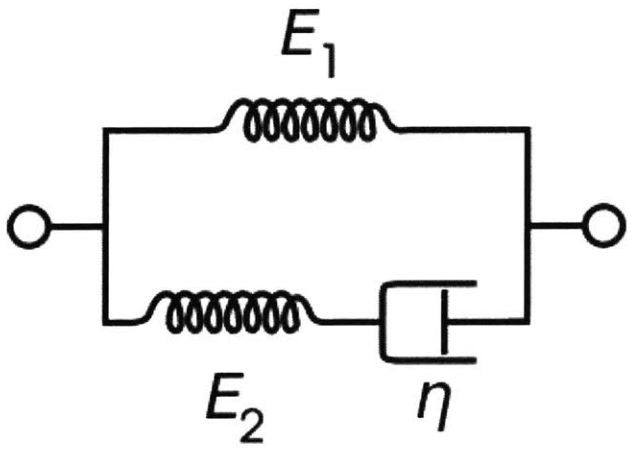

Figure 5-8: Standard linear solid model

with each other, both of which are in parallel with another spring. The governing constitutive relation is

$$\dot{\varepsilon} = \frac{1}{E_1 + E_2}\left(\dot{\sigma} + \frac{E_2}{\eta}\left(\sigma - E_1\varepsilon\right)\right) \tag{5.23}$$

Specifically, we are actually interested in the stress-relaxation behaviors of the glass at given strain as imposed by the bearing. For linear viscoelastic materials, the stress-strain relationship does not depend on strain history, thus is separable. The stress relaxation function of this model is:

$$E(t) = E_1 + E_2\, e^{-\frac{t}{\tau}}, \qquad \tau = \frac{\eta}{E_2}, \tag{5.24}$$

where τ is the relaxation time. From this relationship, we could define the "glassy" relaxation moduli which relates to the instant response, and "equilibrium" relaxation moduli which relates to the long-term response of the viscoelastic material:

$$E_g = E(0^+) = E_1 + E_2, \tag{5.25}$$

$$E_e = E(\infty) = E_1. \tag{5.26}$$

Furthermore, using shear modulus

$$G(t) = \frac{E(t)}{2(1+\nu)}$$

and bulk modulus

$$K(t) = \frac{E(t)}{3(1-2\nu)}$$

we could express the stress-strain relationship for the linear-viscoelastic material as

$$\sigma'_{ij} = 2G(t)\epsilon'_{ij}(0) + \int_0^t 2G(t-\tau)\dot{\epsilon}'_{ij}(\tau)d\tau \tag{5.27}$$

$$\frac{1}{3}\sigma'_{ii} = K(t)\epsilon'_{kk}(0) + \int_0^t K(t-\tau)\dot{\epsilon}'_{kk}(\tau)d\tau \tag{5.28}$$

Generalized Maxwell model and Prony series

The standard linear solid model can be extended to include several Maxwell elements assembled in parallel, to become a generalized Maxwell model. It is the most general form of the linear viscoelastic model, which takes into account that the relaxation occurs at a distribution of times.

Figure 5-9 shows the generalized Maxwell model. It's necessary to have many spring–dashpot Maxwell elements to accurately represent the distribution of relaxation times.

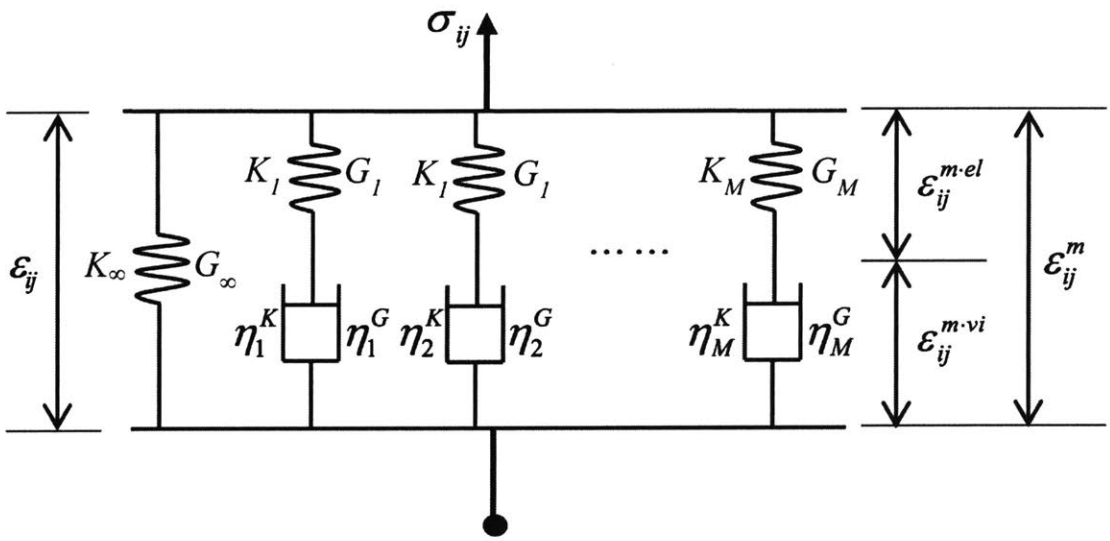

Figure 5-9: Generalized Maxwell model with several parallel Maxwell elements. [33]

The resulting stress vs. time could be modeled as Prony series:

$$G(t) = G_\infty + \sum_{i=1}^{N} G_i e^{-\frac{t}{\tau_i^G}}, \tag{5.29}$$

$$K(t) = K_\infty + \sum_{i=1}^{N} K_i e^{-\frac{t}{\tau_i^K}}, \tag{5.30}$$

where there are N elements with moduli E_i, viscosity η_i^G, η_i^K, and relaxation times $\tau_i^G = \frac{\eta_i^G}{E_i}$, $\tau_i^K = \frac{\eta_i^K}{E_i}$.

Prony series are adapted in many finite element analysis software, where users decide what parameters to input to the system.

5.4.2 Viscoelastic glass model

With the discussion about viscoelasticity in Section 5.4.1, I could now implement a viscoelastic glass model during the FSI. As we've discussed in Chapter 3 and seen in equation 3.1, the viscosity is closely related to temperature, so we could calculate the glass viscosity at the dwelling temperature.

To start with, I only include one term in Equation 5.29. Since the dwelling

temperature is $550°C$ in our experiments, very close to the annealing point of $557°C$ for Schott D263 glass, so I used the value of $\eta = 10^{12}\, Pa \cdot s$ for its viscosity. We also have the value of glass elasticity at room temperature $E = 72.9\, GPa$, I chose $E_1 = 0,\ E_2 = E$. The argument is that the long-term elasticity should be zero such that the internal stress of the glass could fully relieved; while the instant response should be the same as the pure elastic material. Though it's questionable whether I should use the value for E at room temperature, because the elastic moduli of glass at higher temperature tends be smaller. Later in my simulations, I did try slightly smaller E, but for now I'll show results from this set-up.

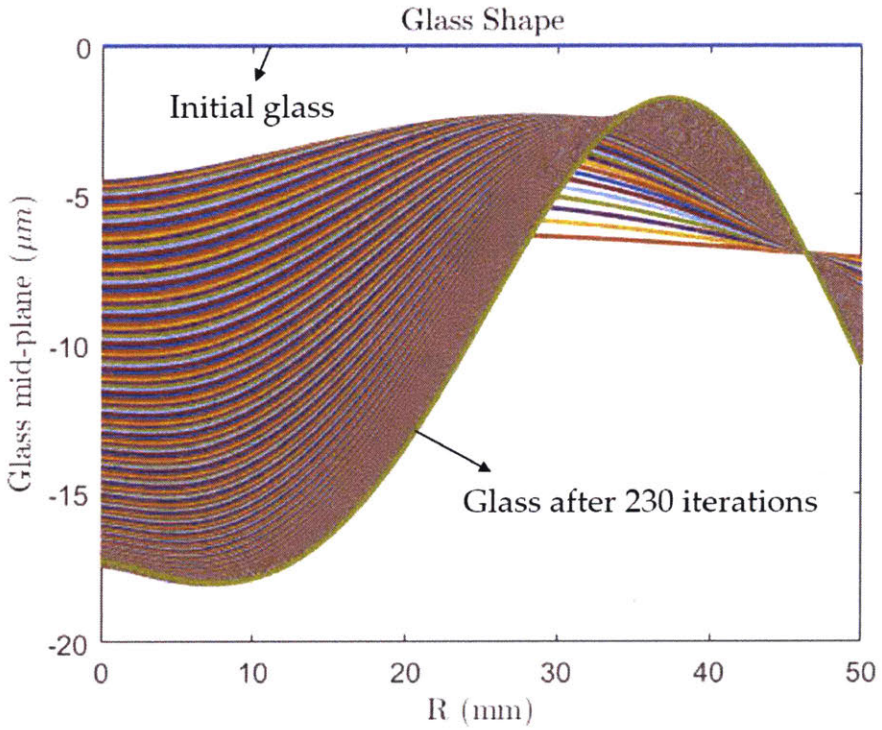

Figure 5-10: Iterative scheme updates the shape and position of the viscoelastic glass through iterations. Blue line shows the initial input glass. Green line shows the output glass after 230 iterations.

Figure 5-10 shows how the shape and position of the viscoelastic glass is updated in each iteration. In total 230 iterations were performed and the glass after each iteration was plotted on the same figure shown here.

Comparing this to the glass using an elastic model in Figure 5-5, we could reach a

comparable shape with far fewer steps. This is because relaxation times are introduced into the viscoelastic model, so the stress relief mechanism could be more effectively simulated. As said before, each iteration in the scheme 5.2.2 corresponds to a certain physical time, in the viscoelastic model I set the simulation time to be slightly greater than the relaxation time.

5.4.3 Influence of simulation time

I also studied the influence of simulation time for the viscoelastic model.

Figure 5-11 shows the same simulation of Figure 5-10 extended to 980 iterations. (a) With 700 more iterations, the glass deformed even further than Figure 5-10, and faster than Figure 5-6. (b) shows RMS von Mises stress of the glass between successive iterations, which also reduces dramatically with the increasing of iterations. Though the von Mises stress is not zero, it does show a slight tendency of keep decreasing with even more iterations, which has not been seen in elastic models, as compared to Figure 5-6 (c).

Both figures help to reinforce our conclusion that the stress relief mechanism is only captured by viscoelastic model, and not elastic model.

5.4.4 Influence of varying bearing permeability

In reality, the bearing permeability was not entirely the same across the whole bearing. So I was interested in how much the pressure distribution would change with different permeability along the radial direction in our model.

Effects to the air film pressure distribution

Figure 5-12 was built on top of the model in Figure 5-3 and divided the bearing into two parts. Region 1 is a circular area with radius less than r_1 and it has permeability κ_1; region 2 is a ring area with radius between r_1 and R.

Figure 5-13 show the pressure distribution in this two-permeability model. Both figures show that the larger the permeability, the higher the pressure in the air films.

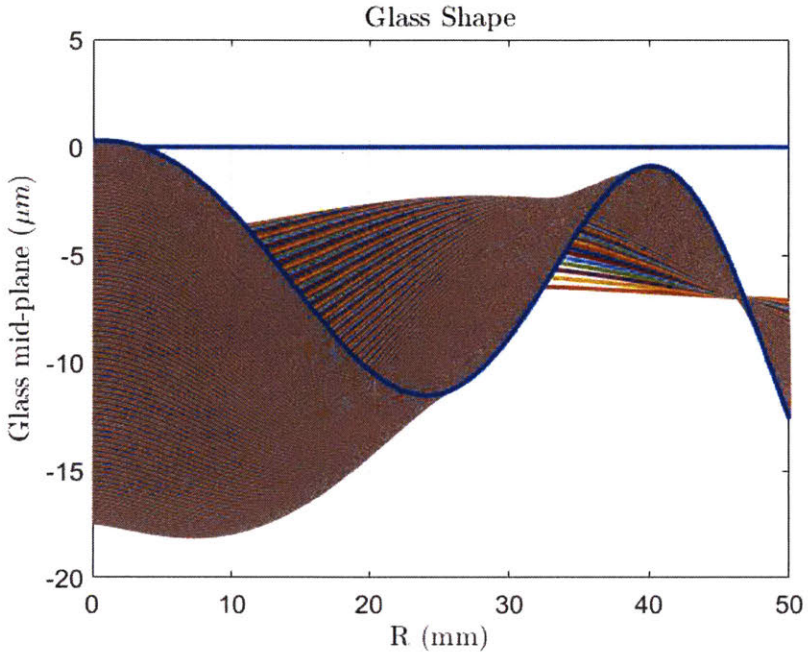

(a) Evolution of the glass through 980 iterations.

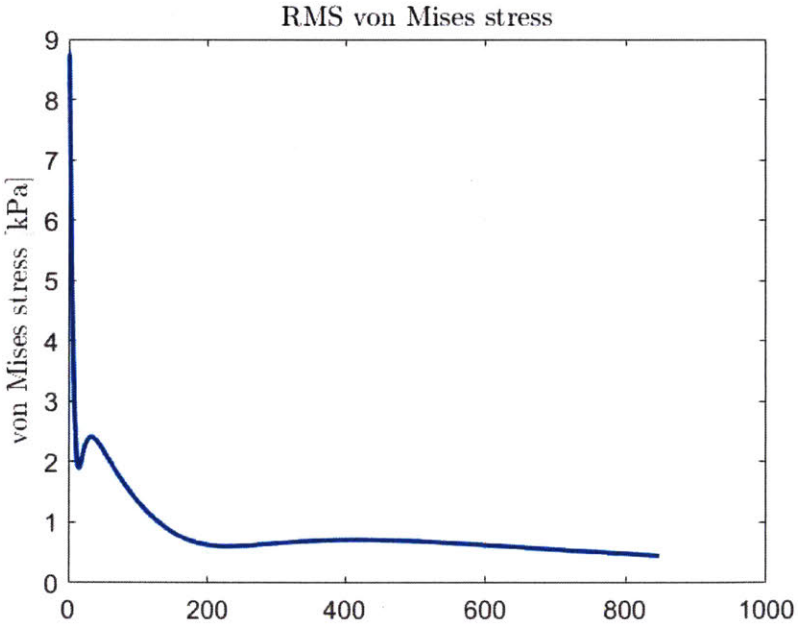

(b) RMS von Mises stress inside the glass between successive iteration.

Figure 5-11: Iterative scheme updates the shape and position of the viscoelastic glass through iterations. Blue line shows the initial input glass. Green line shows the output glass after 980 iterations.

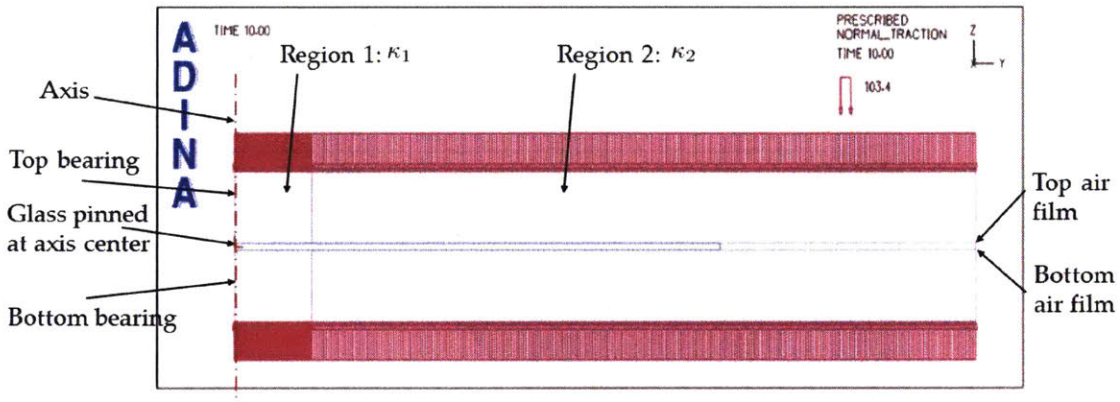

Figure 5-12: 2D axisymmetric model with two different bearing permeability along radial direction.

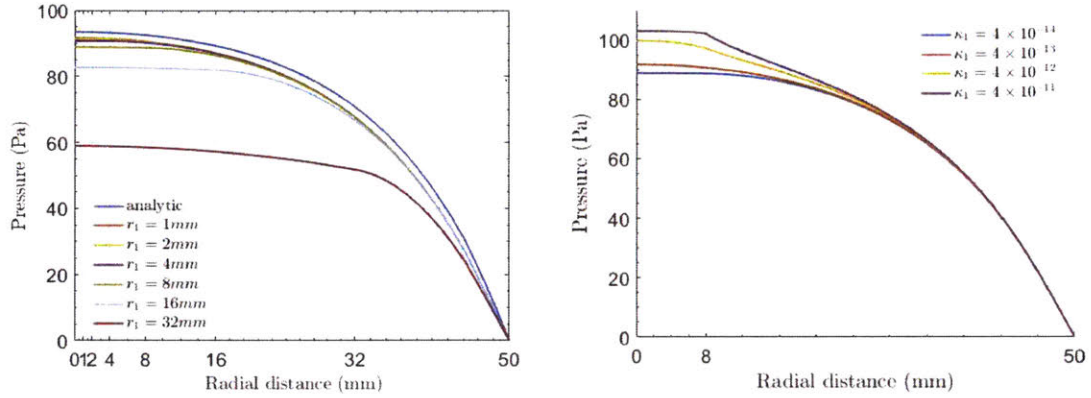

(a) Varying the size r_1 with same permeability $\kappa_1 = 4 \times 10^{-14} m^2$.

(b) Varying permeability in region 1 κ_1 with same $r_1 = 8\,mm$.

Figure 5-13: Pressure distribution in the two-permeability model. In both figures, region 2 has same permeability $\kappa_2 = 4 \times 10^{-13} m^2$.

Effects to the glass deformation

I introduced more non-uniformity of bearing permeability to study the effects they have to the deformation of the glass. To only see the effects from varying permeability, I ignored the gravity force applied to the glass.

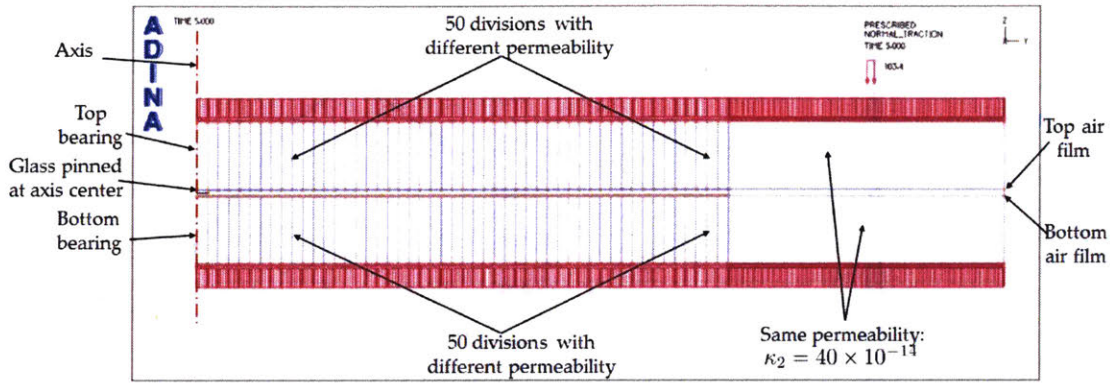

Figure 5-14: Introduce non-uniformity of bearing permeability.

In Figure 5-14 I divided both top and bottom bearings within the radius of the glass into 50 regions with variable permeability along radial direction.

A lot of different input bearing permeability profiles were tested and the shape of the glass after the same number of steps were recorded. Figure 5-15 presents a model with the same permeability everywhere else, except a singular point only in one of the 100 cells. Each row shows one case with a singularity in top bearing at different locations. The left column shows the profile of input bearing permeability, while the right column shows the surface profile of the output glass.

In all three cases, the magnitudes of the singular point are the same (25% higher than other values), and the output P-V in glass are also very comparable, around $0.11\,\mu m$. The peak in the output glass shape remains at approximately the same place of the input singular point, but the bandwidth of the "delta" shape in the input has been expanded significantly. This suggests that air-bearing slumping should be able to smooth out initial singularities in the system.

Then I performed another test with normal distributed bearing permeability in all 100 cells and ran the same simulation. Then I took the Fourier transformation of both the input bearing permeability profile and the output glass surface profile, and calculated the transfer function from permeability non-uniformity to glass deformation.

The results are shown in Figure 5-16. (a) The total variation of the bearing

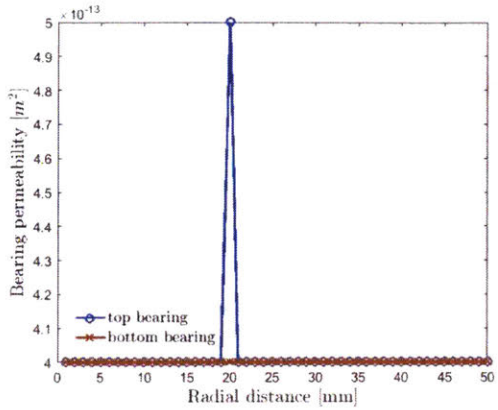

(a) Input singularity at 20 mm.

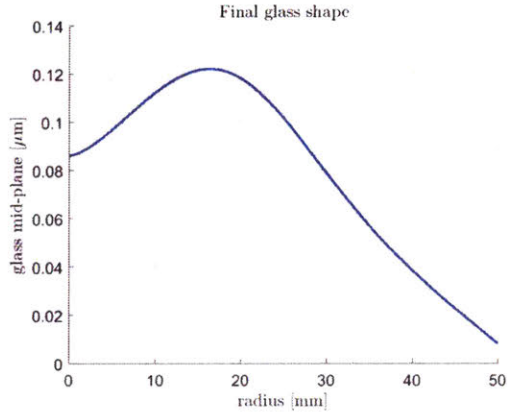

(b) Output glass shape with singularity at 20 mm.

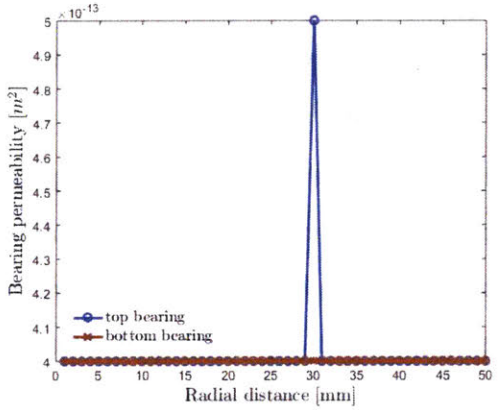

(c) Input singularity at 30 mm.

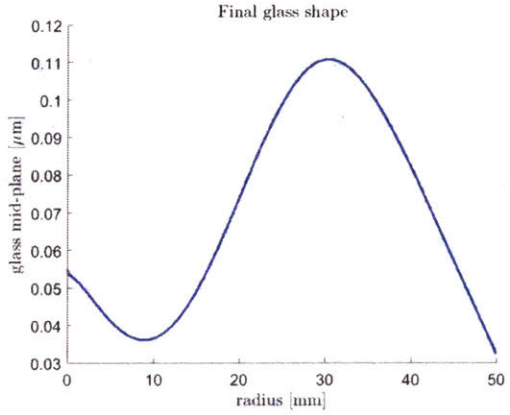

(d) Output glass shape with singularity at 30 mm.

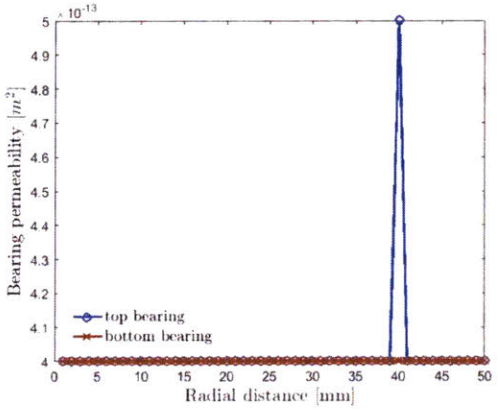

(e) Input singularity at 40 mm.

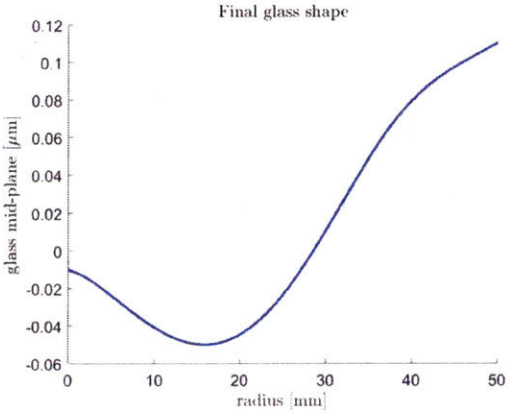

(f) Output glass shape with singularity at 40 mm.

Figure 5-15: Results of added singularity in input bearing permeability with same magnitude at three different locations. Input on the left, output on the right.

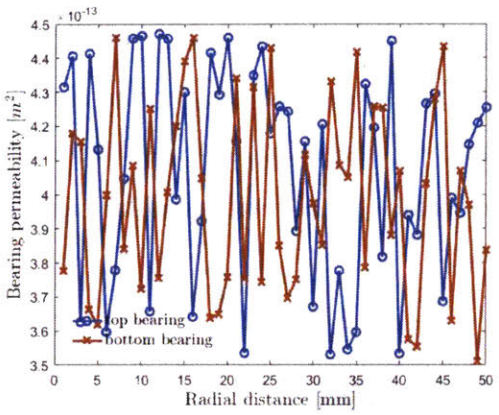

(a) Input non-uniform bearing permeability with normal distribution.

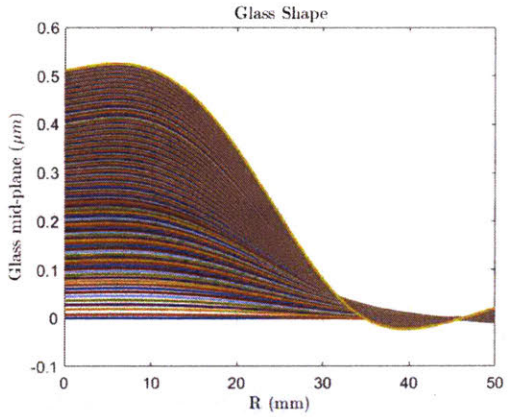

(b) Output glass deformation after 200 iterations.

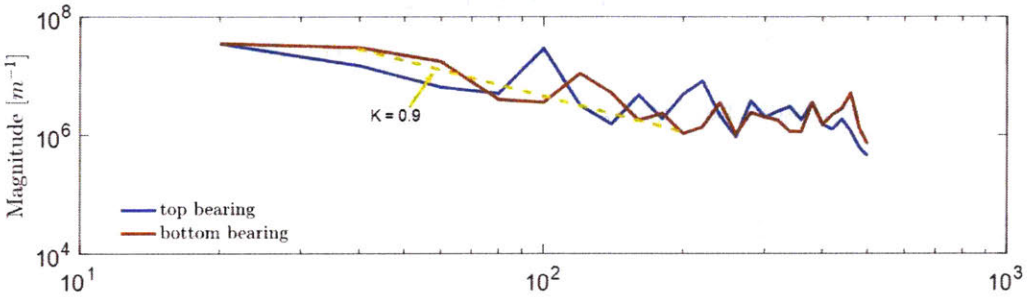

(c) Transfer function from permeability non-uniformity to glass deformation.

Figure 5-16: Normal distributed input bearing permeability.

permeability difference is also 25%. (b) The output is a smooth curve with P-V around $0.5\,\mu m$. (c) The transfer function from the bearing permeability non-uniformity to glass deformation shows that the air-bearing system acts like a low-pass filter, and the fitted line has a slope equal to -0.9, very close to -1 for a standard low-pass filter.

High frequency terms ($> 100\,Hz$ or $< 10\,mm$) are smoothed out, while lower frequency terms ($\leq 100\,Hz$ or $\geq 10\,mm$) have the largest components. This also proves that air-bearing slumping is capable of removing non-uniformity on the order of millimeters, thus greatly eliminating mid-range spatial frequency errors in the slumped glass.

Another important message I learned from these tests is that gravity did play a

huge role in deforming the glass. After I eliminated the gravity force in the above two examples, the P-V of the simulated glass shape was brought down from $15\,\mu m$ with gravity to $\sim 1\,\mu m$ without gravity. This suggests we could use vertical slumping design instead of the original horizontal slumping design in our experiments, to eliminate gravity influence and generate better surface profile with smaller surface variations.

5.5 3D cylindrical viscoelastic model

After the 2D axisymmetric modeling, I carried out simulations for a 3D model with cylindrical bearing. Now the flow and structure are both 3D, the number of elements and nodes have increased exponentially, as well as the computation time for the simulation. The results here are only preliminary.

5.5.1 Model set-up

The simulation assumptions are:

- The model for both bearings are cylindrical with the same curvature, the top one convex and bottom one concave;
- The bearings and the glass are all centered at the origin of the Cartesian coordinate system, and they are all symmetric in four quadrants, so only one quadrant need to be modeled with the other three being symmetric;
- The center of the glass is pinned at the origin, such that the horizontal position of the glass is fixed while only vertical motion and deformation are allowed;
- The boundary conditions along the two symmetric planes in one quadrant are slipping-wall with no penetration through the wall;
- No thermal process or temperature change is considered, which means we are only modeling the dwelling stage at constant temperature $500°C$.

The model is shown in Figure 5-17.

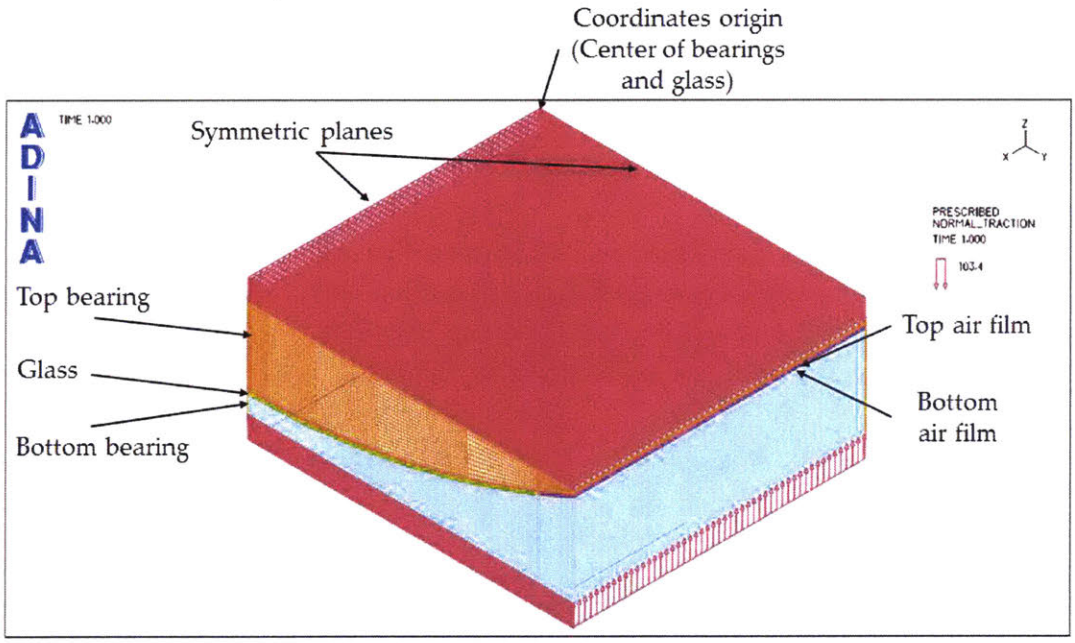

Figure 5-17: 3D cylindrical model setup in ADINA. Only one quadrant of the slumping system is modeled. The boundary conditions imposes symmetric flow through the two symmetric planes. The motion and deformation of the glass are all in vertical directions.

5.5.2 Preliminary simulation results

Using the above set-up with the same viscoelastic glass model, I performed the one iteration according to the 5.2.2.

Glass shape after one iteration is shown in Figure 5-18. The largest deformation is only $0.4\mu m$.

To better understand how the glass would deform, more iterations need to be included in the simulation, and the influences of some key parameters need to be studied.

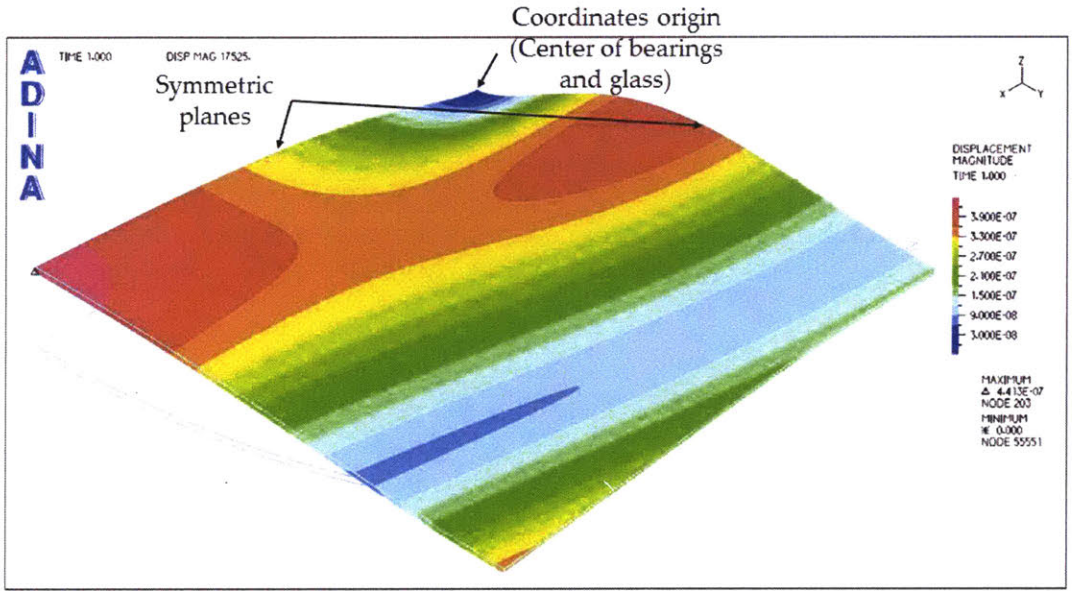

Figure 5-18: 3D Model setup

Chapter 6

Establishing credibility of the results

Now that I've results from both experiments and simulations, it's important to make connections between both approaches, and build credibility of our tools.

6.1 Comparison between experiments and numerical simulations

Figure 6-1 compares the 2D axisymmetric simulation results with one of the slumped glass G20160603. The original reconstructed surface profile of this sample is shown in Chapter 4 Figure 4-15. The circles are scattered surface wavefront data at every grid points on the slumped glass. These circles do not make a single curve because the surface profile of the glass is not fully axisymmetric and has strong astigmatism. Each line in this figure represent one simulation with a different bearing permeability, ranging from $12 \times 10^{-14} \sim 50 \times 10^{-14}\, m^2$. The pressure input for the simulation is $0.025\, psi$ as used by the experiment, and the numerical time also corresponds to the $16\, h$ dwelling time.

Despite the difference in curved simulated results with different bearing permeability, we could still see that the simulation results are quite comparable to the experiments.

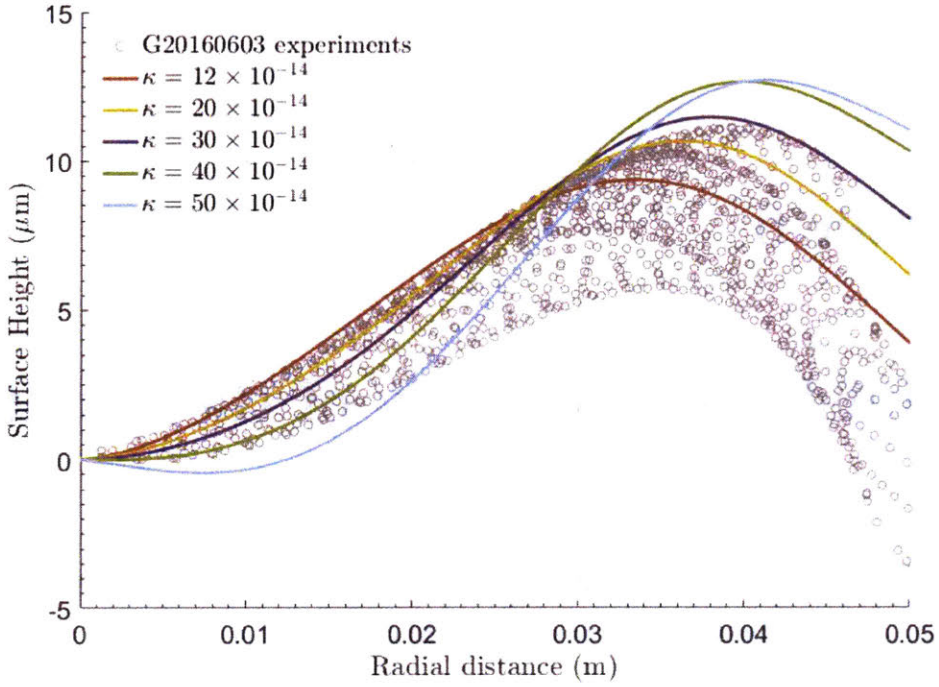

Figure 6-1: Compare 2D axisymmetric simulation results with different bearing permeability to one of the slumped glass G20160603. The dots are scattered surface wavefront data at every grid points on the slumped glass

6.2 Error analysis

Though we've shown that the simulations are in general pretty comparable to the experiments, there are still some gaps between these two approaches. In this chapter, I'll do some error analysis to have an idea of how much improvement we could get through air-bearing slumping.

Both bearing surface flatness and uniformity of bearing permeability are crucial to the production of high quality mirrors, so I spent some efforts inspecting them.

6.2.1 Bearing flatness measurement

First, there are some problems with the silicon carbide (SiC) mandrels that we use for our slumping experiments. We have always suspected that the surface of these bearings are not flat and round enough, which might cause some systematic errors in

the slumped glass samples.

To have a sense of whether this is true, I measured the surface waviness of the central square region of both bearings with coordinate-measuring machine (CMM)[1]. The machine I used at the MIT Department of Mechanical Engineering machines shop has mechanical probe and the precision is only $0.5\,\mu m$, so the measurement results are only resolved up to $0.5\,\mu m$.

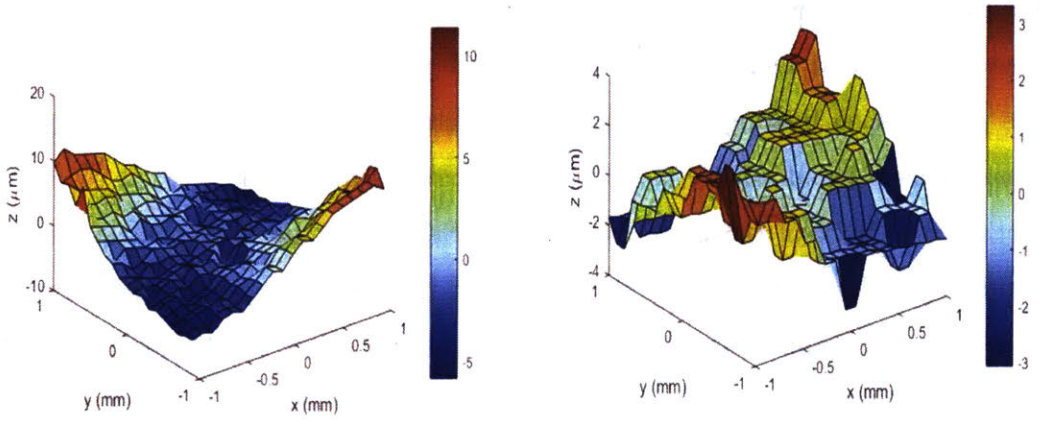

(a) Top bearing has strong astigmatism, variation of the surface height is about $15\,\mu m$.

(b) Bottom bearing has light astigmatism, variation of the surface height is about $5\,\mu m$.

Figure 6-2: SiC bearing surface profiles measured with the coordinate-measuring machine.

Figure 6-2 shows the CMM measured top and bottom SiC bearing surface profiles. From these plots, we did find quite some astigmatism on both bearing surfaces, but the magnitudes were quite different between the two. The top bearing showed stronger astigmatism with a much larger surface waviness of $15\,\mu m$ (Figure 6-2 (a)), while the bottom bearing showed slightly milder surface waviness of less than $5\,\mu m$ (Figure 6-2 (b)). The mosaic pattern in the bottom bearing is essentially because the surface roughness is touching the resolution of the machine.

[1]A coordinate-measuring machine is a device for measuring the physical geometrical characteristics of an object. Measurements are taken by a probe (mechanical, optical, or laser) attached to the moving axis of this machine.

Though the measurement is somewhat rough, it's still quite informative. These bearing unflatness definitely brought about some surface errors to the slumped glass, but it's hard to quantify this in the actual experiments. However, this could be simulated with the finite element model I built, which is one possible way to further my numerical analysis.

The reasoning behind these unevenness and unflatness in bearings are the introduction of some additional stresses during the bonding of the porous air bearing face to the nonporous housing. In order to create a plenum of SiC, we need to manufacture the well polished high flatness porous bearing face and the nonporous housing separately and then bound them together with special glues. However, the bonding may tort the pre-polished bearing face and create different curvatures in two orthogonal directions. This is one downside of using SiC as bearing materials.

Another drawback of the material choice of SiC is it's too hard to grind, thus very hard to get the conical shape[2] for the curved bearing. One possible solution to this issue is to use graphite as bearing material, because of the much greater ease of manufacturing. For testing purposes, we designed and ordered a pair of conical porous air bearings made of graphite. The concept design with these graphite bearings are shown in Figure. 6-3.

The blue trunks in the figure are housings made of aluminum, while the grey parts attaching to them are porous graphite. (a) As in flat circular bearing system, the pair of conical bearings also sit on top of a tip-tilt stage, controlled by tilt actuators. (b) Two bearing surfaces are separated by a Kovar shim with a thickness equal to the glass thickness plus the thickness of the two air films.

6.2.2 Bearing permeability measurement

The permeability of porous silicon is typically around $10^{-15}\,m^2$, while the permeability of carbon graphite varies. Some report measuring a permeability for porous carbon graphite around $0.07\text{–}10\times10^{-15}\,m^2$[15]. Since bearing permeability directly affects the

[2]Conical shape is an approximation of the actual shape of the X-ray telescope optics, where the generatrix is not a traight line but rather a parabolic line or hyperbolic line.

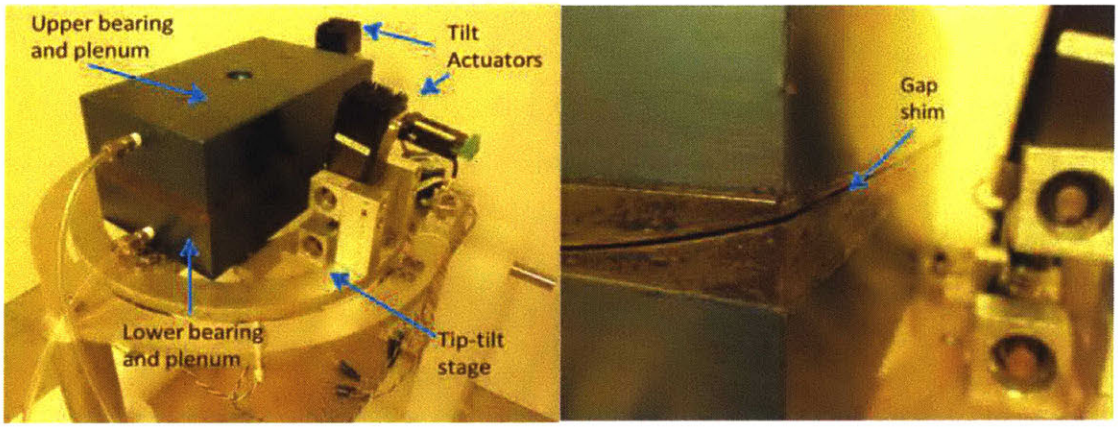

(a) The bearing system sitting on top of a tip-tilt stage controlled by tilt actuators.

(b) Two bearing surfaces are separated by a Kovar shim.

Figure 6-3: Slumping system concept with graphite bearings.

pressure distribution in the gap and controls the final slumping result, the accurate value and uniformity of the actual bearings are of crucial importance.

I've examined the bearing permeability of both SiC bearings and graphite bearings used in our experiments by measuring the local flow rate from the bearing surface. The experiment set-up are shown in both Figure 6-4 (b) and Figure 6-5 (b). Continuous air flow with constant pressure is fed into the bearing plenum through the inlet on the backside, and a plastic tube is applied on the bearing side, with an inner diameter of $0.1\,in$ connecting to the flowmeter. Then the air flow would push the float inside the flowmeter to a certain height, and the reading from the scale indicate the total flow rate inside the tube.

The bearing surface is meshed into many small squares of size $0.1\,in \times 0.1\,in$ to match the diameter of the tube, so each time only the flow coming from one element will be measured. We repeated the measurement for all elements on the surface and calculate the bearing permeability for each of them through the following formula:

$$\kappa = \frac{4\dot{V}\nu}{\pi d^2 P} \tag{6.1}$$

where $\dot{V}$ is the measured flow rate in volume per unit time, $\frac{\pi d^2}{4}$ is the surface area

inside the tube, ν and P are the viscosity and pressure of the air supply. The results are shown below.

Figure 6-4 shows the measurement results for SiC bearings. The thickness of the porous material is the same over the whole surface, but the outer rim region has been coated with a layer of seal, resulting in a permeability loss of about 50%. In the central regions without the seal, the permeability is about $4 \times 10^{-15}\, m^2$.

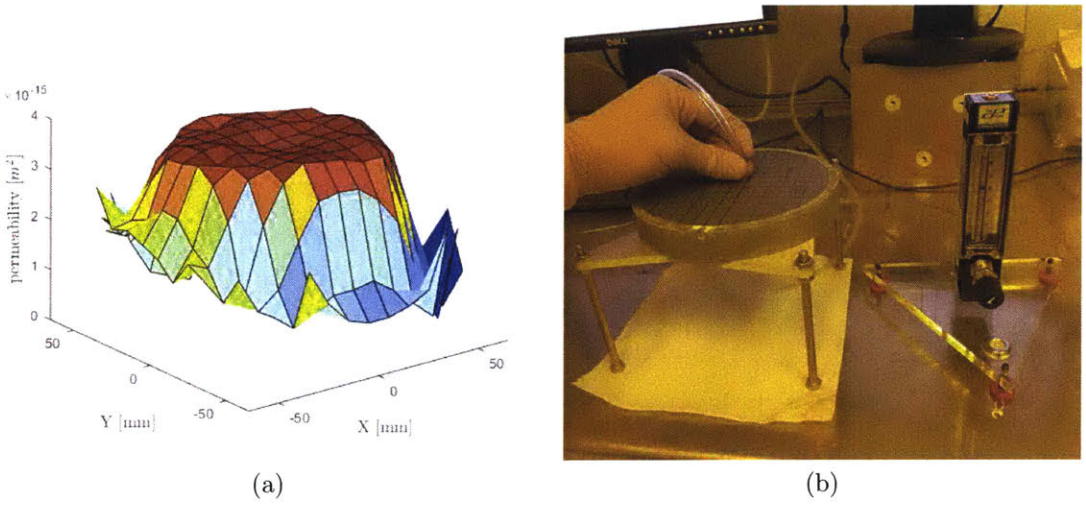

(a) (b)

Figure 6-4: Measured bearing permeability of SiC.

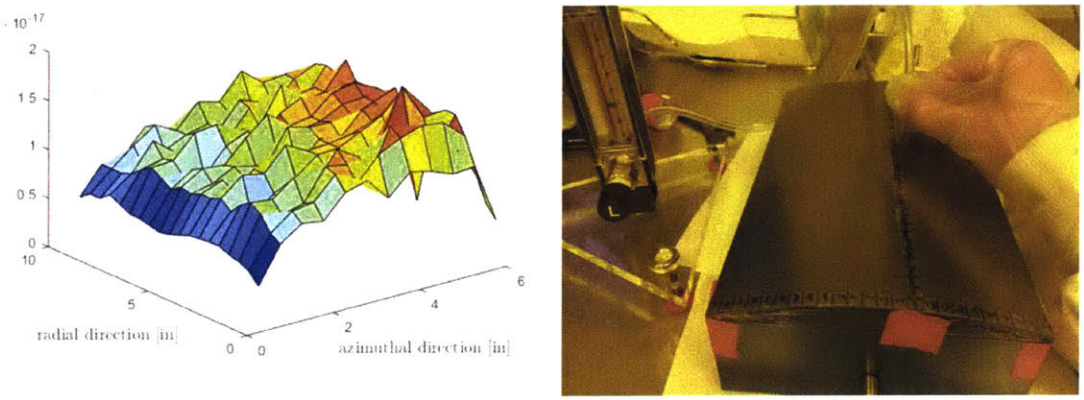

(a) (b)

Figure 6-5: Measured bearing permeability of graphite.

Figure 6-5 shows the measurement results for graphite bearings. The thickness

of the porous material is the same along the radial direction, but along the azimuth direction it is distributed according to a circular function. Having the thickness variation considered, we get the permeability distribution as shown in (a). The average permeability is about $1.1 \times 10^{-17}\, m^2$, which is much lower than the literature and our belief.

Not just the graphite bearings, in fact, the permeability measured for both bearings are below our expectations. It's very implausible that our measurements are correct. There are a lot of uncertain factors that haven't been assessed before the measurement, for instance, the calibration of the flowmeter, the true number of the air pressure. These factors all affect the absolute numeric figures of the measurement results, but the relative magnitude between different part of the same bearing are not much disturbed. Thus, despite the measurements themselves have some issues in the utter correctness, they still provide imperative knowledge about how much bearing permeability fluctuations we need to deal with, a crucial step towards obtaining positive experiment outcomes and validating simulation results.

6.2.3 Influence of gravity

After a detailed examination of the simulated results with and without gravity force while keeping all other parameters identical, a difference of not less than $15\,\mu m$ occurs in the surface P-V. The simulations show that having the gravity considered, the typical glass surface P-V is about $16\,mum$, as seen in Figure 5-10. However, by excluding the gravitational force, we would be able to get the surface P-V down to $0.5\,\mu m$, as shown by Figure 5-16 (b).

These results indicate that the highly curved central lob of the glass we noticed from all experiments might be caused by gravity (see comparison Figure 6-1). The analysis also brings up another feasible future path of using vertical slumping arrangements and aligning the gravity force with the tangential surface of the glass. If the experiments could agree with the simulations, much higher quality mirrors could be produced.

6.3 Glass surface micro-roughness measurement

Though it has been asserted that slumping in general excels at correcting long spatial wavelength errors, and through our past studies we reported that air-bearing slumping has the capability of removing mid-range spatial frequency errors, we would like to look into the high-frequency short-wavelength components on the glass surface as well to make sure air-bearing slumping doesn't incur additional surface roughness.

Atomic-force microscopy (AFM) was used for this purpose. This kind of scanning probe microscopy has very high resolution on the order of nanometer, allowing me to have a closer inspection of the surface structure of the slumped glass.

With the AFM machine at MIT Center for Materials Science and Engineering (CMSE), two glass samples were examined as shown in Figure 6-6 and Figure 6-7.

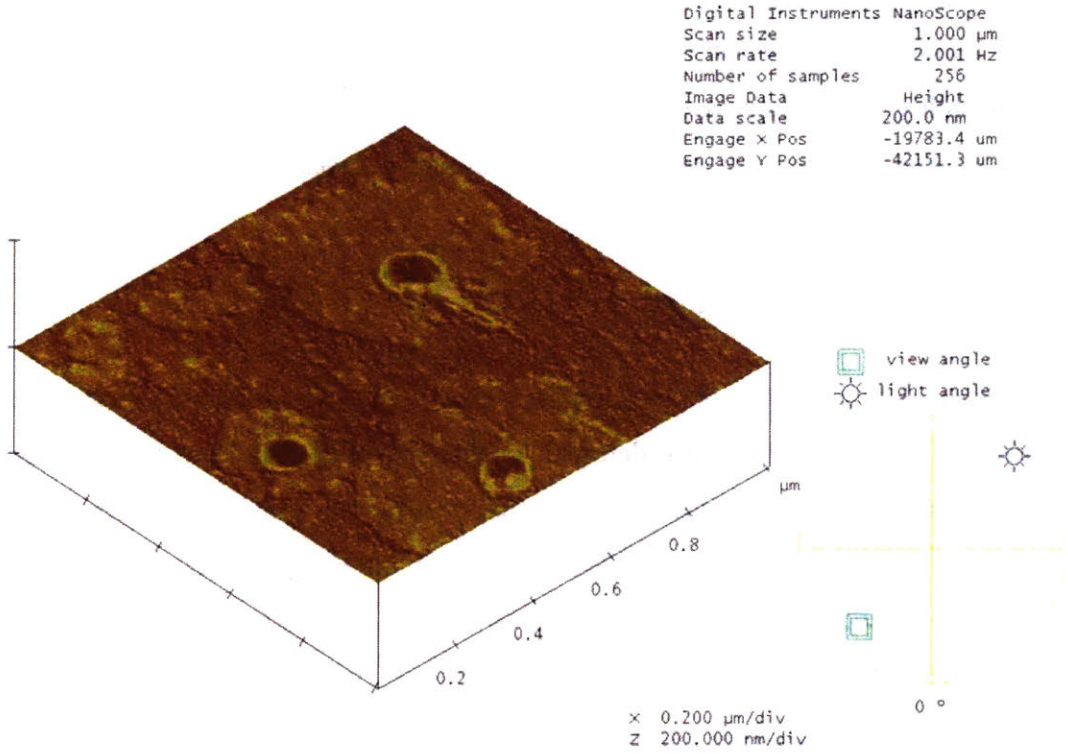

Figure 6-6: Sample G20160711 (not RCA cleaned) surface micro-roughness measured with AFM.

Both figures show a square region of size $1\,\mu m \times 1\,\mu m$ in the center of each glass.

The sample in Figure 6-6 comes directly after slumping, while the sample in Figure 6-7 has been RCA cleaned[3] before AFM measurement.

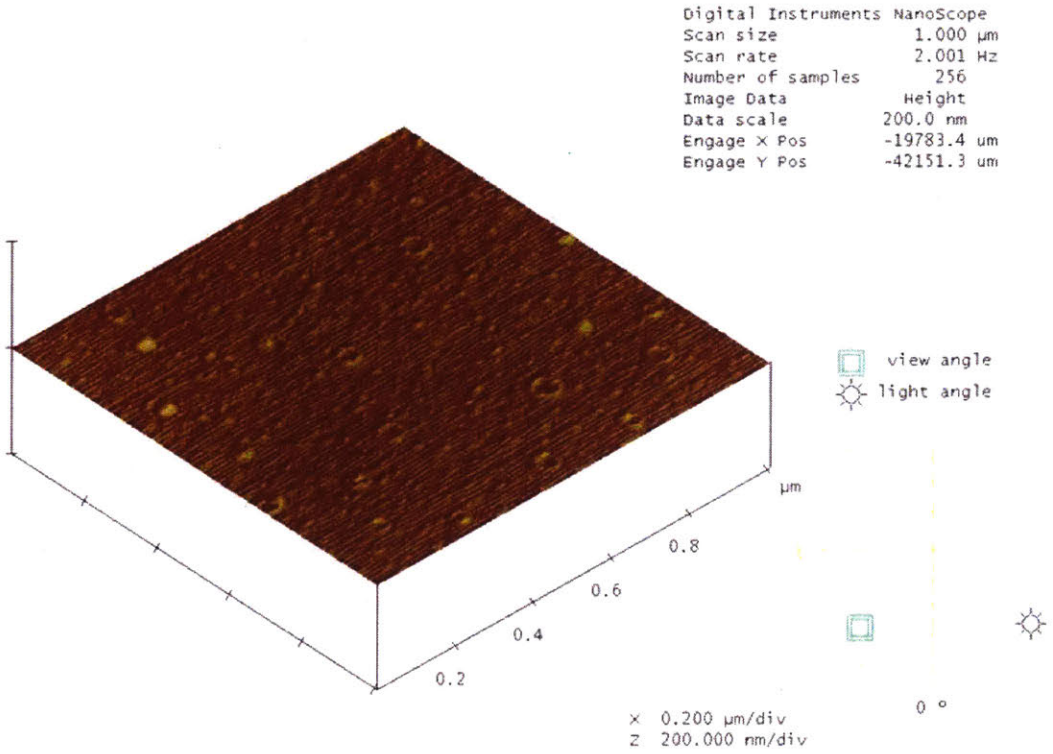

Figure 6-7: Sample G20160609 (RCA cleaned) surface micro-roughness measured with AFM.

There are some "island" regions in Figure 6-6 with size of half a micron, which are not present in Figure 6-7. So it's very likely these regions are organic contaminants which could be easily removed and not damaging the glass. Nevertheless, both figures show signs of small "well"s with size of less than $100\,nm$, and the "edge" of the "well" rises up of about $2\,nm$ in both cases. It appears like some materials may have been deposited on to the surface of the glass, though I haven't fully understood what they are.

[3]The RCA clean is a standard three-step wafer cleaning process used in semiconductor manufacturing. I only performed the first step — SC-1, for removing organic contaminants and particles.

Chapter 7

Conclusions

In the end, after completing a series of experiments and simulations, the paramount comparability of the two approaches have been established, and evidences of air-bearing slumping correcting mid-range spatial frequency errors have been identified. A deeper understanding of the mechanism behind the slumping practices have also been developed, building up more confidence towards our slumping system.

However, there is still quite a lot of room for improvement in surface quality within the realm of slumping, and we've identified a few of them. Some other methods for manufacturing and correcting X-ray telescope mirrors have also produced promising results recently, and we should keep an open mind about searching for other potential alternatives as well.

7.1 Achievements

My main achievements in air-bearing slumping could be summarized into the following 4 aspects:

1. A more reliable and faster controller has been developed for the slumping tools, allowing for rapid and precise experiments.
2. A finite element model based on fluid-structure interaction with viscoelastic glass model has been proposed, which generates comparable results with the

experiments.

3. A more comprehensive understanding of the slumping mechanism has been promoted, and the previous belief of the existence of an "equilibrium" glass shape has been falsified. Thus given the viscoelasticity in glass, it's pivotal to control the slumping time.

4. A grounded assertion has been affirmed that air-bearing slumping has the competence of smoothing out system non-uniformity on the order of millimeters, thus eliminating mid-range spatial frequency errors in the glass.

7.2 Suggestions for future work

For our work on air-bearing slumping, first, more 3D simulations and experiments on cylindrical slumping need to be done. In Chapter 5, I only showed one step of simulation with fluid-structure interaction. To get a simulated result indicative of the physical experiences, more iterations need to be finished. And as in the 2D axisymmetric model, the influences of key parameters should also be studied.

Since simulations have suggested that vertical slumping to cancel the gravity influence, we have designed a vertical slumping tool for the flat SiC bearings, shown in Figure 7-1 (a). The bearings are now coordinated in a vertical fashion, through the compression force via three springs that sustain high temperature. The bearings are still separated by Kovar shims, and the glass hangs down from a beam above the bearings with tungsten wires. According to this design, I machined the supporting trusses in stainless steel with abrasive waterjet machine and assembled them shown in Figure 7-1 (b).

One final thing that's essential to the broader picture is that the actual improvement of angular resolution from our slumped mirrors need to be calculated.

Apart from our work in slumping, I also believe that more mirror fabrication methods need to be developed, especially under the urgent context of the Lynx mission.

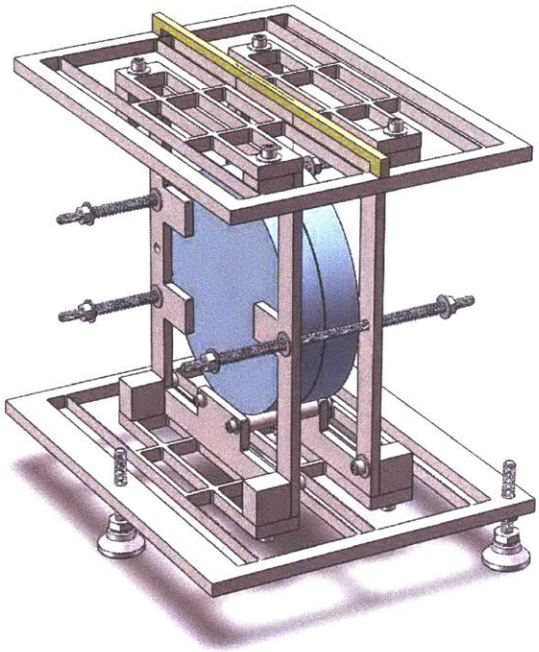

(a) SolidWorks design.

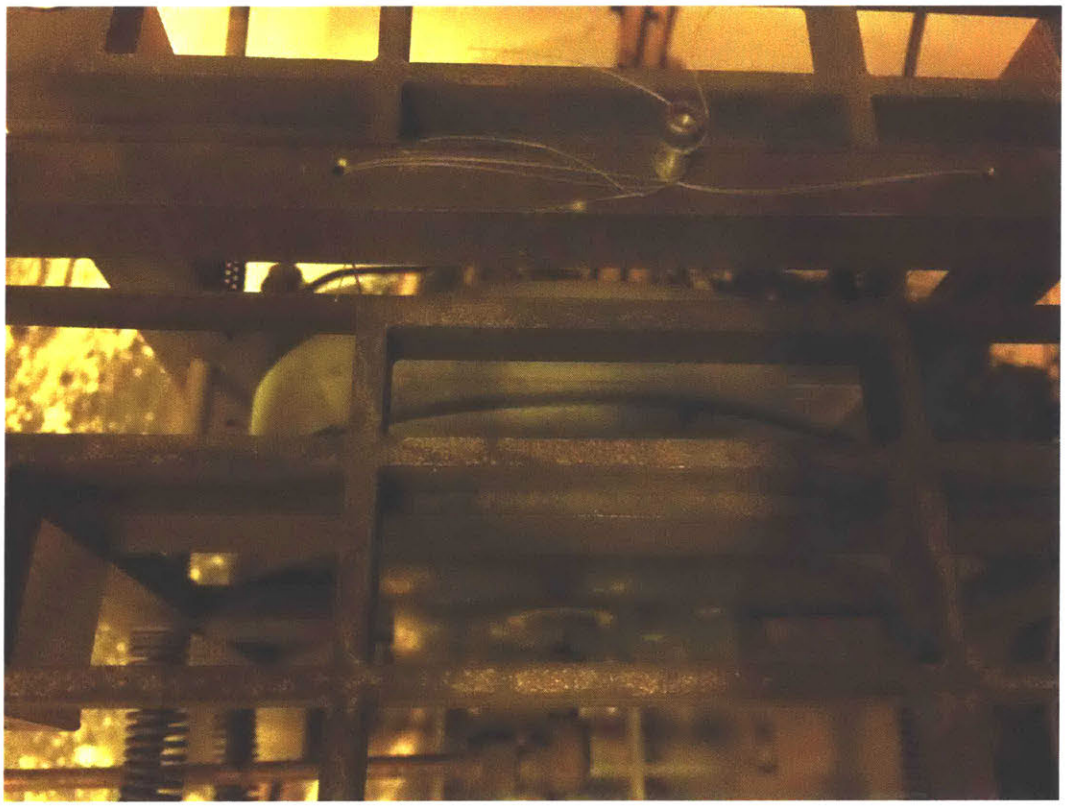

(b) Tool set-up.

Figure 7-1: Vertical slumping tool.

Bibliography

[1] Mireille Akilian. *Methods of improving the surface flatness of thin glass sheets and silicon wafers.* PhD thesis, Massachusetts Institute of Technology, 2008.

[2] Abdul Mohsen Zuheir Al Husseini. *Design and modeling of a third generation slumping tool for X-ray telescope mirrors.* PhD thesis, Massachusetts Institute of Technology, 2011.

[3] NRC Astronomy. New worlds, new horizons in astronomy and astrophysics, 2010.

[4] William D Callister and David G Rethwisch. *Fundamentals of materials science and engineering: an integrated approach.* John Wiley & Sons, 2012.

[5] Chi Ming Hubert Chen. *Development of hard X-ray imaging detectors for the High Energy Focusing Telescope.* PhD thesis, California Institute of Technology, 2008.

[6] Maximilien J Collon, Marcelo Ackermann, Ramses Günther, Abdelhakim Chatbi, Giuseppe Vacanti, Mark Vervest, Alex Yanson, Marco W Beijersbergen, Marcos Bavdaz, Eric Wille, et al. Making the athena optics using silicon pore optics. In *SPIE Astronomical Telescopes+ Instrumentation*, pages 91442G–91442G. International Society for Optics and Photonics, 2014.

[7] David Madrid Costa and Teresa Ferrer-Blasco. Adaptive optics, wavefront aberrations and visual simulation. 2010.

[8] European Southern Observatory. Atmospheric opacity graph, 2010.

[9] Craig R Forest, Claude R Canizares, Daniel R Neal, Michael McGuirk, and Mark L Schattenburg. Metrology of thin transparent optics using shack-hartmann wavefront sensing. *Optical engineering*, 43(3):742–753, 2004.

[10] Jessica A Gaskin, Martin C Weisskopf, Alexey Vikhlinin, Harvey D Tananbaum, Simon R Bandler, Marshall W Bautz, David N Burrows, Abraham D Falcone, Fiona A Harrison, Ralf K Heilmann, et al. The x-ray surveyor mission: a concept study. In *SPIE Optical Engineering+ Applications*, pages 96010J–96010J. International Society for Optics and Photonics, 2015.

[11] R Giacconi, WP Reidy, T Zehnpfennig, JC Lindsay, and WS Muney. Solar x-ray image obtained using grazing-incidence optics. *The Astrophysical Journal*, 142:1274–1278, 1965.

[12] Präzisions Glas & Optik GmbH. D263 t thin glass specifications.

[13] Fiona A Harrison, William W Craig, Finn E Christensen, Charles J Hailey, William W Zhang, Steven E Boggs, Daniel Stern, W Rick Cook, Karl Forster, Paolo Giommi, et al. The nuclear spectroscopic telescope array (nustar) high-energy x-ray mission. *The Astrophysical Journal*, 770(2):103, 2013.

[14] Centrella Kouveliotou, E Agol, N Batalha, J Bean, M Bentz, N Cornish, A Dressler, E Figueroa-Feliciano, S Gaudi, O Guyon, et al. Enduring quests-daring visions (nasa astrophysics in the next three decades). *arXiv preprint arXiv:1401.3741*, 2014.

[15] Qi Liu. Study on variable permeability of porous carbon graphite. In *Applied Mechanics and Materials*, volume 178, pages 441–445. Trans Tech Publ, 2012.

[16] PRK Murti. Analysis of externally pressurized gas porous bearings. *(American Society of Mechanical Engineers, 1974.) ASME, Transactions, Series F- Journal of Lubrication Technology,*, 96:354–360, 1974.

[17] NASA NASA. Strategic plan, 2014. *National Aeronautics and Space Administration, Website*, 2014.

[18] Stephen L O'Dell, Thomas L Aldcroft, Ryan Allured, Carolyn Atkins, David N Burrows, Jian Cao, Brandon D Chalifoux, Kai-Wing Chan, Vincenzo Cotroneo, Ronald F Elsner, et al. Toward large-area sub-arcsecond x-ray telescopes. In *SPIE Optical Engineering+ Applications*, pages 920805–920805. International Society for Optics and Photonics, 2014.

[19] Stephen L O'Dell, Roger J Brissenden, William N Davis, Ronald F Elsner, Martin S Elvis, Mark D Freeman, Terrance Gaetz, Paul Gorenstein, Mikhail V Gubarev, Diab Jerius, et al. High-resolution x-ray telescopes. In *SPIE Optical Engineering+ Applications*, pages 78030H–78030H. International Society for Optics and Photonics, 2010.

[20] Ben C Platt and Roland Shack. History and principles of shack-hartmann wavefront sensing. *Journal of Refractive Surgery*, 17(5):S573–S577, 2001.

[21] Paul B Reid, Thomas L Aldcroft, Ryan Allured, Vincenzo Cotroneo, Raegan L Johnson-Wilke, Vanessa Marquez, Stuart McMuldroch, Stephen L O'Dell, Brian D Ramsey, Daniel A Schwartz, et al. Development status of adjustable grazing incidence optics for 0.5 arcsecond x-ray imaging. In *SPIE Optical Engineering+ Applications*, pages 920807–920807. International Society for Optics and Photonics, 2014.

[22] S Romaine, S Basso, RJ Bruni, W Burkert, O Citterio, G Conti, D Engelhaupt, MJ Freyberg, M Ghigo, P Gorenstein, et al. Development of a prototype nickel optic for the constellation-x hard x-ray telescope: Iii. In *Optics & Photonics 2005*, pages 59000S–59000S. International Society for Optics and Photonics, 2005.

[23] B Salmaso, S Basso, C Brizzolari, M Civitani, M Ghigo, G Pareschi, D Spiga, G Tagliaferri, and G Vecchi. Production of thin glass mirrors by hot slumping for x-ray telescopes: present process and ongoing development. In *SPIE Astronomical Telescopes+ Instrumentation*, pages 91512W–91512W. International Society for Optics and Photonics, 2014.

[24] Martin C Weisskopf, Jessica Gaskin, Harvey Tananbaum, and Alexey Vikhlinin. Beyond chandra: the x-ray surveyor. In *SPIE Optics+ Optoelectronics*, pages 951002–951002. International Society for Optics and Photonics, 2015.

[25] Martin C Weisskopf, Harvey D Tananbaum, Leon P Van Speybroeck, and Stephen L O'Dell. Chandra x-ray observatory (cxo): overview. In *Astronomical Telescopes and Instrumentation*, pages 2–16. International Society for Optics and Photonics, 2000.

[26] Malcolm L Williams, Robert F Landel, and John D Ferry. The temperature dependence of relaxation mechanisms in amorphous polymers and other glass-forming liquids. *Journal of the American Chemical society*, 77(14):3701–3707, 1955.

[27] Anita Winter, Elias Breunig, Peter Friedrich, Laura Proserpio, and Thorsten Döhring. Indirect glass slumping for future x-ray missions: overview, status and progress. In *SPIE Optical Engineering+ Applications*, pages 96030S–96030S. International Society for Optics and Photonics, 2015.

[28] Hans Wolter. Spiegelsysteme streifenden einfalls als abbildende optiken für röntgenstrahlen. *Annalen der Physik*, 445(1-2):94–114, 1952.

[29] William W Zhang. Manufacture of mirror glass substrates for the nustar mission. In *SPIE Optical Engineering+ Applications*, pages 74370N–74370N. International Society for Optics and Photonics, 2009.

[30] William W Zhang, MP Biskach, PN Blake, KW Chan, TC Evans, ML Hong, WD Jones, LD Kolos, JM Mazzarella, RS McClelland, et al. Lightweight and high angular resolution x-ray optics for astronomical missions. In *SPIE Optical Engineering+ Applications*, pages 81470K–81470K. International Society for Optics and Photonics, 2011.

[31] William W Zhang, Kai-Wing Chan, Raul E Riveros, and Timo T Saha. Toward diffraction-limited lightweight x-ray optics for astronomy. In *SPIE Optical Engineering+ Applications*, pages 96030Q–96030Q. International Society for Optics and Photonics, 2015.

[32] WW Zhang, MP Biskach, VT Bly, JM Carter, KW Chan, JA Gaskin, M Hong, BR Hohl, WD Jones, JJ Kolodziejczak, et al. Affordable and lightweight high-resolution x-ray optics for astronomical missions. In *SPIE Astronomical Telescopes+ Instrumentation*, pages 914415–914415. International Society for Optics and Photonics, 2014.

[33] Yuqing Zhang, Bjorn Birgisson, and Robert L Lytton. Weak form equation–based finite-element modeling of viscoelastic asphalt mixtures. *Journal of Materials in Civil Engineering*, 28(2):04015115, 2015.